TECHNICAL UNIVERSITY OF LIBEREC
Faculty of Mechatronics, Informatics and
Interdisciplinary Studies
Institute of Mechatronics and Computer Engineering

CONTROL OF STATIC AND DYNAMIC MECHANICAL RESPONSE OF PIEZOELECTRIC COMPOSITE SHELLS: APPLICATIONS TO ACOUSTICS AND ADAPTIVE OPTICS

by

KATEŘINA NOVÁKOVÁ

DISSERTATION THESIS

PhD programme: Science Engineering

Liberec 2013

Thesis Supervisor:
doc. Ing. Pavel Mokrý, Ph.D.
Institute of Mechatronics and Computer Engineering
Faculty of Mechatronics, Informatics and Interdisciplinary Studies
Technical University of Liberec
Studentská 1402/2
CZ46117 Liberec I
Czech Republic

Abstract

This dissertation thesis (Thesis) deals with the study of possibilities to actively control the static and dynamic mechanical response of planar structures by means of attached piezoelectric actuators. The considered planar structures have a form of flat or curved piezoelectric composite shells. It will be shown that such piezoelectric composite shells can provide efficient and rather simple mechatronic systems that can be profitably used in applications to acoustics and adaptive optics.

In acoustics, the piezoelectric composite shells represent an interface between two acoustic media. Existence of such an interface affects tremendously the sound wave propagation through it. It is known that, when the incident sound wave hits the shell, it makes the shell vibrate. The shell vibration causes that a part of the incident sound wave is reflected and a part is transmitted. It will be shown that by controlling the amplitude of the shell vibration, it is possible to control the amplitudes of the reflected and transmitted waves. Such a principle offers a simple approach for a construction of noise control systems.

A physical parameter, which expresses the sound shielding efficiency of noise control systems, is called the acoustic transmission loss. Therefore, a considerable part of the Thesis is devoted to the analytical calculation or numerical computation of the acoustic transmission loss of several systems with piezoelectric composite shells. It will be demonstrated that by connecting the piezoelectric composite shell to an active electric (shunt) circuit, it is possible to control the acoustic transmission loss of the shell. Such an effect can be easily explained by considering the effective elastic properties of the piezoelectric composite shell shunted by an active electric circuit. It will be shown that acoustic transmission loss of the shell is increased, when the effective Young's modulus or the bending stiffness coefficient of the shell are increased. Such an increase in the elastic parameters of the piezoelectric composite shell can be achieved by the proper construction and adjustment of the shunt circuit connected to the piezoelectric actuators in the piezoelectric composite shell.

The numerical computation of the acoustic transmission loss can be divided into two steps. In the first step, it is necessary to investigate the effect of the shunt circuit on the elastic properties of the piezoelectric actuator, which is attached to the glass shell. In the second step, the effect of the elastic parameters of the piezoelectric actuator on the acoustic transmission loss of the piezoelectric composite shell is analyzed. In the presented work, the utilization of so called the Macro-Fiber-Composite (MFC) actuator is considered, since it is suitable for easy attachment to flat or curved glass shells. In accord with the aforementioned approach and due to geometrical complexity of the MFC actuator, the numerical model of the MFC actu-

ator based on the finite element method (FEM) is developed. The FEM model of the MFC actuator has been used for the numerical computation of effective elastic parameters, macroscopic piezoelectric constants, and the capacitance per unit area of the MFC actuator. The effect of the shunt electric circuit on the macroscopic properties of the MFC actuator is analyzed and the method for the determination of optimal shunt circuit parameters that yield maximum values of effective Young's moduli is presented. Then, a detailed analysis of the particular geometry of the glass plate and the arrangement of MFC actuators on the glass plate is performed using a FEM model. Finally, the functionality of the approach and the developed numerical models are verified using acoustic experiments.

In the last part of the Thesis, an application of electronic control of the shape of planar structures in adaptive optics is introduced. An optimization of several geometric parameters of a deformable mirror that consists of a nickel reflective layer deposited on top of a thin piezoelectric PZT disk to get the maximum actuator stroke is presented using the FEM simulations of the layered composite structure.

Keywords:

Acoustics, Adaptive Optics, Planar Structure, Glass window, Macro Fiber Composite piezoelectric actuator, Noise Transmission Control, Elastic properties control, Active circuit, Negative capacitor, FEM simulations.

Abstrakt

Dizertační práce se zabývá tématem studia možností aktivního ovládání statické a dynamické mechanické odezvy systémů plošných struktur za pomoci piezoelektrických aktuátorů připevněných ke struktuře. Plošné struktury, uvažované v práci, jsou tvaru rovinných či zakřivených piezoelektrických kompozitních skořepin. Bude ukázáno, že takováto piezoelektrická kompozitní struktura může být efektivním a poměrně jednoduchým mechatronickým systémem využitelným v akustice nebo v adaptivní optice.

V akustice většinou plošné struktury představují rozhraní mezi dvěma akustickými prostředími. Vlastnosti takového rozhraní vždy ovlivňují zvukovou vlnu, která se skrze něj šíří. Je všeobecně známo, že pokud zvuková vlna narazí na překážku, kterou je plošná struktura, způsobí vibrace této struktury. Tyto vibrace pak způsobí to, že část zvukové vlny se od vibrující struktury odrazí a část jí projde na druhou stranu. Bude ukázáno, že kontrolou amplitudy vibrací plošné struktury je možné kontrolovat i amplitudy odražených a přenesených zvukových vln. Tato myšlenka je základem přístupu k tlumení hluku prezentovaného v dizertační práci.

Fyzikální veličina, která měří přenos zvuku skrz strukturu, se nazývá akustická přenosová ztráta. Značná část práce je proto věnována analytickému výpočtu nebo numerickým simulacím akustické přenosové ztráty několika systémů piezoelektrických kompozitních skořepin. Bude ukázáno, že paralelním připojením piezoelektrické kompozitní skořepiny k aktivnímu elektronickému obvodu je možné ovládat její akustickou přenosovou ztrátu. Ve své podstatě aktivní elektronický obvod ovládá elastické vlastnosti piezoelektrického prvku připojeného ke struktuře a bude dokázáno, že tímto způsobem lze ovládat elastické vlastnosti celé kompozitní skořepiny. Pokud se efektivní Youngův modul nebo koeficient ohybové tuhosti piezoelektrické kompozitní struktury podaří zvýšit, akustická přenosová ztráta se zvýší. Zvýšení hodnot elastických parametrů piezoelektrické kompozitní skořepiny lze dosáhnout správným nastavením napěťového obvodu paralelně připojeného k piezoelektrickým aktuátorům v kompozitní struktuře.

Numerické výpočty akustické přenosové ztráty pomocí metody konečných prvků (FEM) mohou být rozděleny do dvou kroků. V prvním kroku je nutné zjistit, jaký efekt má paralelně připojený elektronický obvod na elastické parametry piezoelektrického aktuátoru, který je připevněný ke skleněné skořepině. V druhém kroku je třeba analyzovat vliv elastických parametrů piezoelektrického aktuátoru na akustickou přenosovou ztrátu celé struktury. V této práci je jako piezoelektrický aktuátor uvažován tzv. macro fiber composite (MFC) actuator, protože je vhodný k připevnění k plochým i zakřiveným strukturám, jako jsou skleněné skořepiny. Díky tomu, že MFC aktuátor má neobyčejně složitou geometrii skládající se

z mnoha mikroskopických PZT vláken, je nutné nejprve vyvinout numerický model pouze MFC aktuátoru. Tento model slouží k výpočtu efektivních elastických parametrů, makroskopických piezoelektrických koeficientů a kapacity na jednotkovou plochu MFC aktuátoru. Poté je možné zařadit do výpočtu vliv paralelně připojeného elektronického obvodu na makroskopické vlastnosti MFC aktuátoru. Je také ukázána metoda, jak optimálně určit parametry aktivního elektronického obvodu, které způsobí maximální hodnotu makroskopických Youngových modulů MFC aktuátoru. A nakonec je pomocí FEM modelu provedena detailní analýza konkrétní geometrie skleněné desky, na niž jsou určitým způsobem rozmístěny MFC aktuátory. Funkčnost vyvinutých FEM modelů je dále ověřena pomocí experimentů měření akustické přenosové ztráty a plošného rozložení výchylky pomocí digitální holografie.

V poslední části práce je uveden příklad aplikace elektronického řízení tvaru plošných struktur v adaptivní optice. Tato část je věnována takové optimalizaci několika geometrických parametrů deformovatelného zrcadla, které se skládá z odrazné niklové plochy nanesené na povrchu tenkého PZT disku, aby bylo dosaženo maximálních výchylek PZT aktuátoru. Analýza je opět provedena pomocí FEM simulací vrstvené kompozitní struktury, tentokrát niklu a PZT.

Keywords:

Akustika, Adaptivní optika, Plošná struktura, Skleněné okno, Macro Fiber Composite piezoelektrický aktuátor, Kontrola šíření hluku, Kontrola elastických vlastností, Aktivní obvod, Negativní kapacita, FEM simualce.

Acknowledgements

First of all, I would like to express my gratitude to my dissertation thesis supervisor, doc. Ing. Pavel Mokrý, Ph.D. He has been a constant source of encouragement and insight during my research and helped me with numerous problems and professional advancements.

I would like to thank to Ing. Vít Lédl, Ph.D. and his research group, namely Ing. Roman Doleček and Ing. Pavel Psota, for their professional attitude to the optical measurement, which helped to improve the quality of this work. Then I would like to thank to doc. Ing. Antonín Potěšil, CSc. for providing a measurement equipment, particularly the Laser Doppler Vibrometer, for the acoustic experiments.

I would like to express my thanks to my colleagues, namely Ing. Jan Václavík, Ing. Martin Černík, Ph.D., Ing. Miloš Kodejška and Ing. Pavel Márton, Ph.D., for their valuable comments during the scientific work and for helping me with the electronics and measuring software solutions.

Special thanks go to the staff of the Institute of Mechatronics and Computer Engineering, who maintained a pleasant and flexible environment for my research, especially I have to appreciate the kindness and patience of Jitka Němcová and Anna Engová.

Special thanks belongs also to Ing. Jan Korpnický, Ph.D. who was always helpful with providing partial funding for my research.

Finally, my greatest thanks go to my family, for the patience and care.

Contents

List of Figures

List of Tables

Abbreviations and Symbols

Abbreviations

AEC	active elasticity control
AFC	active fiber composite
ANC	active noise control/cancellation
APSD	active piezoelectric shunt damping
ASAC	active structural acoustic control
DHI	digital holographic interferometry
FEM	finite element method
IDE	interdigital electrode
LQG	linear quadratic gaussian methods
MFC	macro fiber composite
NC	negative capacitor
PCT	piezoceramic composite transducer
PML	perfectly matched layer
PSD	piezoelectric shunt damping
PVDF	polyvinyledene difluoride
PZT	lead zirconate titanate
RVE	representative volume element
SPL	sound pressure level
SSC	switching shunt control
TL	acoustic transmission loss

Symbols of physical variables and constants

a (m)	length dimension (x axis direction) of the glass plate/shell
A (m^2)	area of the electrodes of piezoelectric actuator
b (m)	width dimension (y axis direction) of the glass plate/shell/layered composite structure
B (Pa)	bulk modulus of the acoustic medium

c (m·s^{-1})	sound velocity in the air
C (F)	capacitance (of the NC circuit)
C_0 (F)	reference capacitance in a NC circuit
C_S (F)	static capacitance of a piezoelectric element
$C_{S,0}$ (F)	static capacitance of the MFC actuator
$C_{S,\omega}$ (F)	static capacitance of the MFC actuator driven by a harmonic voltage
c_{ijkl}, $c_{\lambda\mu}$ (Pa)	elastic stiffness tensor components
d_{ikl}, $d_{i\lambda}$ (C·N^{-1})	piezoelectric coefficient tensor components
$\mathbf{D}$ (C·m^{-2})	electric displacement field vector
D_i (C·m^{-2})	dielectric displacement field vector components
dx (m)	differential of x
dy (m)	differential of y
e_x, e_y, e_{xy} (1)	mechanical strain tensor components along the coordinates x, y, xy
$\mathbf{E}$ (V·m^{-1})	electric field vector
E_i (V·m^{-1})	electric field vector components
e_{ikl}, $e_{i\lambda}$ (N·C^{-1})	piezoelectric coefficient tensor components
f (Hz)	frequency
$\mathbf{f}$ (N·m^{-2})	local surface external force vector
f_x (N·m^{-2})	local surface external force component in the x direction
f_y (N·m^{-2})	local surface external force component in the y direction
$\mathbf{f}_{\mathrm{fr}}$ (N)	reaction force from the spring system of the frame of the glass plate
F_1 (N)	external force component in the x direction
g_{ikl}, $g_{i\lambda}$ (m^2·C^{-1})	piezoelectric coefficient tensor components
G (Pa)	bending stiffness coefficient
G_{ij} (Pa)	shear modulus component of an orthotropic material
h (m)	thickness in general/thickness of the glass plate/shell
h_f (m)	thickness of the piezoceramic fiber in the MFC actuator
h_{MFC} (m)	thickness of the MFC actuator
h_{Ni} (m)	thickness of the nickel reflective layer of the deformable mirror
h_{PZT} (m)	thickness of the PZT layer of the deformable mirror
h_{ikl}, $h_{i\lambda}$ (V·m·N^{-1})	piezoelectric coefficient tensor components
k (m^{-1})	wave number

k_{fr} (N·m^{-1})	effective spring constant of the frame of the glass plate
k_{ijk}, $k_{i\lambda}$ (1)	electromechanical coupling factor
l (m)	RVE (of the MFC actuator) length
L (m)	wavelength
M_x M_y, M_{xy} (kg·m·s^{-1})	moments of bending forces
$\mathbf{n}$ (1)	outer normal vector
n_i (1)	outer normal vector i-th component
N	number of layers of the layered composite structure
N_x, N_y (Pa)	normal stresses along the coordinates x, y
p (Pa)	acoustic pressure
P (Pa)	amplitude of acoustic pressure
p_i (Pa)	incident acoustic pressure
P_i (Pa)	amplitude of incident acoustic pressure
p_r (Pa)	reflected acoustic pressure
P_r (Pa)	amplitude of reflected acoustic pressure
p_t (Pa)	transmitted acoustic pressure
P_t (Pa)	amplitude of transmitted acoustic pressure
$\mathbf{P}_R$ (C·m^{-2})	remnant polarization
Q (C)	electric charge
R (m)	radius of a double-layer sandwich composite structure of the deformable mirror
R_0 (Ω)	tunable resistance in a NC circuit
R_1 (Ω)	tunable resistance in a NC circuit
R_x (m)	radius of curvature along the x
R_y (m)	radius of curvature along the y
S (m^2)	surface area
$\mathbf{S}$ (1)	mechanical strain tensor
S_{ij}, S_λ (1)	mechanical strain tensor components
s_{ijkl}, $s_{\lambda\mu}$ (Pa^{-1})	elastic compliance coefficient tensor components
t (s)	time
$\mathbf{T}$ (Pa)	mechanical stress tensor
T_{ij}, T_λ (Pa)	mechanical stress tensor components
T_x, T_y, T_{xy} (Pa)	mechanical strain tensor components along the coordinates x, y, xy
TL (dB)	acoustic transmission loss
$\mathbf{u}$ (m)	displacement vector
u_i (m)	displacement vector i-th component
u_x (m)	tangential component of the displacement/displacement component in the x direction
u_y (m)	tangential component of the displacement/displacement component in the y direction
u_z (m)	displacement component in the y direction

U_e (J)	electrical energy per unit volume
U_m (J)	mechanical energy per unit volume
v (m·s^{-1})	particle velocity & vibration velocity
V (m·s^{-1})	amplitude of vibration velocity
V (m^3)	volume
V (V)	electric voltage/potential
V_0 (V)	testing voltage
V_x (V·m^{-1})	partial derivative of the electrostatic potential V with respect to x
V_y (V·m^{-1})	partial derivative of the electrostatic potential V with respect to y
w (m)	normal component of the displacement
w_e (m)	width of epoxy gap between two PZT fibers in the MFC actuator
w_f (m)	width of the PZT fiber in the MFC actuator
W (m)	amplitude of the normal component of the displacement
x (m)	orthogonal coordinate
y (m)	orthogonal coordinate
Y (Pa)	Young's modulus
Y_{ii} (Pa)	Young's modulus component of an orthotropic material
z (Pa·s·m^{-3})	acoustic impedance
Z_0 (Pa·s·m^{-1})	characteristic acoustic impedance
Z (Pa·s·m^{-1})	specific acoustic impedance
Z_a (Pa·s·m^{-1})	specific acoustic impedance of air
Z_w (Pa·s·m^{-1})	specific acoustic impedance of the window
α (1)	ratio of the shunt circuit capacitance over the piezoelectric element static capacitance
β_{ij} (m·F^{-1})	impermittivity tensor components
γ (Pa)	elastic stiffness of the "surface" region of the RVE element
γ_{23}, γ_{13}, γ_{12} (1)	engineering shear strains
ϵ_0 (F·m^{-1})	vacuum permittivity
ϵ_{ij} (F·m^{-1})	electrical permittivity tensor components
ϵ_r (1)	relative electrical permittivity
ζ (1)	ratio of the optimal value $R_{0,\mathrm{opt}}$ of the tunable resistor over its current value R_0
ζ_x, ζ_y, $\zeta_x y$ (1)	curvature changes
Θ (K)	thermodynamic temperature
η (1)	dielectric loss factor
η_S (1)	dielectric loss factor of the piezoelectric sample
ν (1)	Poisson's ratio

ν_{ij} (1)	Poisson's ratio component of an orthotropic material
ξ (m^{-1})	curvature of the shell
ξ_x (m^{-1})	curvature along the x
ξ_y (m^{-1})	curvature along the y
ξ (m)	coordinate direction in which the PML absorbs acoustic waves
ξ (1)	ratio of the optimal value $R_{1,\mathrm{opt}}$ of the tunable resistor over its current value R_1
ϱ ($\mathrm{kg{\cdot}m}^{-3}$)	mass density of a material
ϱ_0 ($\mathrm{kg{\cdot}m}^{-3}$)	air density
σ ($\mathrm{J{\cdot}K}^{-1}$)	entropy
ω ($\mathrm{rad{\cdot}s}^{-1}$)	angular frequency
ω_0 ($\mathrm{rad{\cdot}s}^{-1}$)	tuning angular frequency at which the condition for the infinite Young's modulus is satisfied

Commonly used mathematical symbols

$\mathbf{I}$	second-order identity matrix
i	index from 1 to 3 OR imaginary unit
j	index from 1 to 3
k	index from 1 to 3
l	index from 1 to 3
m	Fourier's series index
n	Fourier's series index
λ	index from 1 to 6 (in Voigt notation)
μ	index from 1 to 6 (in Voigt notation)
∇	Del operator (gradient operator), represented by the nabla symbol
Δ^2	biharmonic operator

Chapter 1

Introduction

1.1 Motivation

The past few decades have been dedicated to an integration of active materials into a variety of host structures by means of measuring and controlling their shape and behavior. Materials science and structural engineering have focused on a development of advanced (smart) materials and their applications to structures with enhanced functionality. While there exist many types of smart materials, such as shape memory alloys, electrostrictive or magnetostrictive materials, piezoelectrics remain the most widely used ones for a number of reasons. They have a unique ability to convert the electrical energy into mechanical strain energy, and vice versa. Piezoelectric ceramics have a high structural stiffness, which allows them a strong, voltage-dependent actuation capability. In addition, piezoelectrics can interact with dynamic systems in a wide range of frequencies from zero up to a megahertz range. Nowadays, piezoelectric materials have been used in numerous applications to enhance the performance of aerospace structures, automobiles and sporting equipment by performing shape control and vibration and acoustic noise reduction.

It is known that the vibration of large planar structures (e.g. airplane wings, large windows, glass facades or various flexible panels) results in a serious material fatigue, weakening joints, increase in skin friction, or an unpleasant noise produced directly by vibrating structures. All these bothering effects represent a stimulation for a research of sophisticated methods for the suppression of vibration and noise transmission through large planar structures. Realization of such methods has become a big contemporary challenge for scientists and researchers in the fields of mechanical engineering and acoustics. Therefore, the objective of the dissertation thesis (Thesis) is to develop methods for the noise suppression through planar structures.

Nowadays, the noise suppression became an environmental problem because people in cities are exposed to many harmful influences on their health caused by the unpleasant noise. In the quest of prevention the hearing illnesses, it seems to be reasonable to suppress the noise at places where people live and work. It is a quite hard task, because the intensity of the noise in cities is becoming permanently bigger and passive noise suppression methods are not sufficient, especially in the low frequency range (up to 1 kHz). On the other hand, active noise suppression methods work well in a low frequency range (up to 1 kHz) but they require complicated control algorithms and very fast electronics. There is a big challenge for researchers in a broad variety of scientific fields to invent advanced noise suppression methods with a strong accent on the interdisciplinary interaction. The new approach of modern noise suppression methods should be based on the sound transmission control. Besides other things, the most important requirements for these methods is the noise suppression system effectiveness in wide frequency range, especially between 2 and 5 kHz, where the human hearing is inclined to be easily harmed [1, 2]. These aforementioned issues have become a motivation for the Thesis.

1.2 Problem Statement

The key objective of the Thesis is the study of possibilities of a precise active control of static and dynamic mechanical response of planar structures. There exist two possible groups of applications, where the controlled planar structures can be used. The first group of applications is in structural acoustics, where the planar structures (windows or glazed facades) represent major paths of noise transmission into a building interior. They can be actively controlled by means of their acoustic impedance. The second group of application, where the tuned planar structures can be used, is adaptive optics, where the most commonly used planar structures as wavefront correctors are large diameter deformable mirrors, which require a fast response time and a strong actuation stroke. In order to achieve large deflections over the surface of the planar structures, devices based on piezoelectric layer composite structures actively controlled by the electric field are designed. An analysis of fundamental properties of such systems is the main objective of the Chapters presented below. The basic principles of the vibrational control of planar structures are explained and demonstrated on a simple example of a sound transmission through a glass plate window.

Today, there exist several passive noise control techniques, which are based on the application of elements, such as massive walls, rubber layers, porous materials, etc. Such methods are relatively cheap and efficient in high frequency range. However, it is clear that they can be hardly applicable to large glass windows or facades. At the same time, there exist conventional active noise control techniques. These methods are efficient in the low frequency range, but it is difficult to find their implementation that would be both efficient in a broad frequency range and financially acceptable. The third category of noise suppression methods is based on the semi-active control approach, which profitably balances the advantages of both passive and active approaches: a high efficiency, a simple technical implementation, a minimal weight and size, a low cost, and small external power supply. This technique is in literature commonly referred to as a piezoelectric shunt damping (PSD). It uses the piezoelectric actuator mechanically attached to the structure and electrically shunted by passive or active electrical networks. This promising approach is characterized by utilization of piezoelectric materials in an alternative way based on a simultaneous sensing and actuation performed by a single either monolithic or composite piezoelectric actuator, which is connected to a one-port shunt circuit.

1.3 Contributions of the Thesis

A relevance of the problem solved in the Thesis can be measured in terms of approach originality, global social benefits, and potential commercial profits. The approach presented in the Thesis offers a promising method for the control of the static and dynamic deformations of planar structures. In Thesis, there is analyzed and verified the functionality of the method on a system for the suppression of noise transmission through the glass windows using the active control of the acoustic impedance of the glass plate with attached piezoelectric actuators shunted by an active electric circuit. The advantages of this method stem from its generality and simplicity, offering an efficient tool for the control of the noise transmission through glass windows, especially in the low-frequency range, in which passive methods are inefficient.

The social benefits can be found in the contribution to reduction of the urban and traffic noisiness in buildings and consequently to living and working comfort increase.

From the commercial point of view, the noise control method based on the piezoelectric shunt damping can bring an affordable higher comfort of services such as transport or accommodation thanks to an inexpensive and effective noise reduction. Potential success of the applied technology would lead to a higher competitiveness of the final services and products on the world markets thanks to its low costs and the efficiency in a wide range of frequencies.

1.4 Structure of the Thesis

The Thesis is organized into 6 chapters as follows:

- *Chapter 1. Introduction* describes the motivation behind the work efforts together with the goals. There is also a list of contributions of this Thesis and briefly indicated the outline.

- *Chapter 2. Background and State-of-the-Art* introduces the reader to the necessary theoretical background and surveys the current state-of-the-art. The theoretical background presents basics about smart materials and puts emphasis on piezoelectric materials. Also, there is defined the acoustic transmission loss (TL) as the main physical quantity evaluating the sound shielding efficiency of the interface between two acoustic media. The literature review of the state of the art in the field of noise control through the plates is presented. The survey is focused on the noise transmission control using smart, especially piezoelectric materials.

- *Chapter 3. Theoretical modelling of the acoustic impedance of a curved glass shell and the principles of active elasticity control method* determines the most important features of the noise transmission through planar structures using the approximative analytical model of the specific acoustic impedance of the curved shell. It is demonstrated that by an active piezoelectric layer attached to the planar structure it is possible to control the effective elastic properties of the whole structure. Also, the basic theoretical aspects of active control of effective elastic properties of piezoelectric materials are explained.

- *Chapter 4. Active elasticity control of macro fiber composite actuator* introduces a macro fiber composite (MFC) actuator such as active piezoelectric layer which could be attached to a vibrating structure without cracking. The static and dynamic response of the MFC actuator is analyzed in detail using finite element method (FEM) simulations. Computation of its effective material properties and demonstration of tuning its effective elastic constants by means of a shunt electric circuit is presented in this Chapter. Particularly, it is solved the effect of the shunt circuit with a negative capacitance (NC) on the effective elastic properties of the MFC actuator.

- *Chapter 5. Glass plate noise transmission suppression by means of distributed MFC actuators shunted by the negative capacitance circuit*: The objective of the study presented in this Chapter is to analyze the most efficient ways for suppression of noise transmission through the glass plates using active elasticity control of attached piezoelectric MFC actuators. A detailed analysis of the FEM model implementation of the particular arrangement of MFC actuators on the glass plate is performed. A simple experimental setup for the approximative measurements of the acoustic transmission loss is described. Results of the FEM model simulations and their comparison with experimental data are presented.

- *Chapter 6. Application of the active shape control of the planar structure to adaptive optics* introduces the deformable mirrors as the most commonly used wavefront correctors in adaptive optics systems. An optimization of several geometric parameters of a deformable mirror that consists of a nickel reflective layer deposited on top of a thin piezoelectric PZT disk to get the maximum actuator stroke is presented using the FEM simulations of the layered composite structure.

- *Conclusions*: Summarizes the results of the research presented in the Thesis.

Chapter 2

Background and State-of-the-Art

This Chapter introduces the reader to the necessary theoretical background about piezoelectric materials and acoustic transmission loss and surveys the current state-of-the-art of the noise transmission control through the planar structures.

2.1 Theoretical Background

In this Section, there will be given fundamental information about piezoelectric materials. The Chapter introduces the mathematical description of the piezoelectric effect to an extent, which is necessary for understanding its applications to the noise control through planar structures presented in the Thesis. For more extensive information, the reader should consult literature dedicated to the field of piezoelectrics such as in [3] or [4]. Useful information can be found in the IEEE Standard on Piezoelectricity [5] and more popular reading with recent aspects of the field of piezoelectricity is published in [6].

In addition, the acoustic transmission loss (TL) as the main physical quantity that measures/expresses the sound shielding efficiency of the device will be introduced.

2.1.1 Piezoelectric materials

Piezoelectric materials or piezoelectrics constitute a special group of materials, which belongs to so called *smart materials*. Generally, smart materials are divided into groups according to the kind of energy transformation, such as light–mechanical, chemo – mechanical, thermo – mechanical, magneto – mechanical and electro – mechanical. The majority of systems with smart materials have two basic functions, which are sensing and actuation. The sensor or detection capabilities are used to measure physical quantities by converting them into signals, which can be read by an observer. According to the nature of a smart material, different physical quantity can be measured, e.g. changes in mechanical stress, strain, displacement, velocity, acceleration, electrical or thermal change of the structure. Actuators are used to change the physical quantities by the source of energy, usually the electrical signal, and convert that energy into some kind of motion. By actuation one can change e.g. structural stiffness or geometrical configuration.

Once smart materials are bonded to or embedded in traditional structures (as host structures), those structures now can have sensing or actuating and even controlling capabilities. They are known as intelligent structures or smart structures. Nowadays, the smart structures are used widely in structural engineering. For more detail information the reader can see e.g. [7] or [8].

In the wide range of smart materials the most commonly used electro - mechanical transducers are piezoelectric materials. They provide excellent actuation and sensing capabilities, which are very valuable, e.g., in structural vibration control applications.

Now, some important highlights from the history of piezoelectricity and its applications are presented. The ability of piezoelectric materials to transform mechanical energy into electrical energy, i.e. direct piezoelectric effect, was discovered more than a century ago by Pierre and Jacque Curie, when electric charges were generated by mechanical stress on the surface of tourmaline crystals [9]. It was clearly understood that symmetry of the crystal plays a decisive role in the piezoelectric effect. However, the deformation or stress caused by applied electric field, i.e. converse piezoelectric effect, Curie brothers could not predict. This important physical phenomena was mathematically deduced from the fundamental thermodynamic principles by Lippmann [10]. The existence of the converse effect was immediately confirmed by Curie brothers in the following publication [11].

The first serious application for piezoelectric materials appeared during the World War I. This work is credited to Paul Langevin and his co-workers in France, who built an ultrasonic submarine detector. Their transducer was a mosaic of thin quartz crystals glued between two steel plates (the composite having a resonant frequency of about 50 kHz, mounted in a housing suitable for immersion) [12]. Then, after the World War II the piezoelectric effect started to be used in the industry with applications ranging from mentioned underwater sonars to medical imaging systems or car accelerometers. This evolution was possible mainly due to the invention of piezoelectric ceramics, which contain microscopic piezoelectric grains, in which the averaging of piezoelectric responses results in the high symmetry (∞mm) macroscopic state with only a few independent effective piezoelectric coefficients (see e.g. [13]). This research has resulted in the astonishing performance of piezoelectric materials with industrial applications in many areas.

Nowadays, piezoelectric transducers are of many types and available in many forms and shapes. As mentioned, piezoelectric effect can be observed in various types of materials, such as single crystals (e.g. quartz, barium titanate, lithium niobate), ceramics (e.g. lead zirconate titanate (PZT)), thin epitaxial films (e.g. the layer of PZT of the thickness of the order of μm and mm), polymers (e.g. polyvinylidene fluoride (PVDF)), or various composite structures. For more detailed overview of these types of materials, the reader should take a look at the recent publication edited by Safari and Akdogan ([14]).

In next Subsections, a more detailed description of piezoelectric ceramics is given, since it is the most commonly used piezoelectric material. According to the application and the function, which the piezoceramic transducer should provide, there is possible to find many shapes of piezoceramic components such as simple discs, tubes, plates, stacks, unimorphs or bimorphs. In addition, the piezoelectric ceramic can be a part of numerous composites (see e.g. the websites of leading piezoceramic producing companies [15], [16] or [17]). Currently, the search for new technologies has resulted in advanced composites from PZT that are light in weight, shape flexible and high in strength and stiffness compared to more conventional material systems. The possibility to use these piezoelectric composite structures contributed to being of the motivation of the Thesis. Next paragraph briefly introduces the basic material properties of piezoelectric ceramics.

2.1.1.1 Piezoelectric PZT ceramics

The piezoelectric PZT ceramics is a polycrystalline ferroelectric material with the perovskite crystal structure. Each crystal lattice unite cell is composed of a small, tetravalent metal ion (Zr or Ti) placed inside a lattice of larger divalent metal ions (Pb) and O_2, as shown in Fig. 2.1.1.1.

To prepare a piezoelectric ceramic, fine powders of the component metal oxides $PbTiO_3$ and $PbZiO_3$ are mixed in specific proportions. This mixture is then heated to form a uniform powder. The powder is then mixed with an organic binder and is formed into specific shapes, e.g. discs, rods, plates, fingers, etc. These elements are then heated for a specific time, and under a predetermined temperature. As a result of this process the powder particles sinter and the material forms a dense crystalline structure. Finally, electrodes of the desired size and shape are applied to the

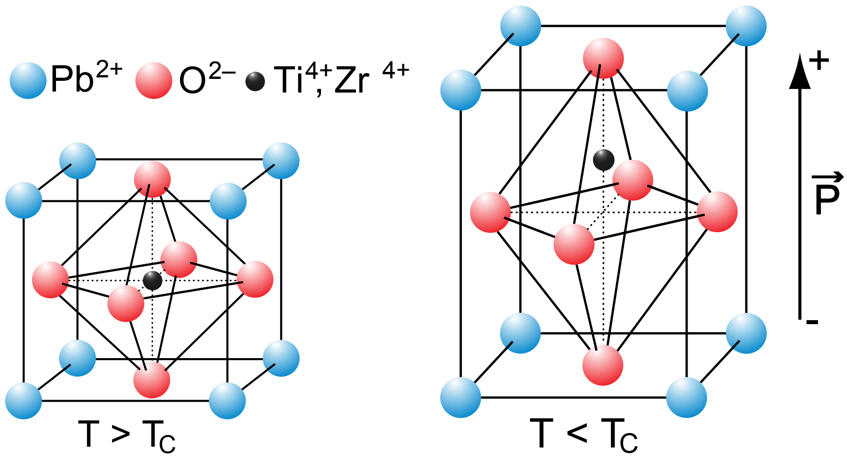

(a) (b)

Figure 2.1: Crystalline structure of a piezoelectric PZT ceramic, (a) above the Curie temperature, the material exhibits a simple cubic symmetry with no spontaneous polarization, (b) below the Curie temperature, the material has now tetragonal symmetry which is associated with a spontaneous polarization, [18, 19].

appropriate surfaces of the structure [20].

Above a critical temperature, known as the Curie temperature, each perovskite crystal exhibits a simple cubic symmetry with no spontaneous polarization, as demonstrated in Fig. 2.1(a). On the other hand, at temperatures below the Curie temperature, the lattice structure becomes deformed and asymmetric in the way that the tetravalent metal ion (Zr or Ti) in the middle of the lattice is moved from the center position and each crystal lattice unite cell has now tetragonal symmetry which is associated with a spontaneous polarization of the ferroelectric ceramics (Fig. 2.1(b)).

Regions within a material which has uniform spontaneous polarization are called domains. Because of chaotic ordering of the individual piezoelectric grains in the whole volume of the material, the direction of polarization among neighboring domains is random, as demonstrated in Fig. 2.2(a). Subsequently, the piezoceramic element has zero average polarization. By applying the strong DC electric field, the domains in the piezoceramic element are aligned along the direction of the field (Fig. 2.2(b)) and even after the electric field is removed most of the domains are locked into a position near the alignment, i.e. the piezoelectric ceramic has nonzero average polarization.

It must be said that PZT and other perovskite structure materials are so called tri-axial ferroelectrics. That means that the tetravalent metal ion could be moved from the center position in three perpendicular direc-

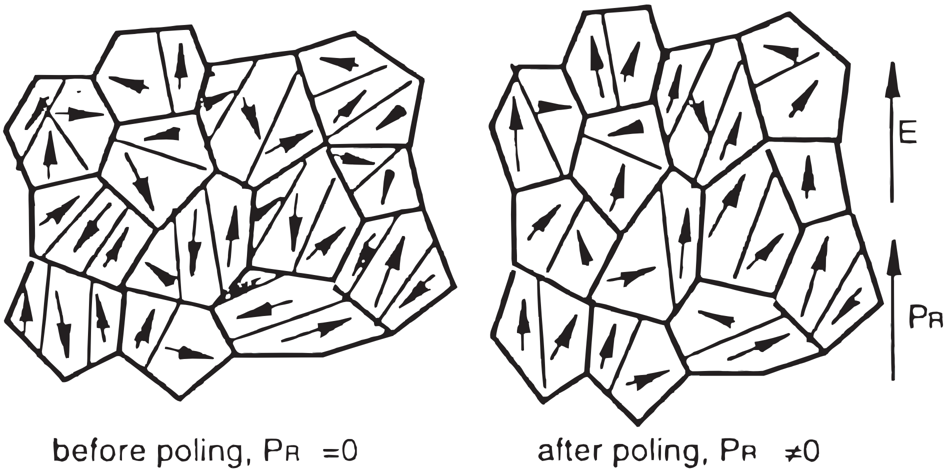

(a) (b)

Figure 2.2: Poling process of PZT: (a) Before the polarization the domains are oriented randomly, (b) DC electric field is used for polarization and after the DC field is removed, the remnant polarization $\mathbf{P}_R$ remains.

tions according to the applied electric field. It is essential that orientation of spontaneous polarization controls the form and the components values of tensors of piezoelectric, dielectric and elastic coefficients. This phenomenon, i.e. a direction of piezoelectric ceramic polarization, is crucial in many applications of the design of sensors/actuators.

As shown in Fig. 2.3, the poled piezoelectric ceramic element, exposed to the mechanical compressive and tensile stresses generates electric fields and hence voltages. Compression along the direction of polarization, or tension perpendicular to the direction of polarization, generates voltage of the same polarity as the poling voltage. Tension along the direction of polarization, or compression perpendicular to that direction, generates a voltage with polarity opposite to that of the poling voltage. When operating in this mode, the device is being used as a sensor using the direct piezoelectric effect. If a voltage of the same polarity as the poling voltage is applied to a ceramic element, in the direction of the poling voltage, the element will lengthen and become thiner in its diameter. If a voltage of polarity opposite to that of the poling voltage is applied, the element will become shorter and broader. If an alternating voltage is applied to the device, the element will expand and contract cyclically, at the frequency of the applied voltage. When operated in this mode, the piezoelectric ceramic is used as an actuator using a converse piezoelectric effect.

The relationship between mechanic and electric energy conversion could be described by basic electromechanical equations, which are presented below.

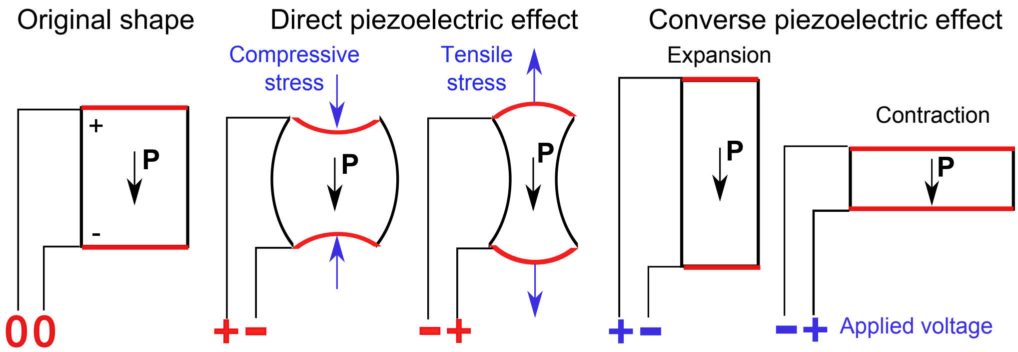

Figure 2.3: Direct and converse piezoelectric effects. When the poled piezoelectric ceramic element is exposed to the mechanical compressive and tensile stresses, it generates electric fields and hence voltages of the polarity according to a direction of applied mechanical stress; If an electrical voltage is applied to a ceramic element, the element will change its shape according to a direction of the applied voltage. [21].

2.1.1.2 Piezoelectric state equations

In this Section, the equations, which describe an electromechanical interaction in a piezoelectric material, are introduced. The interpretation is based on the IEEE standard for piezoelectricity [5]. The mathematical description of the electromechanical interaction in piezoelectrics combines the piezoelectric effect, the electrical behavior of the material and the Hooke's law. These physical phenomena are coupled in the set of two summation equations, where the first one describes the direct piezoelectric effect and the second one describes the inverse piezoelectric effect. In the constitutive equations, it is assumed that the total strain in the transducer is the sum of mechanical strain induced by the mechanical stress and the induced strain caused by the applied electric voltage.

The IEEE standard assumes that piezoelectric materials are linear. That means, that the following relationships comply only with small electrical and mechanical amplitudes. Only in this range of small values it possible for polarized piezoelectric ceramics to be described by linear relationships between the mechanical strain S_{ij} or mechanical stress T_{ij} tensor components and the vector components of the electric field E_i or the dielectric displacement D_i. The mechanical and electrical physical quantities are linked up together through dielectric, piezoelectric and elasticity "constants". They are defined in terms of tensors because of anisotropic material character of piezoelectrics. Every component of the tensor then reflects the directionality of the electric field, the mechanical stress, etc.

The four state variables ($\mathbf{S}$, $\mathbf{T}$, $\mathbf{E}$, and $\mathbf{D}$) can be arranged to give 4 combination sets of piezoelectric constitutive equations. They differ in the coupling matrices of the piezoelectric coefficients. It is possible to transform piezoelectric constitutive data in one form to another form. Assuming the simplified situation, i.e. the thermodynamic state when the temperature Θ or the entropy σ are constant values, the basic relationships between the electrical and elastic properties in piezoelectric materials are expressed in Einstein notation (introduced by Albert Einstein in 1916 [22]) as follows:

$$\begin{aligned} T_{ij} &= c^E_{ijkl} S_{kl} - e_{ijk} E_k \\ D_i &= e_{ikl} S_{kl} + \epsilon^S_{ij} E_j \end{aligned} \tag{2.1a}$$

$$\begin{aligned} T_{ij} &= c^D_{ijkl} S_{kl} - h_{ijk} D_k \\ E_i &= -h_{ikl} S_{kl} + \beta^S_{ij} D_j \end{aligned} \tag{2.1b}$$

$$\begin{aligned} S_{ij} &= s^E_{ijkl} T_{kl} + d_{ijk} E_k \\ D_i &= d_{ikl} T_{kl} + \epsilon^T_{ij} E_j \end{aligned} \tag{2.1c}$$

$$\begin{aligned} S_{ij} &= s^D_{ijkl} T_{kl} + g_{ijk} D_k \\ E_i &= -g_{ikl} T_{kl} + \beta^T_{ij} D_j, \end{aligned} \tag{2.1d}$$

where i, j, k, l are indexes of the material properties and state variables tensors from 1 to 3. As mentioned, T_{ij}, S_{ij}, E_i and D_i refer to the state variables, i.e. the components of the mechanical stress tensor, mechanical strain tensor, electric field vector and dielectric displacement vector, respectively.

Symbols ϵ_{ij} and β_{ij} stand for the electrical permittivity and impermittivity tensor components. The permittivity determines the charge per unit area in the i-axis due to an electric field applied in the j-axis. In this notation, it is assumed that the permittivity is a product of the relative permittivity ϵ_r and the vacuum permittivity (permittivity of free space) $\epsilon_0 \approx 8.854187817$ F·m^{-1}. Furthermore, the superscript T or S refers to the permittivity ϵ^T or ϵ^S, when the material is under constant mechanical stress or strain influence.

Elastic material parameters are expressed by the tensors of elastic compliance coefficients s_{ijkl} and elastic stiffness coefficients c_{ijkl}. Elastic compliance is the ratio of the strain the in ij-direction to the stress in the kl-direction, given that there is no change of stress along the other two directions. Elastic stiffness tensor is the inverse matrix to the elastic compliance tensor. A superscript E is used to state that the elastic compliance s^E_{ijkl} is measured with the electrodes short-circuited. Similarly, the superscript D in s^D_{ijkl} denotes that the measurements were taken when the electrodes were left open-circuited.

And last, d_{ikl}, e_{ikl}, g_{ijk} and h_{ijk} are the symbols indicating the piezoelectric coefficients which differ in terms which state variables are involved in the energy transformation. There are 4 possible combinations of the state variables during the mechanical into the electrical energy and vice versa transformation, so the four piezoelectric coefficients exist. E.g. the piezoelectric coefficient d_{ijk} is the ratio of the induced strain S_{ij} in jk-direction to the electric field E_i applied along the i-axis, when all external stresses are held constant.

Speaking about the variables and parameters expressed by the tensors, it is convenient to implement Voigt notation or Voigt form which in multilinear algebra is a way to represent a symmetric tensor by reducing its order [23]. An example could be demonstrated using the stress tensor which is assumed to expressed by symmetrical matrix:

$$\mathbf{T} = \begin{pmatrix} T_{11} & T_{12} & T_{13} \\ T_{21} & T_{22} & T_{23} \\ T_{31} & T_{32} & T_{33} \end{pmatrix} \tag{2.2}$$

The stress tensor, represented in Voigt notation is given as 6-dimensional vector:

$$\mathbf{T} = (T_{11}, T_{22}, T_{33}, T_{23}, T_{13}, T_{12}) \equiv (T_1, T_2, T_3, T_4, T_5, T_6)\,, \tag{2.3}$$

where the T_1, T_2, T_3 represent the normal components of stress and T_4, T_5, T_6 represent the shear components of stress. It should be noted that for convenience some scaling factors are often introduced when converting tensors into Voigt notation. For example, the off-diagonal (shear) components of the strain tensor are converted such that in Voigt notation they are equal to the engineering shear strain, so they are twice the tensorial shear strain, i.e.:

$$\mathbf{S} = \begin{pmatrix} S_{11} & S_{12} & S_{13} \\ S_{21} & S_{22} & S_{23} \\ S_{31} & S_{32} & S_{33} \end{pmatrix} = (S_{11}, S_{22}, S_{33}, \gamma_{23}, \gamma_{13}, \gamma_{12}) \equiv \tag{2.4}$$

$$\equiv (S_1, S_2, S_3, S_4, S_5, S_6)\,, \tag{2.5}$$

where $\gamma_{23} = 2S_{23}$, $\gamma_{13} = 2S_{13}$ and $\gamma_{12} = 2S_{12}$ are engineering shear strains. Likewise, a three-dimensional symmetric fourth-order tensor of elastic compliances or stiffness can be using the Voigt notation reduced to 6×6 matrix.

If the piezoelectric element is placed into the system of coordinates and assuming the usual situation, i.e. the device is poled along the axis 3, and viewing the piezoelectric material as a transversely isotropic material, which is true for piezoelectric ceramics, many of the material parameters in the matrices will be either zero, or can be expressed in terms of other parameters. In particular, for the non-zero elastic compliance coefficients stands (written in Voigt notation):

$$s_{11} = s_{22} \tag{2.6a}$$

$$s_{13} = s_{31} = s_{23} = s_{32} \tag{2.6b}$$

$$s_{12} = s_{21} \tag{2.6c}$$

$$s_{44} = s_{55} \tag{2.6d}$$

$$s_{66} = 2(s_{11} - s_{12}). \tag{2.6e}$$

The non-zero components of piezoelectric coefficients written in Voigt notation can be reduced in a way

$$d_{31} = d_{32} \tag{2.7a}$$

$$d_{15} = d_{24} \tag{2.7b}$$

and, finally, the non-zero components of the dielectric constant are only the diagonal ones ($\epsilon_{11}, \epsilon_{22}, \epsilon_{33}$) assuming

$$\epsilon_{11} = \epsilon_{22}. \tag{2.8}$$

Subsequently, e.g. the set of Eq. (2.1c) could be simplified and written in a form:

$$\begin{pmatrix} S_1 \\ S_2 \\ S_3 \\ S_4 \\ S_5 \\ S_6 \end{pmatrix} = \begin{pmatrix} s_{11}^E & s_{12}^E & s_{13}^E & 0 & 0 & 0 \\ s_{12}^E & s_{22}^E & s_{13}^E & 0 & 0 & 0 \\ s_{13}^E & s_{13}^E & s_{33}^E & 0 & 0 & 0 \\ 0 & 0 & 0 & s_{44}^E & 0 & 0 \\ 0 & 0 & 0 & 0 & s_{44}^E & 0 \\ 0 & 0 & 0 & 0 & 0 & 2(s_{11}^E - s_{12}^E) \end{pmatrix} \begin{pmatrix} T_1 \\ T_2 \\ T_3 \\ T_4 \\ T_5 \\ T_6 \end{pmatrix} + \\ + \begin{pmatrix} 0 & 0 & d_{31} \\ 0 & 0 & d_{31} \\ 0 & 0 & d_{33} \\ 0 & d_{15} & 0 \\ d_{15} & 0 & 0 \\ 0 & 0 & 0 \end{pmatrix} \begin{pmatrix} E_1 \\ E_2 \\ E_3 \end{pmatrix} \tag{2.9a}$$

$$\begin{pmatrix} D_1 \\ D_2 \\ D_3 \end{pmatrix} = \begin{pmatrix} 0 & 0 & 0 & 0 & d_{15} & 0 \\ 0 & 0 & 0 & d_{15} & 0 & 0 \\ d_{31} & d_{31} & d_{33} & 0 & 0 & 0 \end{pmatrix} \begin{pmatrix} T_1 \\ T_2 \\ T_3 \\ T_4 \\ T_5 \\ T_6 \end{pmatrix} + \\ + \begin{pmatrix} \epsilon_{11}^T & 0 & 0 \\ 0 & \epsilon_{11}^T & 0 \\ 0 & 0 & \epsilon_{33}^T \end{pmatrix} \begin{pmatrix} E_1 \\ E_2 \\ E_3 \end{pmatrix} \tag{2.9b}$$

One of the most important factors, which denote the efficiency of the conversion of the electrical energy into the mechanical energy, or vice versa, is the electromechanical coupling factor k_{ijk}. In Voigt notation it can be simplified to the $k_{i\lambda}$, where λ index ranges from 1 to 6. The indexes indicate that the stress, or strain are applied or developed in the direction λ, and the electrodes of the piezoelectric element are perpendicular to the i-axis. The electromechanical coupling factor measures the square root of converted over input energy fraction [24].

Lets assume that electric field E_j is applied to a piezoelectric material. Taking into account the relation of the electrical energy per unit volume,

$$U_e = \frac{1}{2} D_i E_j = \frac{1}{2} \epsilon_{ij} E_j^2, \tag{2.10}$$

and the stored mechanical mechanical energy per unit volume under zero external stress,

$$U_m = \frac{1}{2} S_\lambda T_\mu = \frac{1}{2} \frac{S_\lambda^2}{s_{\lambda\mu}}, \tag{2.11}$$

the relationship for the electromechanical factor can be expressed in terms of material constants. In particular,

$$k_{i\lambda}^2 = \frac{U_m}{U_e} = \frac{d_{i\lambda}^2}{s_{\lambda\mu} \epsilon_{ij}^T}, \tag{2.12}$$

where for the induced strain in piezoelectric materials holds the relationship $S_\lambda = d_{j\lambda} Ej$. As it could be seen from the Eq. (2.12), the electromechanical coupling factor is a unitless number from 0 to 1.

The electromechanical coupling factor is a very important parameter, because it characterizes the performance efficiency of the piezoelectric transducer. It has also a direct impact on the device bandwidth. For many applications, such as noise or vibration control, the electromechanical coupling factor is a crucial parameter for the design of the shunt electronics.

2.1.2 Acoustic transmission loss

Many environmental noise sources cause vibrations of various structures by the incident acoustic pressure waves. Due to their physical nature, structure vibrations are accompanied with the flow of mechanical or acoustic energy. In Fig. 2.4, it is pictured how the noise can transmit into buildings. The vibrations spread to adjacent structures, whose vibrations can cause the structure-born noise. So, the vibrating structures can be considered as secondary noise sources. If it is succeeded the suppression of this secondary structure-born noise, one does not have to pay attention to the sound fields generated by primary noise sources from outside.

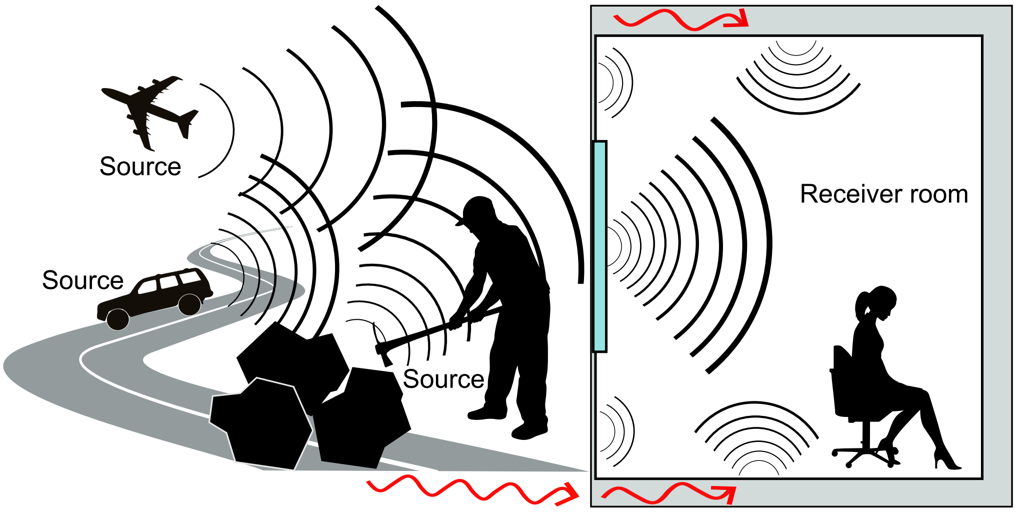

Figure 2.4: Noise transmission paths between an environment and adjacent building/room. Many noise sources cause vibrations of various structures by the incident acoustic pressure wave. The vibrations spread to adjacent structures, whose vibrations can cause the structure-born noise. Here, the major noise transmission path to buildings is the window.

As mentioned in the Introduction, large planar structures (flexible plates or panels), which vibrate, represent a substantial secondary noise source. Typical examples of the panels, through which the noise can be transmitted, include drywall, plywood, glass panels, sheet metal panels or metal roof decks. However, the weakest segments in the noise transmission path from the noisy environment to the building interior are windows or glazed facades. The reason for this is that they usually do not represent an effective noise barrier due to their low flexural rigidity. They are, in principle, thin plates with their edges fixed in a frame. Therefore, it is very easy to make them vibrate by the action of incident acoustic waves. Then, non-negligible part of the wave is transmitted through the window to the building interior.

Any flexible panel, which vibrates in response to the incident sound, will transmit some sound energy to the other side and, therefore, decrease the reflected sound. The effect is most pronounced at low frequencies. Therefore, low frequency absorption is usually highly desirable, but it is very difficult to find some effective and financially acceptable method to achieve it. In addition, the human hearing is inclined to be easily harmed at frequencies between 2 and 5 kHz[2], so it is very important to find some stable and effective way for the suppression of noise through the large planar structures.

In order to quantify the acoustic waves propagation in an acoustic

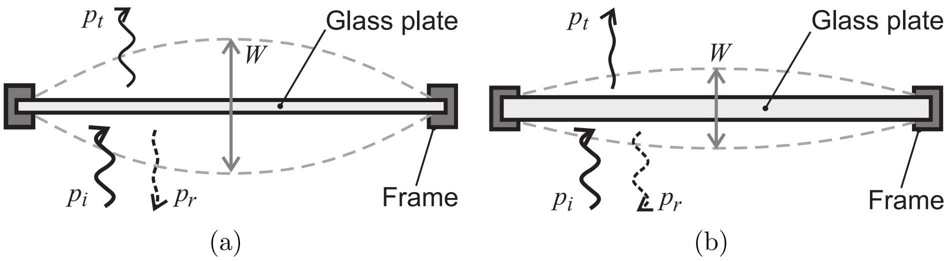

Figure 2.5: (a) Scheme of the considered sound transmission system, which consists of the glass plate fixed in a rigid frame at its edges. The sound source located underneath the glass plate generates an incident sound wave of the acoustic pressure p_i that strikes the glass plate. It makes the glass plate vibrate and a part of the sound wave is reflected and a part is transmitted with the values of the acoustic pressures p_r and p_t, respectively. The dashed line indicates the vibration amplitude W of the glass plate (for simplicity, there is pictured first mode of vibration where the maximal amplitude is formed in the middle of the glass plate and the there are just two nodes at the edges of the plate). The greater the amplitude of vibration is, the greater part of the incident sound wave energy is transmitted to the other side; (b) Scheme of the noise suppression principle: When the vibration amplitude normal to the surface of the glass plate is reduced (e.g. due to being thicker), the greater part of the incident sound wave energy is reflected than transmitted.

medium and the reflection of the sound at the interface of two different media, we define a physical property called the acoustic impedance z (in Pa·s·m^{-3}). It is a frequency-dependent parameter defined as an acoustic sound pressure p divided by particle velocity v and a surface area S, through which an acoustic wave propagates:

$$z = \frac{p}{vS}. \tag{2.13}$$

When dealing with planar structures, it is often convenient to express the acoustic impedance per unit area of the structure, which is made using a physical property called specific acoustic impedance Z (in Pa·s·m^{-1}),

$$Z = \frac{p}{v}. \tag{2.14}$$

If a sound wave propagates through a medium, its wave motion is characterized by a physical property called characteristic acoustic impedance (in Pa·s·m^{-1}):

$$Z_0 = \sqrt{\rho B}, \tag{2.15}$$

where symbols ρ and B stand for the mass density and the bulk modulus of the medium, respectively.

The role of the acoustic impedance in noise and vibration suppression devices can be easily demonstrated on the case of simple glass plate shown in Fig 2.5(a). Let us consider a sound transmission system, which consists of the glass plate fixed in a rigid frame at its edges. The plate creates an interface between two acoustic media of air. The interface is characterized by a specific acoustic impedance of the window Z_w. The sound source located underneath the glass plate generates an incident sound wave of the acoustic pressure p_i that strikes the glass plate. It makes the glass plate vibrate and a part of the sound wave is reflected and a part is transmitted with the values of the acoustic pressures p_r and p_t, respectively. Then, the specific acoustic impedance of the glass plate is defined as

$$Z_w = \frac{p_i + p_r - p_t}{v}, \tag{2.16}$$

which satisfies the equation of motion. Considering that the acoustic impedance is a frequency dependent property, one can work only with the amplitudes of the acoustic pressures, i.e. P_i, P_r, P_t and the amplitude of the vibrations, i.e. W. The frequency dependent specific acoustic impedance is expressed as follows, considering the simple assumption of a harmonic vibration response of the plate:

$$Z_w(\omega) = \frac{P_i(\omega) + P_r(\omega) - P_t(\omega)}{i\omega W(\omega)}, \tag{2.17}$$

where ω is the angular frequency, where $\omega = 2\pi f$, where f is the ordinary frequency in Hz. Assuming that by tuning the acoustic impedance of the planar structure at the interface of acoustic media can be changed the absorbing or reflecting capabilities of the interface, one can achieve devices such as perfectly absorbing surfaces or perfect sound shields.

In practice, the absorbing or reflecting capabilities of the structure are usually evaluated using the physical property called *acoustic transmission loss (TL)*. In noise suppression applications, the acoustic TL denotes the sound shielding efficiency of the interface structure. The value of acoustic TL is defined as a ratio, usually expressed in units of decibels, of the acoustic powers of the incident and transmitted acoustic waves, respectively:

$$\mathtt{TL} = 20 \log_{10} \left| \frac{p_i}{p_t} \right|, \tag{2.18}$$

Knowing the value of the specific acoustic impedance of the glass window Z_w, which is defined by Eq. (2.17), it is possible to derive the acoustic TL as follows: Let us use the simplified picture in Fig. 2.5(a) where the sound wave propagates through the glass shell from the acoustic medium below the shell to the acoustic medium above the glass shell along the z direction.

It is true that membrane velocity equals to (i) the particle velocity in the acoustic medium on the bottom side of the shell equals to the membrane velocity and (ii) the particle velocity in the acoustic medium in the upper side of the shell. This fact can be expressed by the following equation of motion:

$$-\frac{1}{i\omega\rho}\frac{\partial p}{\partial z} = Ve^{i\omega t}, \tag{2.19}$$

where the acoustic pressure p and the medium density ρ (i) at the bottom side of the shell are expressed as

$$p = P_i e^{i(\omega t - \frac{1}{c_0}z)} + P_r e^{i(\omega t + \frac{1}{c_0}z)}, \tag{2.20a}$$

$$\rho = \rho_0, \tag{2.20b}$$

where the symbol c_0 is the velocity of the sound in the acoustic medium below the shell, and (ii) at the upper side of the shell, the pressure is expressed as

$$p = P_t e^{i(\omega t - \frac{1}{c_1}z)}, \tag{2.21a}$$

$$\rho = \rho_1, \tag{2.21b}$$

where the symbol c_1 is the velocity of the sound in the acoustic medium above the shell. Using Eqs. (2.17), (2.19), (2.20a) and (2.21a), it is possible to obtain the following relations for the amplitudes of reflected acoustic pressure P_r, transmitted acoustic pressure P_t and the membrane velocity V:

$$P_r = -\frac{-P_i(Z_w + c_0\rho_0 - c_1\rho_1)}{Z_w + c_0\rho_0 + c_1\rho_1}, \tag{2.22}$$

$$P_t = \frac{2c_1 P_i \rho_1}{Z_w + c_0\rho_0 + c_1\rho_1}, \tag{2.23}$$

$$V = \frac{2P_i}{Z_w + c_0\rho_0 + c_1\rho_1}. \tag{2.24}$$

Then from Eqs. (2.14) and (2.19), it is possible to express the characteristic acoustic impedances Z_0 and Z_1, of the medium below and above the glass shell, respectively:

$$Z_0 = c_0\rho_0 \tag{2.25a}$$

$$Z_1 = c_1\rho_1. \tag{2.25b}$$

One can notice that it is possible to express the transmitted acoustic pressure amplitude, i.e. Eq. (2.23), in terms of characteristic acoustic impedance of the media and specific acoustic impedance of the shell:

$$P_t = \frac{2P_0 Z_1}{Z_0 + Z_1 + Z_w}, \tag{2.26}$$

And finally, when we substitute Eq. (2.26) into the definition formula for the acoustic TL, Eq. (2.18), assuming that the characteristic acoustic impedances of the media below and above the shell are equal, i.e. $Z_0 = Z_1 = Z_a$, where Z_a is the characteristic acoustic impedance of air, and $c_0 = c_1 = c$, where c is the sound velocity in air, and $\rho_0 = \rho_1 = \rho_0$, where ρ_0 is the density of air, we derive in the formula which was presented in [1]:

$$\mathtt{TL} = 20 \log_{10} \left| 1 + \frac{Z_w}{2Z_a} \right|, \tag{2.27}$$

where the acoustic TL is expressed only in terms of specific acoustic impedance of the glass shell/window Z_w.

Since the acoustic TL describes the sound shielding efficiency of the interface structure, it is clear that its value has to be increased in order to decrease the sound transmission through the interface. It can be seen from Eq. (2.27) that the acoustic TL will increase, when the specific acoustic impedance of the window increases. Fig. 2.5(b) presents a scheme of the noise suppression principle that follows from Eqs. (2.16) and (2.27), i.e., the values of specific acoustic impedance Z_w and acoustic TL increase with a decrease in the amplitude of the window vibration velocity v. The window is indicated to be thicker, so the amplitude of the vibrations W is smaller. As a result, the greater part of the incident sound wave energy is reflected than transmitted. In the most of applications, it is not possible or even desirable to make the planar structures, especially windows, thicker. One of the objective of the Thesis is to increase the acoustic TL without rising of the amount of material.

In order to optimize the system and to achieve maximum values of the acoustic TL, it is necessary to understand the dynamics and vibrational response of the glass plate. It is made using mathematical numerical simulations using the finite element method (FEM), which is presented further in next Chapters.

2.2 Review of the noise control methods through the plates

This section introduces a basic overview of methods to control the noise propagation through the plates and includes a literature review. First, there are mentioned conventional methods of the noise attenuation, then the text is focused on new modern methods with pointing out the use of the piezoelectric shunt acoustic control which is further examined in the Thesis.

2.2.1 Passive noise control

The most conventional noise control approach used in practice is an implementation of passive noise control methods. The two important noise-related quantities of a material are the ability to absorb acoustic energy and the ability to reflect or block sound energy. Good absorbing materials allow sound pressure fluctuations to enter their surface and dissipate energy by air friction. They are generally porous and lightweight, such as fiberglass, open cell foam, or acoustical ceiling tiles [25, 26]. Good barrier materials reflect sound, are dense and nonporous, they are e.g. concrete, lead, steel, brick or glass. In general, a single homogeneous material will not be both a good absorber and a barrier. To get the best results, it is common to use an absorbing layer laminated to a barrier material.

So, focused on the plates and particularly windows, the most common methods of passive noise control are based on the laminated glass technology and double glazing [25]. Laminated glass with the different thicknesses of interlayer and glass can improve the acoustical performance by reducing the noise transmission in the fenestration system.

Among the recent works dedicated to the passive noise control through the plates using the layers belongs the work by Araújo et al. [27] who formulated a finite element model by using a mixed layerwise approach for anisotropic laminated plates with viscoelastic core. It is about the optimization of passive damping: maximization of modal loss factor using a gradient based approach. Most recently, Li and Narita [28] present the paper concerning the optimal design for the damping loss factor of laminated plates under general edge conditions. The analysis is based on the classical lamination theory, the loss factor is deduced from the energy formulation for symmetrically laminated thin plates comprised of fiber reinforced layers and viscoelastic layers. The effects of location and thickness of viscoelastic layers on the loss factor of the plates are studied and the fibers orientation angles are also clarified. Their numerical results are successfully compared with the experimental data from the work by Berthelot and Sefrani [29] so their present approach is quite useful in analyzing and designing the loss factor of the plates.

Double glazed windows use two separate panels of glass with an air space between them. Such a double structure has a resonance frequency, which depends on the mass and distance of the plates, and on the stiffness of the cavity medium. At the resonance frequency, the sound insulation is minimal. Above the resonance frequency, the sound proofing capability rises three times faster than below the resonance. Fig. 2.6 shows the sound transmission loss through the commonly used window panels with different approaches of passive damping applied [30]. Solid thin line represents the acoustic transmission loss for the glass plate of thickness 4 mm, solid

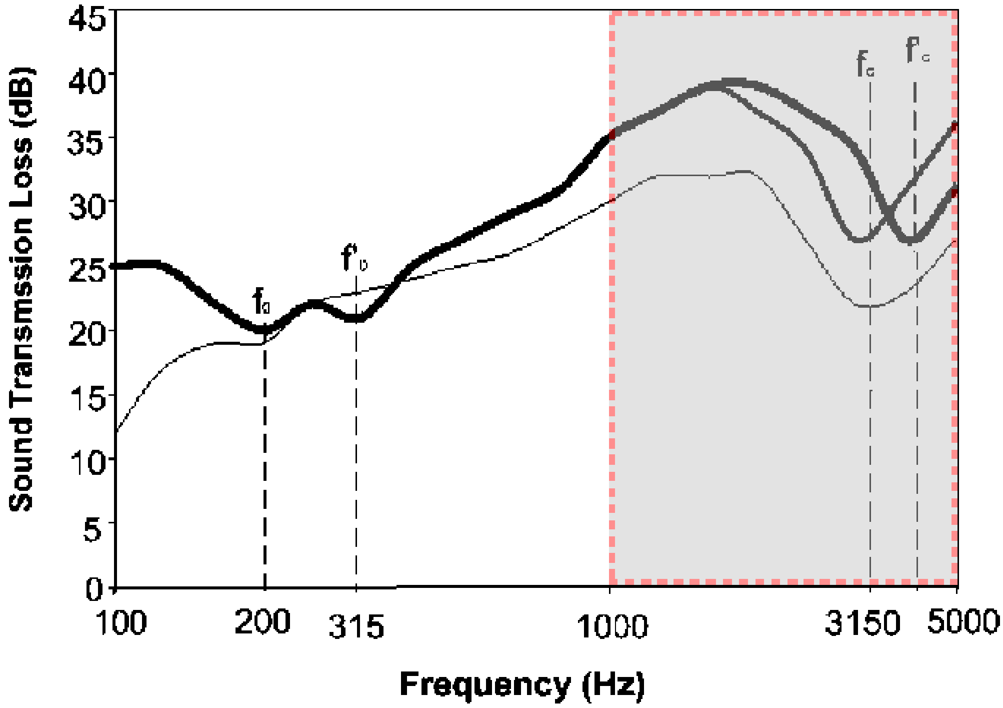

Figure 2.6: Sound transmission loss through the commonly used window panels with different approaches of passive damping applied [30]. Solid thin line represents the acoustic transmission loss for the glass plate of thickness 4 mm, solid medium-thick line represents the acoustic transmission loss for the double glass panel with air gap of thicknesses $4-12-4$ mm and the solid thick line represents the laminated double glass panel with air layer of thicknesses $4-12-2/2$ mm. It is obvious that the both passive methods are efficient in reducing the noise transmission at frequencies higher than 1 kHz. On the other hand, below the double structures resonance acoustic shielding can be even worse than that of a single glass plate.

medium-thick line represents the acoustic transmission loss for the double glass panel with air gap of thicknesses $4-12-4$ mm and the solid thick line represents the laminated double glass panel with air layer of thicknesses $4-12-2/2$ mm. It is obvious that the both passive aforementioned methods are efficient in reducing the noise transmission at frequencies higher than 1 kHz. On the other hand, acoustic performance of the double glazed window deteriorates rapidly below the double structures resonance, where its acoustic shielding can be even worse than that of a single glass plate. Recent work by Legault and Atalla [31] demonstrates an analytical model of the sound transmission of an aircraft sidewall represented by a double panel structure with a fiberglass filling the cavity between the panels. The studied configuration is composed of a trim panel (receiver side panel) attached to a ribbed skin panel (source side panel) with periodically spaced resilient mounts. The investigation of mount stiffness, damping and spacing show that properly designed mounts can increase the sound transmission loss significantly (up to 20 dB of difference between rigid and resilient mounts). They compare the analytical model with FEM simulations which show that the average level of structure-borne transmitted energy is well reproduced with the periodic approach.

Anyway, in order to achieve a reasonable low-frequency noise transmission suppression, heavy structures are required, which leads to significant weight penalties. As a result, the search for alternative ways of the low-frequency noise transmission suppression has become a very important research area.

2.2.2 Active noise control

The active noise control/cancellation (ANC), in which secondary waves with the opposite phase interfere destructively with the disturbing noise, has drawn increasing interest as a potential method to overcome the limitations of passive sound insulation. ANC method is based on the use of either feedforward control or feedback control. In feedforward control, a coherent reference signal is picked up before it propagates to the secondary source (the control speaker or actuator). In feedback control, however, the controller attempts to attenuate the noise without the benefit of the previously described reference signal. The problem with feedforward control then is that a coherent reference signal is needed. If such a reference signal is not available, feedback control is then the alternative option. However, the control bandwidth achieved in feedback control is typically very narrow due to the nature of the speaker dynamics in the low 100—500 Hz range. The performance achieved is highly limited by the available gain and phase margins. Feedforward ANC is generally more effective than feedback ANC, especially when the feedforward system has a reference signal isolated from the secondary anti-noise source. Most ANC systems in use and under development use feedforward control.

For better awareness about the ANC, lets look at the brief history about the method. At 1930s, Leug [32] first suggested the idea of ANC. The mechanism is based on the destructive interference of the incident sound wave with the sound wave generated from a speaker. His patent proposes a feedforward system in which a microphone senses an acoustic pressure superposed i.e. of a sound wave incident to a loudspeaker. The sensed signal is processed and then introduced to the speaker, which should desirably generate a sound wave inverse to the incident one. Because of the fact that it was impossible to implement the method with the technology available at that time, the first experiments with the noise control were performed nearly twenty years later. Olson and May [33] and Olson [34] experimented with an "electronic sound absorber". His arrangement consisted of a microphone placed in a duct in close proximity to the loudspeaker face. The speaker and the microphone operated in a feedback loop, which means a driving of the speaker by the processed signal from the microphone in order to minimize the sound pressure at the microphone's location. Other important researchers in this stage include Widrow et al. [35], Jessel and Mangiante [36] and patent of Swinbanks [37]. With the development of digital signal processing techniques, ANC reached a new stage. Chaplin [38] introduced digital techniques in his ANC patent and then, he realized the first simple digital control systems in ducts [39]. Later in 1989, both the feedforward and the feedback approaches to the noise control were combined in the work of Eriksson [40], where the feedforward noise attenuation system was adapted on the base of the feedback signal from the additional error sensor. Since then, much work on ANC using digital processing techniques has been published.

A literature survey reveals very few academic publications directly related to window active sound transmission control. However, several patent applications can be found on this topic. The patent by Petiet [41] proposes generating sound waves or anti-sound waves using window glass or other types of transparent material. Vibration of window panes is realized by use of either an electrically conductive layer on the panes or by the use of piezo elements or by the use of a gas confined between the window panes. Tagg's invention [42] allows the window itself to be used as a conventional speaker. A speaker coil is attached directly to the window and causes it to vibrate. Mark [43] proposes a noise attenuation system located on a movable side glass of a motor vehicle for reducing the noise within the passenger compartment. ANC was also used to improve the sound insulation of double-glazed windows. Jakob and Möser obtained their results with a feedforward [44] and adaptive feedback controller [45]. They presented a comprehensive overview of the system with various numbers and positions of loudspeakers and microphones inside the cavity and they gave some insight into the physics of the active double-glazed window. The total sound pressure level can be reduced by nearly 8 dB and somewhat more than 5 dB with feedforward and feedback control, respectively, in the frequency range up to 400 Hz. A recent work by Zhu [46] shows the development of thin glass panels, whose vibrations can be controlled electronically by small rare earth voice coil actuators. The development of the control system is based on the use of a wave separation algorithm that separates the incident sound from the reflected sound. Using this method, the sound transmission reduction by $10 - 15$ dB in a broadband frequency range up to 600 Hz was achieved.

Although results on many successful ANC systems have been published, the major limitations of ANC systems must be noted. First, since the noise source and environment tend to be non-stationary, robustness and so powerful electronics requirements limit the performance of ANC systems. Although the continuously increasing speed of progress in digital electronics allows to satisfy high requirements for computational capacity, the large instrumentation raises the costs of extra power-supplies, amplifiers, filters, converters, and microprocessors. Generally, the improvement in the conventional ANC systems – higher efficiency, stability and operating flexibility – goes along with an increase in their complexity and high costs. Second, it is very difficult for an ANC system to achieve global noise cancellation in a 3-D environment such as in an enclosure. This is especially due to the limitations on the number of speakers and microphones that can be used. With the inputs from the primary source and the secondary sources, the acoustic field in an enclosure becomes very complicated. Optimal arrangement of the available control speakers and microphones becomes critical. Moreover, when applied to building windows, the ANC method requires external microphones for disturbance monitoring, and internal error sensors and loudspeakers for control purposes.

2.2.3 Active structural acoustic control

Later, the active structural acoustic control (ASAC) method has been developed for the reduction of the structure-borne noise. In this method, vibrating structures are used as secondary noise sources to suppress sound fields generated by primary noise sources from outside. ASAC in conjunction with the adaptive feedforward control has been proved to be an efficient practical approach to reduce structure-borne sound. ASAC works on the principles of reducing the vibration amplitude of the structure (modal reduction), as well as changing the vibration distributions of the structure so that the vibration distributions of each structural modes destructively interfere with one another in their associated radiating acoustic field (modal restructuring). Essentially, ASAC is a specific embodiment of ANC that could be used to reduce the sound radiated from a vibrating structure into an enclosure.

Usually, piezoelectric or other force actuators are used to change vibration modes of structures. Fuller et al. [47] were the first who demonstrated the possibility of active vibration control of the structures and the potential effectiveness of piezoelectric actuators. Fuller analyzed the use of one or two control point to minimize a cost function proportional to the radiated acoustic power through the aluminum elastic plate [48]. Fig. 2.7(a) shows the model setup and the computed sound transmission loss for the cases of one or two point force actuators located on the structure is shown in Fig 2.7(b). The results show that for low to mid-range frequencies, large

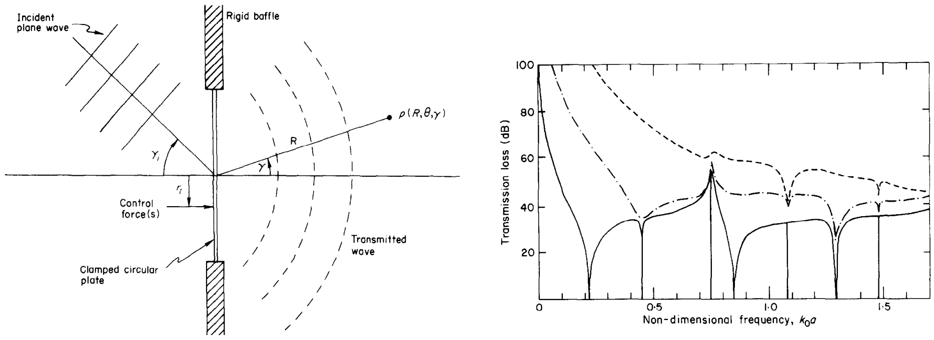

(a) (b)

Figure 2.7: (a) Scheme of analyzed sound transmission system by Fuller. Aluminum elastic plate is clamped in a rigid frame. Fuller derives the pressure radiated from the plate due to the incident plane acoustic wave (noise) and the point force excitation (control); (b) The plate transmission loss calculated by Fuller versus non-dimensional frequency. The results show that for low to mid-range frequencies, large global reductions in radiated sound levels can be achieved with just one (dash-and-dot line) or two judiciously located point force actuators (dashed line). The solid line stands for the sound transmission loss of the simple aluminum plate without control sensors; [48]

global reductions in radiated sound levels can be achieved with just one or two judiciously located point force actuators. Later, Metcalf and Fuller applied actively controlled harmonic force inputs to reduce experimentally the sound transmitted through an elastic circular plate [49]. The performance of the active system in reducing the transmitted sound was tested for several input frequencies up to 200 Hz and the reduction of about $15 - 25$ dB in a sound transmission was achieved. The experimental results are compared to previously derived analytical results in [48]. In their next work [50], piezoelectric or point force actuators have been further analytically investigated for the use as active control inputs attached to the rectangular plate. These results show that a reduction of sound transmission through the plate can be successfully achieved, if the proper size, number and position of the piezoelectric actuators are chosen. A very interesting result, which was observed, was that point force actuators were seen to perform slightly better than piezoelectric actuators (see Fig. 2.8).

Methods investigated by Fuller et al. are further used by Thomas [51]. This paper gives a fairly detailed study of the active control of harmonic sound transmission through rectangular plates by means of secondary force inputs. Berry et al. [52] presents a general formulation for sound radiation from panels with arbitrary boundary conditions. The boundary conditions

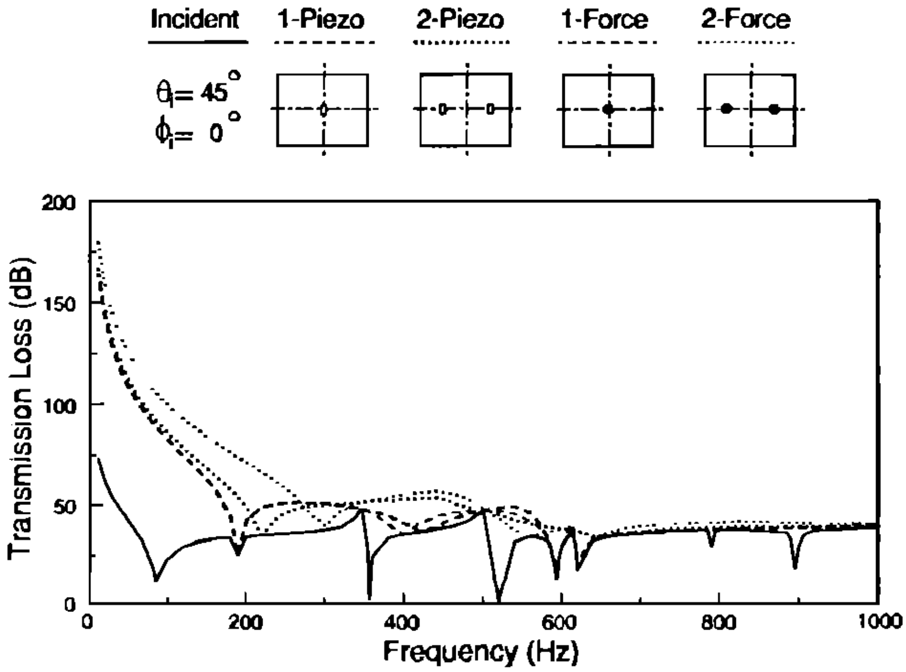

Figure 2.8: Sound transmission loss through the plate with attached piezoelectric or point force actuators computed by Fuller [48]. It can be seen that a reduction of sound transmission through the plate can be successfully achieved and, that point force actuators performed slightly better than piezoelectric actuators.

are represented by a translational and a rotational stiffness at the edge of the plate. In extreme cases, both of them are set to zero or infinity which means a freely mounted plate or a clamped edge condition, respectively. Pan et al. in [53] analytically and Pan and Hansen in [54] experimentally analyzed a technique for controlling noise transmitted into the interior of a cavity through a rectangular plate. Their method involves the use of point force actuators on the boundary structures. Results obtained here demonstrate that there are two different control mechanisms. If the system response is dominated by panel-controlled modes, sound energy in the cavity is minimized by suppressing the panel modes that radiate into the cavity. If the system response is dominated by cavity-controlled modes, the control force, caused by the actuators, is used to change the panel velocity distribution and thus adjust the radiation of each panel mode. Their experimental results qualitatively verify their previous analytical results. Balachandran et al. [55] analytically and experimentally studied the noise control in the interior of a three-dimensional enclosure with rigid acrylic walls and one flexible aluminum wall, clamped along all four edges. Noise generated by an external speaker is transmitted into the enclosure through the flexible boundary and active control is realized by PZT piezoelectric actuators bonded to the flexible boundary. Voltage inputs to the piezoelectric actuators are optimized. Later, Al-Bassyiouni and Balachandran [56] developed a structural–acoustics model for studying the transmission of sound through a flexible panel into an enclosure. The model is used to describe the pressure fields inside and outside the three-dimensional rectangular enclosure, as well as the flexible panel vibrations. A spherical wave, which is generated by a noise source located in the near field, is transmitted into a rectangular enclosure through a flexible panel with piezoelectric actuators, which are bonded symmetrically to the top and bottom surfaces of the panel.

Various studies of ASAC use the properties of passive double panel system to enhance the noise control performance. As an example it could be mentioned the work by Carneal and Fuller [57]. They analytically and experimentally investigated the radiating plate stiffness influence on the acoustic transmission loss and the placing of PZT actuators. Fig. 2.9(a) shows the model/experimental setup. A double panel system with a stiffer radiating plate exhibits a decreased coupling of the incident and radiating plates and a lower modal density, which results in increased controlled transmission loss (compare Fig. 2.9(b) of the acoustic transmission loss of the sandwich board radiating plate with the Fig. 2.9(c) of the acoustic transmission loss of the aluminum radiating plate). As for the PZT actuators placing, it is better to mount them on the radiating plate of a double panel system then on the incident plate (see both Fig. 2.9(b) and Fig. 2.9(c)). Another example of the active structural control of the noise transmission control through a mechanically linked double-wall structure into an acoustic enclosure is presented by Li and Cheng [58]. Two control strategies (for structural control it is used the thunder actuator, for cavity control it is used the loudspeaker) and two control mechanisms (modal suppression and modal rearrangement) are examined and numerical simulations are carried out. Modal suppression occurs mainly in the low-frequency range while modal rearrangement in the high-frequency one.

Concerning ASAC used for the purposes of the noise suppression through the glass windows, a recent work by Naticchia and Carbonari [59] was presented. They study the implementation of an active structural control system for glazed facades. They obtained a sound reduction of the highest value up to 15 dB in the low frequency range (up to 200 Hz). They have also proposed a procedure to combine this approach with the laminated glass plates, which are more effective at higher frequencies.

Most recent works in the field are focused mainly on the simulations. The paper by Pinte et al. [60] discusses the effectiveness of an ASAC system for the reduction of repetitive impact noise, radiated by structures with a high modal density. It was for the first time when non-periodic damping

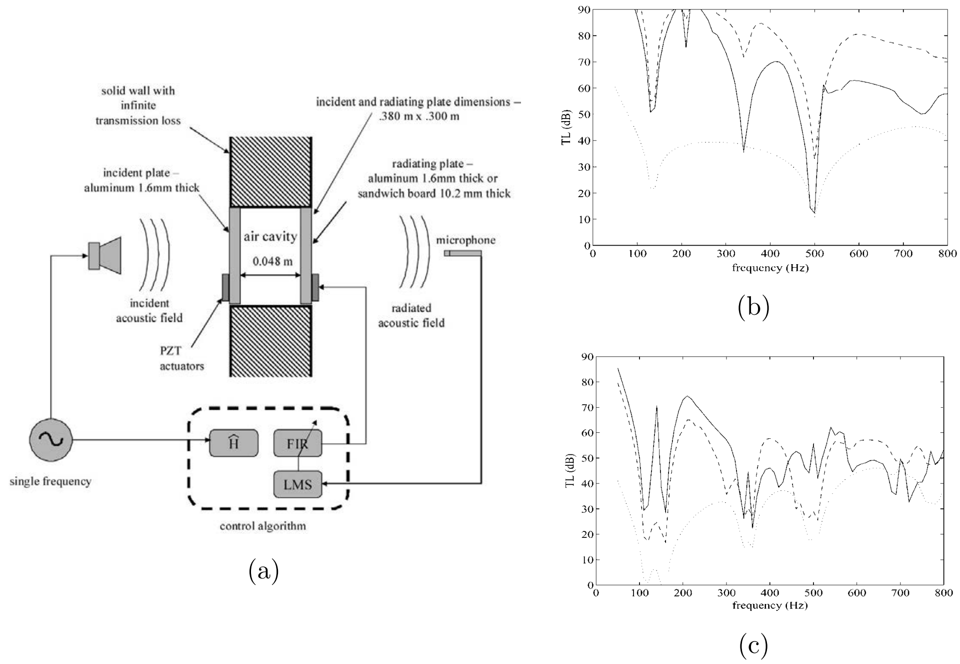

Figure 2.9: (a) Scheme of a model/experimental setup of a double panel system; (b) Sandwich board radiating plate: Uncontrolled (solid line) and controlled acoustic transmission loss for double panel system with PZT actuators located on incident (dashed line) and radiating plates (dotted line); (c) Aluminum radiating plate: Uncontrolled (solid line) and controlled acoustic transmission loss for double panel system with PZT actuators located on incident (dashed line) and radiating plates (dotted line); [57]

using ASAC was used. The developed ASAC strategy has been verified on a thick steel plate, which is excited by successive impacts. Kozupa's and Wiciak's [61] paper presents simulations of the aluminum plate with active vibration control realized using four piezoceramic PZT actuators and one PZT sensor bonded to the plate. The aim of this paper is to analyze and compare two ways of excitation of the test plate – mechanical and acoustic. The test results indicate that the use of PZT actuators can decrease vibrations by approximately 15 dB for a pure sound input with acoustic excitation method and by 18 dB for mechanical excitation method (a sinus vibration signal). Kapuria and Yasin [62] provided the extensive study of influence of placing piezoelectric fiber reinforced composite sensors and actuators, multiple segmentation of their electrodes and the piezoelectric fiber orientation on the active vibration suppression of multi-layered plates. Isabelle Bruant et al. [63] study the optimization of piezoelectric actuators and sensors locations for active vibration control of an elastic plate. Two optimization variables are considered for each piezoelectric device: the location of its center and its orientation. Genetic algorithms are used to find the optimal configurations. Yiqi and Yiming [64] applied the finite difference method to carry out the nonlinear active vibration control of the structure with adoption of the negative velocity feedback control algorithm. Tavakolpour et al. [65] used the finite difference method and self-learning feedback control for a flexible plate structure active vibrations control using a piezoelectric actuator. Hu and Galland [66] performs the active control of the double wall structure with symmetrically located piezoelectric patches and with porous material, using finite element simulations and experimental validation. The porous material represents the passive noise suppression. It is both theoretically and experimentally demonstrated that the acoustic transmission loss of more than 10 dB at the resonance frequencies can be increased with the active control in addition to a passive porous material influence. Yuan et al. [67] proposed active control laws for sound transmission through a stiffened panel in the low-frequency range using hybrid control strategy combining both feedback and feedforward control.

However, when applied to building windows, in order to develop model-based ASAC schemes, a good understanding of structural–acoustic interactions in the considered system is required. Both of the methods – ANC and ASAC – require a fast control algorithm and powerful electronics, so, in general, such requirements yield rather expensive and energy consuming systems which will be introduced in the next section.

2.2.4 Semi-active noise control

The third category of noise suppression methods is based on the semi-active control approach. An example to be mentioned here is the possibility of the arrangement of optimally tuned Helmholtz resonators (HRs) that result in an increase in the acoustical damping level inside the cavity between the double plates. The HR is one of the most common devices for passive control of noise at low frequencies. Mao and Pietrzko [68] developed a fully coupled system of structural-acoustic-HRs for the double wall structures by the modal coupling method. The simulations were confirmed by their experimental work [69]. With optimally tuned HRs it is possible to achieve the sound reduction up to 18 dB at certain low frequencies (to 100 Hz). Recent results concerning the active and passive control of sound transmission through double wall structures have been summarized in the review by Pietrzko and Mao [70].

Another example of the semi-active noise cancellation method with a rather high application potential is the piezoelectric shunt damping (PSD). This method uses piezoelectric elements connected to a shunt circuit. In fact, this system controls a strain of the element according to the applied force or vice versa, i.e. a one port circuit is connected to the piezoelectric element and the direct and inverse piezoelectric effects work simultaneously. The shunt circuit could be consisted of either passive or active elements. This categorization was introduced by Niederberger [71].

Passive shunts are characterized by the fact that they do not add any energy to a system. They are usually comprised of linear one port circuits which can be divided into the resistive, resonant or capacitive groups. Of course, there exist the group of nonlinear shunts which are characterized by the fact that they produce discontinuous or in other way nonlinear characteristics due to some circuits parts, e.g. diodes. This attitude is typically used in power harvesting applications (see e.g. [72] or [73]). The approach with passive shunt circuits has been widely studied by Fleming et. al (see e.g. [74, 75, 76]). It is mainly focused on narrow frequency band devices (based on passive resonant shunts) and relatively complicated control algorithms based on classical linear quadratic gaussian methods (LQG) implemented through digital signal processors. They use this attitude in the nanopositioning system applications. In their recent works they study piezoelectric shunt damping method with a force sensor added to the nanopositioning stage as a feedback variable to achieve both tracking and damping [77]. Also, using the LRC passive shunts, they control the image resolution of the atomic force microscope [78].

Vibration damping of planar structures or the suppression of the noise transmission through them is not very trivial problem, so, in past few years there are various tries to adopt some semi-active hybrid strategies. Usually, it is the combination of the conventional passive damping with some passive shunt circuit. A numerical model of one such device, exhibiting mass-spring-damper dynamics, attached to a vibrating host structure is described and validated in 3D FEM analysis by Harne and Fuller [80]. In their following study, smart foam samples (lightweight clamped panel with the poroelastic foam) containing a single half-circular segment of embedded piezoelectric film attached to the clamped plate are considered. As the load resistance on the electrodes is increased, the resonance frequency of the sample is shifted. The model was employed to evaluate the simultaneous vibration control and power-harvesting potential of similar devices on a clamped panel. Ducarne et al. [81] present a strategy to optimize (in terms of damping efficiency) the geometry of piezoelectric patches as well as their placement on the host elastic structure. This procedure is based on the maximization of the modal electro-mechanical coupling factor which is assumed to be the main free parameter that governs the shunt optimization. An interesting result of this paper is the importance of the thickness of the piezoelectric patches and the ratio of Young's moduli of the piezoelectric material and the elastic material of the host structure.

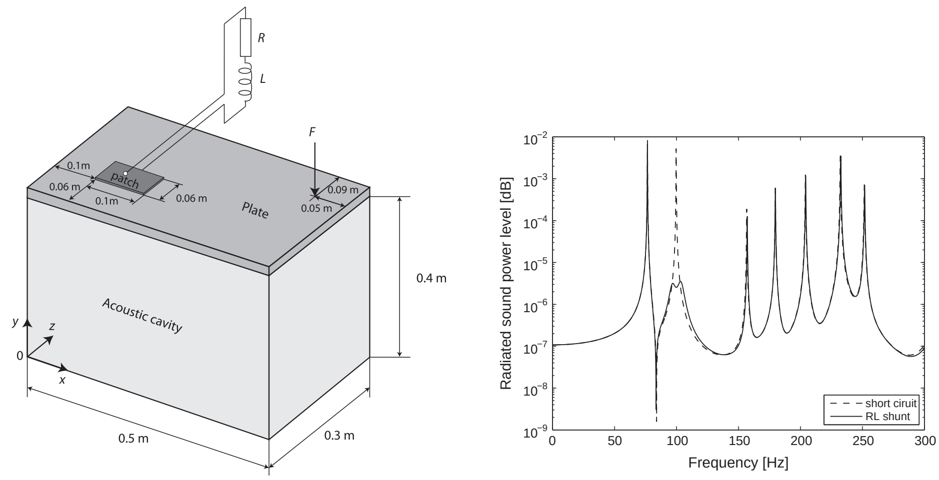

(a) (b)

Figure 2.10: (a) Scheme of an electromechanical-acoustic coupled system considered by Larbi – acoustic cavity with a plate with layered piezoelectric element shunted by the resonant circuit; (b) Radiated sound power in the cavity with (solid line) and without resonant shunt system (dash-and-dot line). It can be seen that the shunt circuit has an enormous influence on the radiated sound power at some tuned single frequency mode; [79]

Variational formulation and the FEM implementation of vibroacoustic response of the structures with piezoelectric shunt damping is developed by Larbi et al. [79]. Their system consists of a composite multilayer piezoelectric structure coupled with an acoustic fluid and connected to resonant shunt circuits. Fig. 2.10(a) shows one of the examples with an acoustic cavity with a plate with elastic properties similar to glass. The layered piezoelectric element is attached to the plate and shunted by the resonant circuit. It becomes apparent, see Fig. 2.10(b), that passive inductive shunt damping techniques has been shown very effective for vibration attenuation of low frequency modes in structural-acoustics. They note if one desires to broaden the effectiveness of these inductive shunt systems on a wider frequency band and to avoid a very precise tuning of the electrical parameters, further extension has to be turned to switching shunt damping. E.g., 6-PZT network multi-tone switching shunt control (SSC) system embedded into a balanced fiberglass laminate plate was used for the noise and vibration control of non-isotropic structures by Ciminello et al. [82]. They performed both FEM analysis and experiment with a good agreement and amplitude reductions up to 16 dB were attained.

On the other hand, active shunt circuits are the ones that add energy to the shunted system. There are employed other circuit elements such as operational amplifiers. Active shunts can fundamentally offer a higher efficiency of damping, however, stability is not automatically guaranteed and additional power to drive the shunt circuit is required [83]. Lissek et al. deals with the design of electric networks (active but also passive) when connected to the loudspeaker are employed as an absorber of the sound ("electroacoustic absorber") ([84], [85]). Also, active feedback control and shunt control are discussed and compared. The goal is to reach desired acoustic impedance over a certain frequency bandwidth. The array of 10 shunt loudspeakers is capable of damping the chosen mode with an acoustic attenuation of 14 dB. An extensive study about electroacoustic absorbers and the unifying theory of their active acoustic impedance control is then presented by Lissek et al. [86] and a method for acoustic performance optimization of the electroacoustic absorber is presented by Boulandet and Lissek [87]. A simple case study is provided to illustrate that the electroacoustic absorber performance depends on several constitutive parameters (moving mass of the loudspeaker, the enclosure volume or the electrical load value to which the loudspeaker is connected). Rather new work by Boulandet et al. mainly concerning the controlling mechanism using a digital real-time controller is discussed in [88].

Among the active shunts belong negative capacitors (NC). The method is based on the change of the vibrational response of the structure using piezoelectric actuators shunted by active electronic circuits that have a negative effective capacitance. This method is now known as active piezoelectric shunt damping (APSD). It was demonstrated by Date et al. [90] that by connecting the piezoelectric element to a NC circuit, it is possible to control the effective elastic stiffness of the piezoelectric element to a large extent (in theory to zero or infinity), in a broad frequency range. This method allows to realize noise shielding and vibration isolation systems. Early applications of this system have been reported by Okubo et al. [91] and Kodama et al. [92]. The theoretical analysis of these systems was performed later by Mokrý [93, 94] and various applications of an active elasticity control technique in the noise and vibration control devices were demonstrated by Fukada et al. [95, 96]. Imoto et al. [97] and Tahara [98] demonstrated the great potential of this method on a system for suppressing vibrations by 20 dB in the broad frequency range from 1 to 100 kHz. The low energy consumption was proved by Vaclavik and Mokry [99]. The noise shielding principle using the NC circuit was further theoretically analyzed by Sluka et al. [89]. His model considers the sound propagation through the curved piezoelectric membrane shunted by the NC circuit (see Fig. 2.11(a)). The acoustic transmission loss is controlled by the ratio of specific acoustic impedances of air and the membrane. Since the specific acoustic impedance of the curved membrane fixed in a rigid frame is proportional to its elastic stiffness, an extremely stiff membrane (compared to air) works as an interface with high sound transmission loss.

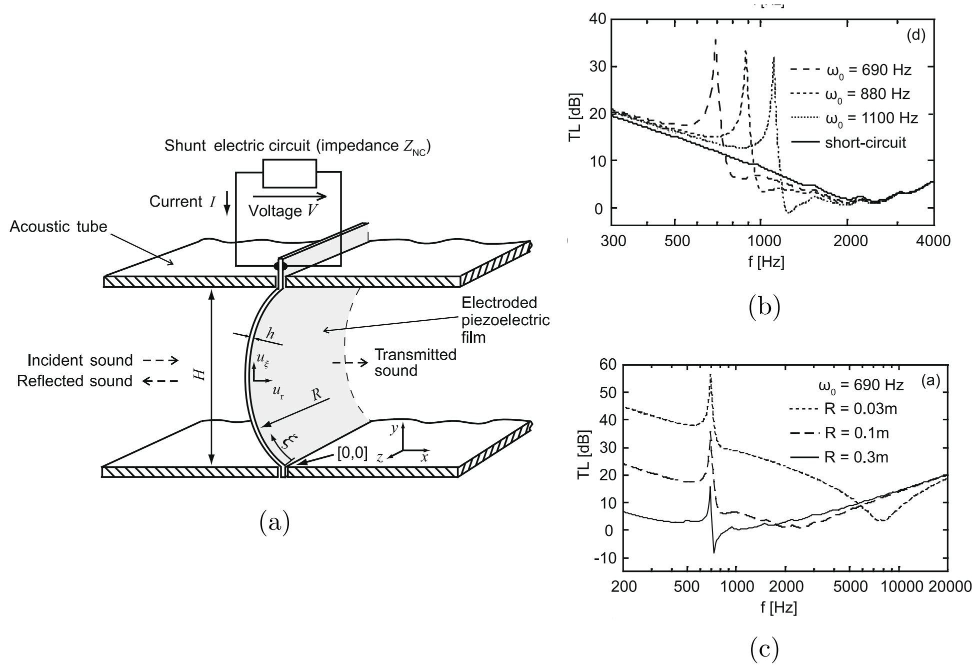

Figure 2.11: (a) Geometry of the curved piezoelectric membrane model for the calculation of the acoustic transmission loss of sound; The frequency dependence of the acoustic transmission loss (TL) of sound through the cylindrically curved piezoelectric membrane connected to the shunt electric circuit with negative capacitance. Effects of following parameters are shown: (b) membrane radius R, (c) the frequency ω_0 where the transmission loss reaches maximum; [89]

In this arrangement, the majority of acoustic energy is reflected from the membrane and only a negligible amount of energy is transmitted. The improved acoustic transmission loss can be seen in Fig. 2.11(b), where the effect of a membrane radius is shown, and in Fig. 2.11(c), where the acoustic transmission loss reaches maximum at the specific frequency according the tunning of the NC circuit.

The change of the stiffness and even the geometry of the whole structure to reach the improvement in noise transmission through the structures became more investigated recently. Typically, the structure could be stiffened by some mechanical forces which can be a result of an electrical voltage induced on a stiffening element. Cao et al. theoretically study the interaction of two sets of parallel stiffeners with the laminated plate through the normal forces [100] and the interaction of the point forces with a shear deformable laminated cylindrical shells [101]. Stiffeners have significant influence on the sound field transmitted through the plate or the shell. Xin and Lu [102] developed an analytic model to investigate the wave propagation and sound transmission characteristics of an infinite sandwich structure reinforced by two sets of orthogonal rib-stiffeners. There is considered an influence of the spacing size between the rib-stiffeners on the sound transmission loss. Chronopoulos et al. [103] developed a robust-unified model for the prediction of the vibroacoustic performance of composite shells of various geometries (namely curved panels and cylindrical shells) within a statistical energy analysis approach. The method was adopted for calculation of the sound transmission loss where the finite dimensions of the panel were taken into account. For non-closed shells, a generally very good agreement between the experimental measurements and the prediction using the presented method was observed. Sarangi and Ray [104] provide an analysis of active damping of viscoelastic doubly curved shell. This layer is constrained between the host structure and a constraining layer made either 1-3 PZT composite or of PZT fibers reinforced composite material (particularly active fiber composites (AFC)). When the constraining layer is activated by an appropriate control voltage, the shear deformations of the viscoelastic layer improve damping characteristics of the overall structure. It is also found that the performance of constraining layer being made of the AFC is significantly higher than the one with 1-3 PZT constraining layer.

The Thesis is focused on the APSD method that can offer an attractive approach for reduction of the noise level transmitted through windows in buildings. The objective of the all work is to analyze the most efficient ways for suppression of noise transmission through the glass plates using active elasticity control (AEC) introduced by Date et al. [90] of attached piezoelectric elements and the change of the geometry of the glass plate. The AEC method will be explained in detail in Chap. 3. But first, the most important features of the noise transmission through the glass plates must be analyzed using the approximative analytical model and the key aspects which have an influence on the acoustic TL have to be determined. To verify the applicability of the APSD method to the noise transmission suppression through the glass plates, FEM simulations of sound transmission through a glass plate with attached piezoelectric elements shunted with negative capacitance circuits are performed (Chap. 5). Also, simple experimental setup for the approximative measurements of the acoustic TL is described in this chapter. The chapter before, Chap. 4, presents details of the FEM simulations of the anisotropic effective Young's modulus of the piezoelectric macro fiber composite (MFC) actuator and the influence of NC circuit on the elastic properties of the actuator.

Chapter 3

Theoretical modelling of the acoustic impedance of a curved glass shell and the principles of active elasticity control method

In this Chapter, the possibilities in the active control of acoustic transmission loss (TL) of planar structures using the active elasticity control (AEC) method are analyzed. In the first step of the analysis, the most important parameters of the noise transmission system, which have an influence on the acoustic TL, are determined. In our particular case, an approximative analytical model of the vibration of curved glass shell is developed (see Sec. 3.1). Then, the specific acoustic impedance of the curved glass shell is calculated within the developed model. In the second step of the analysis, it is demonstrated that it is possible to control the elastic properties of the planar structure using an active piezoelectric layer attached to the planar structure (see Sec. 3.2). Finally, the basic theoretical aspects of the AEC method are explained (see Sec. 3.3).

3.1 Analytical estimation of the acoustic impedance of a curved glass shell

In order to determine the parameters of the glass plate that control its acoustic impedance, it is necessary to analyze its vibrational response. So, the analytical model of the vibration of generally curved glass shells is developed in this Section.

For simplicity, consider a rectangular-like glass shell of a constant thickness h and with the dimensions denoted by symbols a and b, which is shown in Fig. 3.1. Consider a curvilinear orthogonal coordinates x and y, that define the position on the curved surface of the shell. Consider that the shell has constant radii of curvature along the x and y coordinates denoted by symbols R_x and R_y, respectively. It is convenient to introduce the symbols $\xi_x = 1/R_x$ and $\xi_y = 1/R_y$ for local curvatures of the shell along the x and y directions, respectively. Symbols u_x and u_y stand for tangential components of the displacement of the infinitesimal shell element with the volume $h\,dx\,dy$. The symbol w stands for the normal component of the displacement of the shell element. Using the fundamental equations presented in basic textbooks [105, 106, 107], equations of motion are derived, as usual, from the equilibrium of forces acting on an infinitesimal element of the curved glass shell:

$$
\begin{aligned}
\frac{\partial T_x}{\partial x} + \frac{\partial T_{xy}}{\partial y} &= \varrho h \frac{\partial^2 u_x}{\partial t^2}, &(3.1)\\
\frac{\partial T_{xy}}{\partial x} + \frac{\partial T_y}{\partial y} &= \varrho h \frac{\partial^2 u_y}{\partial t^2}, &(3.2)\\
\frac{\partial N_x}{\partial x} + \frac{\partial N_y}{\partial y} + \frac{T_x}{R_x} + \frac{T_y}{R_y} + q &= \varrho h \frac{\partial^2 u_z}{\partial t^2}, &(3.3)
\end{aligned}
$$

where the symbol ϱ is the mass density of the material of the shell, T_x, T_y and T_{xy} are the forces per unit area of the shell cross section, which acts in the tangential plane to the curved glass shell. Forces T_x, T_y acts along the directions of x and y axes, respectively. Force T_{xy} is the shearing force in the xy-plane. Symbols N_x and N_y stand for the bending forces normal to the tangent plane of the curved shell and bending the shell along the x and y directions, respectively. The above equations of motion must be appended by the equations for the equilibrium of bending moments M_x and M_y, the twisting moment M_{xy}, and the bending forces N_x and N_y acting on an infinitesimal element of the curved glass shell:

$$
\begin{aligned}
N_x &= \frac{\partial M_x}{\partial x} + \frac{\partial M_{xy}}{\partial y}, &(3.4)\\
N_y &= \frac{\partial M_y}{\partial y} + \frac{\partial M_{xy}}{\partial y}. &(3.5)
\end{aligned}
$$

In the next step, the equations for the local elasticity are considered in the following form:

$$
\begin{aligned}
T_x &= \frac{Yh}{1-\nu^2}\left(e_x + \nu e_y\right), && (3.6)\\
T_y &= \frac{Yh}{1-\nu^2}\left(e_y + \nu e_x\right), && (3.7)\\
T_{xy} &= \frac{Yh}{1+\nu} e_{xy}, && (3.8)\\
T_{yx} &= \frac{Yh}{1+\nu} e_{xy}, && (3.9)\\
M_x &= -12\,G\,\left(\zeta_x + \nu\zeta_y\right), && (3.10)\\
M_y &= -12\,G\,\left(\zeta_y + \nu\zeta_x\right), && (3.11)\\
M_{xy} &= 12\,G\,\left(1-\nu\right)\,\zeta_{xy}, && (3.12)\\
M_{yx} &= -12\,G\,\left(1-\nu\right)\zeta_{xy}, && (3.13)
\end{aligned}
$$

where the symbols Y, ν and G stand for the Young's modulus, Poisson's ratio and the bending stiffness coefficient of the shell, respectively. Symbols e_x, e_y and e_{xy} are the mechanical strain tensor components along the coordinates x, y, xy, respectively and ζ_x, ζ_y and ζ_{xy} are the curvature changes, respectively.

Finally, equations for strain and curvature changes are considered in the following form:

$$
\begin{aligned}
e_x &= \frac{\partial u_x}{\partial x} - \frac{u_z}{R_x}, && (3.14)\\
e_y &= \frac{\partial u_y}{\partial y} - \frac{u_z}{R_y}, && (3.15)\\
e_{xy} &= \frac{1}{2}\left(\frac{\partial u_x}{\partial y} + \frac{\partial u_y}{\partial x}\right), && (3.16)\\
\zeta_x &= \frac{\partial^2 u_z}{\partial x^2}, && (3.17)\\
\zeta_y &= \frac{\partial^2 u_z}{\partial y^2}, && (3.18)\\
\zeta_{xy} &= \frac{\partial^2 u_z}{\partial x \partial y}. && (3.19)
\end{aligned}
$$

By combining Eqs. (3.1)-(3.19) one arrives at the equations of motion

$$\begin{aligned}
Yh\Bigg[\frac{1}{2(1-\nu^2)}\frac{\partial^2 u_x}{\partial x^2} + \frac{1}{2(1+\nu)}\frac{\partial^2 u_x}{\partial y^2} - \\
-\frac{1}{2(1-\nu)}\frac{\partial^2 u_y}{\partial x \partial y} - \frac{\xi_x + \nu\xi_y}{2\,(1-\nu^2)}\frac{\partial w}{\partial x}\Bigg] &= \varrho h \frac{\partial^2 u_x}{\partial t^2}, && (3.20a)\\
Yh\Bigg[\frac{1}{2(1+\nu)}\frac{\partial^2 u_y}{\partial x^2} + \frac{1}{2(1-\nu^2)}\frac{\partial^2 u_y}{\partial y^2} - \\
-\frac{1}{2(1-\nu)}\frac{\partial^2 u_x}{\partial x \partial y} - \frac{\nu\xi_x + \xi_y}{2\,(1-\nu^2)}\frac{\partial w}{\partial y}\Bigg] &= \varrho h \frac{\partial^2 u_y}{\partial t^2}, && (3.20b)\\
-G\Delta^2 w + \frac{Yh}{1-\nu^2}\Bigg[(\xi_x + \nu\xi_y)\frac{\partial u_x}{\partial x} + (\nu\xi_x + \xi_y)\frac{\partial u_y}{\partial y} - \\
-(\xi_x^2 + \xi_y^2 + 2\nu\xi_x\xi_y)w\Bigg] + \Delta p &= \varrho h \frac{\partial^2 w}{\partial t^2}, && (3.20c)
\end{aligned}$$

where

$$\Delta^2 w = \frac{\partial^4 w}{\partial x^4} + 2\frac{\partial^4 w}{\partial x^2 \partial y^2} + \frac{\partial^4 w}{\partial y^4} \qquad (3.21)$$

is the biharmonic operator. The symbol Δp stands for the difference of the acoustic pressures at the opposite sides of the curved shell and represents the “driving force” of the system. It is seen that the first and second equations in Eqs. (3.20) represent the equations of motion for the tangential components u_x and u_y of the shell displacement. These are coupled with the normal component of the shell displacement w and the driving force Δp via the nonzero values of curvatures ξ_x and ξ_y. It can be shown that for relatively small numerical values of curvatures considered in this work, the values of all terms, which contain the tangential components u_x and u_y in Eq. (3.20c), are much smaller than the remaining terms with the normal component w of the displacement. Under this consideration, the system of Eqs. (3.20) can be further reduced down to a single partial differential equation in a form:

$$-G\Delta^2 w + \frac{Yh}{1-\nu^2}\left(\xi_x^2 + \xi_y^2 + 2\nu\xi_x\xi_y\right) w + \Delta p = \varrho h \frac{\partial^2 w}{\partial t^2}. \qquad (3.22)$$

When one considers a simple situation: (i) the shell is formed by a rectangular part of a spherical shell, i.e. $\xi_x = \xi_y = \xi$, (ii) the steady state, when the shell is driven by the pure tone of angular frequency ω, i.e. $\Delta p(t) = Pe^{i\omega t}$ and $w(x,\ y,\ t) = w(x,\ y)e^{i\omega t}$, and (iii) the boundary conditions of the simple supported shell, i.e. $w(0,\ y) = w(a,\ y) = w_{xx}(0,\ y) = w_{xx}(a,\ y) = 0$ and $w(x,\ 0) = w(x,\ b) = w_{yy}(x,\ 0) = w_{yy}(x,\ b) = 0$, the solution of the partial differential equation Eq. (3.22) can be easily found

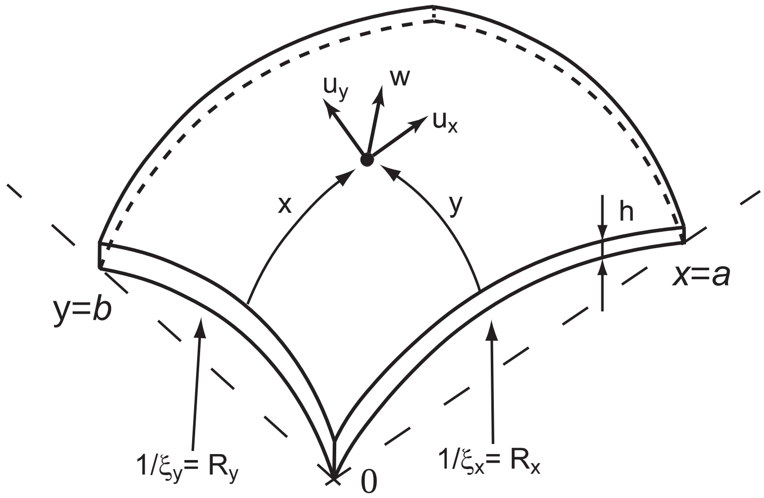

Figure 3.1: Geometry of the rectangular-like curved glass shell of constant thickness h. Symbols x and y stand for curvilinear orthogonal coordinates. The shell dimensions are denoted by symbols a and b. The shell has constant radii of curvatures along the x and y coordinates denoted by symbols $R_x = 1/\xi_x$ and $R_y = 1/\xi_y$. Symbols u_x and u_y stand for tangential components of the displacement of the infinitesimal shell element. The symbol w stands for the normal component of the displacement of the shell element.

in the form of Fourier series:

$$w(x,y,t) = \sum_{n,m=1}^{\infty} \frac{16P(1-\nu)\sin\left[(2n-1)\pi x/a\right]}{(2n-1)(2m-1)\pi^2\{2Yh\xi^2 + (1-\nu)} \times \\ \times \frac{\sin\left[(2m-1)\pi y/b\right] e^{i\omega t}}{\left[G((2m-1)^2/b^2 + (2n-1)^2/a^2) - \rho h\omega^2\right]\}}. \qquad (3.23)$$

Now, according to the Eq. (2.16), the effective value of the specific acoustic impedance z_w of the glass shell can be expressed in the following form:

$$Z_w(\omega) \approx \Delta p(0) \left[i\omega \sqrt{\frac{1}{ab}\int_a^0 dx \int_b^0 w(x,y,0)^2 dy} \right]^{-1}. \qquad (3.24)$$

When we substitute the expression for the normal displacement of the spherical shell w from Eq. (3.23), one can arrive at the following formula for the effective specific acoustic impedance:

$$Z_w(\omega) \approx$$
$$\approx \left\{ \sum_{n,m=1}^{\infty} \left[\frac{8i\omega a^2 b^2 (1-\nu)}{(2m-1)(2n-1)\pi^2 \left(G\,\zeta_{mn} + 2Yh\xi^2 - (1-\nu)\rho h\omega^2\right)} \right]^2 \right\}^{-1/2}, \tag{3.25}$$

where

$$\zeta_{mn} \;=\; \pi^4 \,(1-\nu)^2\,(1+\nu)\,\left[(2m-1)^2/b^2 + (2n-1)^2/a^2\right]^2.$$

It is clear that Eq. (3.23) describes the displacement of the rectangular part of a spherical shell in a special situation without much practical interest. On the other hand, the presented analytical solution serves a possibility to trace the key features of the system that can be used for the suppression of the noise transmission.

First, it is seen that with an increase of the glass shell curvature ξ, the term $2Yh\xi^2$ in the denominator of Eq. (3.23) increases. This yields the decrease of the amplitude of the shell displacement and, therefore, the decrease of the normal velocity of vibrations. As a result, the value of the specific acoustic impedance of the glass shell Z_w increases with an increase in its curvature ξ as it can be seen in Eq. 3.25. The reason for this curvature effect is that the normal displacement of the curved shell is controlled by the in-plane stiffness, in addition to the bending flexural rigidity. Second, the specific acoustic impedance Z_w of the curved shell, i.e. $\xi > 0$, increases with an increase in the Young's modulus Y. Third, the value of Z_w of the plane plate, i.e. $\xi = 0$, increases with an increase in the bending stiffness coefficient G.

Now, it is clear, that the active control of the Young's modulus Y and the bending stiffness coefficient G would influence the vibrational response of the glass shell. Next section of the Thesis explains the basic principle how to do that by means of the attached piezoelectric layer to the planar structure.

3.2 Composite structure of the glass plate and piezoelectric element

Generally, bending piezoelectric devices consists of several piezoelectric and non-piezoelectric layers laminated together. Each layer has different material and geometric parameters. The motion of multilayer composite structures is described by equations of motion, see e.g. the Eqs. 3.20, where the material and geometric parameters are replaced by their average values.

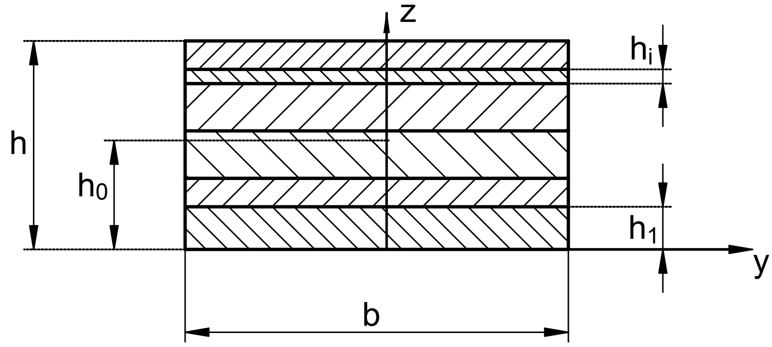

Figure 3.2: General multilayer structure with a rectangular cross-section placed in the system of coordinates. The structure has N layers of width b with different height h_i. The total thickness of the structure is denoted by the symbol h.

These average values can be calculated by the integration of the partial parameters of the sublayers over the total cross-section [108].

Imagine a general multilayer structure with a rectangular cross-section area $S = bh$ according to Fig. 3.2. The structure has N layers of width b with different height h_i, cross-section area $S_i = bh_i$, density ρ_i and Young's modulus Y_i. The total thickness of the structure is denoted by the symbol h. The position of the neutral axis, which passes through the centroid of the cross-section, is denoted by h_0. Then, the average density ρ_{Eff}, average Young's modulus Y_{Eff} and the position of the neutral axis h_0 can be solved using following relations:

$$\rho_{\text{Eff}} = \frac{1}{S}\int_S \rho dS = \frac{\sum_{i=1}^{N} \rho_i h_i}{h} \tag{3.26}$$

$$Y_{\text{Eff}} = \frac{1}{S}\int_S Y dS = \frac{\sum_{i=1}^{N} Y_i h_i}{h} \tag{3.27}$$

$$h_0 = \frac{1}{Y_{\text{Eff}} S}\int_S Y z dS = \frac{1}{2}\frac{Y_1 h_1^2 + \sum_{j=2}^{N} Y_j \left[\left(\sum_{k=1}^{j} h_k\right)^2 - \left(\sum_{k=1}^{j-1} h_k\right)^2\right]}{\sum_{i=1}^{N} Y_i h_i}. \tag{3.28}$$

The average bending stiffness G_{Eff} is calculated with respect to the position

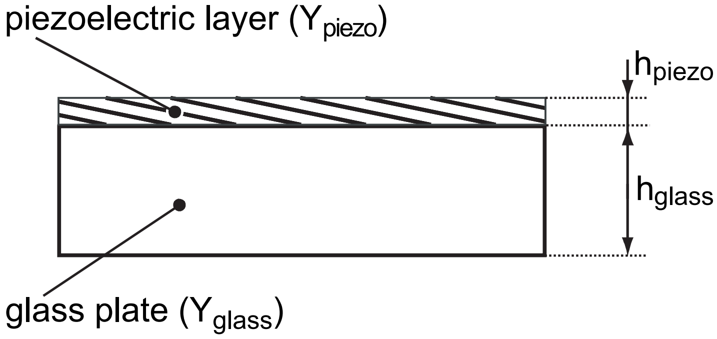

Figure 3.3: Cross-section of the layered composite structure, which consists of a glass plate of thickness h and Young's modulus $Y_{\rm glass}$ and an attached piezoelectric layer of thickness $h_{\rm piezo}$ and Young's modulus $Y_{\rm piezo}$.

of the neutral axis as

$$G_{\rm Eff} = \int_S Y z^2 dS = b\int_{-h_0}^{h-h_0} Y z^2 dS = \frac{1}{3} b \Bigg\{ Y_1\left[(h_1-h_0)^3-(-h_0)^3\right] + + \sum_{j=2}^{N} Y_j \left[\left(\sum_{k=1}^{j} h_k - h_0\right)^3 - \left(\sum_{k=1}^{j-1} h_k - h_0\right)^3\right]\Bigg\}. \tag{3.29}$$

Following the [108], let us consider a one of the typical layered configurations, simple bender with just two layers of different material and thicknesses, i.e. composite structure of the glass plate and the attached piezoelectric layer, with a cross-section shown in Fig. 3.3. The average (effective) Young's modulus of the whole structure $Y_{\rm Eff}$ is given by weighted average of the Young's moduli of the glass and the piezoelectric layer, according to the formula originated from Eq. (3.27):

$$Y_{\rm Eff} = \frac{Y_{\rm glass} h_{\rm glass} + Y_{\rm piezo} h_{\rm piezo}}{h_{\rm glass} + h_{\rm piezo}}, \tag{3.30}$$

where the symbols $Y_{\rm glass}$ and $Y_{\rm piezo}$ stand for the Young's moduli of the glass and the piezoelectric material of the piezoelectric layer, respectively. The symbols $h_{\rm glass}$ and $h_{\rm piezo}$ stand for the thickness of the glass plate and the piezoelectric layer, respectively. Let us substitute the symbols Y and h for the symbols $Y_{\rm glass}$ and $h_{\rm glass}$, for simplicity. Now, the average (effective) value of the bending stiffness coefficient $G_{\rm Eff}$ of the composite sandwich structure is given by the formula which originates from Eqs. (3.28) and

(3.29):

$$G_{\mathrm{Eff}} = \frac{Y^2 h^4 + Y_{\mathrm{piezo}}^2 h_{\mathrm{piezo}}^4 + 2YY_{\mathrm{piezo}} h h_{\mathrm{piezo}} \left(2h^2 + 3hh_{\mathrm{piezo}} + 2h_{\mathrm{piezo}}^2\right)}{12\left(1-\nu^2\right)\left(Yh + Y_{\mathrm{piezo}} h_{\mathrm{piezo}}\right)}, \tag{3.31}$$

where ν is Poisson's ratio of the material.

It is clearly seen that if Young's modulus of the piezoelectric layer is increased, both effective values of the Young's modulus Y_{Eff} and the bending stiffness coefficient G_{Eff} of the composite sandwich structure are increased as well. And, it is seen from Eqs. (3.23) and (3.25) that with an increase of the effective Young's modulus of the piezoelectric layer, the specific acoustic impedance of the curved glass shell increases. It should be pointed out that Eqs. (3.23) and (3.25) were calculated in a simplified model, where the values of curvature ξ. This simplification is not the case of many applications of practical interest but, on the other hand, this model serves only for the determination of the key aspects which control the specific acoustic impedance of the curved or plain planar structure. Now, it was demonstrated that by the piezoelectric layer attached to the planar structure it is possible to control the elastic properties of the whole system, so, the next section presents a principle and an implementation of a method for the active control of the Young's modulus of the piezoelectric material which can me attached as a control layer to the planar structure.

3.3 Active elasticity control of piezoelectric materials

Since the beginnings of the study of piezoelectric materials, it is known that the electrical boundary conditions of piezoelectric actuators greatly affect their effective elastic properties. The role of electromechanical interaction on the effective elastic properties can be amplified if an active shunt circuit is connected to the piezoelectric actuator. Such an approach was introduced by Date et al. [90] and is called the active elasticity control (AEC) method. When the method is adopted in vibration or noise transmission control applications, then thanks to the fact that the shunt circuit is by nature active, it belongs to the group of active piezoelectric shunt damping (APSD) methods.

The basic idea of the method is based on the superposition of direct and converse piezoelectric effects with Hooke's law. Let us explain the basic principle on the case when the piezoelectric element is exposed to the influence of incoming acoustic pressure as it could be seen in Fig. 3.5(a). That means, the external mechanical force is applied to the piezoelectric element. According to the Hooke's law the mechanical strain $\mathbf{S}$ is produced in the piezoelectric actuator and, the external force generates a charge Q on the electrodes due to the direct piezoelectric effect (see Fig. 3.5(b)). The generated charge is introduced to the electronic shunt circuit, which controls the electric voltage V on the electrodes of the piezoelectric element which is then deformed according to the inverse piezoelectric effect (see Fig. 3.5(c)). The total strain $\mathbf{S}$ of the piezoelectric actuator is then equal to the sum of both: the stress-induced strain (due to Hooke's law) and the voltage-induced strain (due to the converse piezoelectric effect). When the voltage-induced strain cancels the stress-induced strain, the total strain of the piezoelectric actuator equals zero even if nonzero external stress is applied. This actually means that the effective Young's modulus of the piezoelectric actuator reaches infinity. This fact could be successfully used in the noise transmission control applications because when the acoustic wave strikes the element with infinite Young's modulus, the all acoustic energy is reflected from the surface and nothing is transmitted to the other side (Fig. 3.5(d)).

The shunt circuit, which implements the control of effective elastic properties of the piezoelectric actuator is the active negative capacitance (NC) shunt circuit. The key parameter, which controls the value of the effective Young's modulus of the MFC actuator, is the capacitance of the circuit C. This fact can be derived, when the equations of state for the mechanical strain S_{ij} and the electric displacement D_i in the piezoelectric actuator, i.e. Eqs. (2.1d) are appended by the formula for the voltage $V = E_i h$ applied back to the electrodes of the piezoelectric element from the external capacitor of capacitance C:

$$V = -Q/C, \tag{3.32}$$

where $Q = D_i A$ is the charge generated on the electrodes of the piezoelectric actuator of electrodes area A.

Combining Eqs. (2.1d) and (3.32), it is possible to obtain the formula for the effective Young's modulus of the piezoelectric actuator shunted by the external capacitor [90]:

$$Y_{ijkl,\mathrm{shunted}} = \frac{T_{kl}}{S_{ij}} = \frac{1}{s^E_{ijkl}} \left(1 + \frac{k^2_{ijk}}{1 - k^2_{ijk} + \alpha} \right), \tag{3.33}$$

where k_{ijk} is the electromechanical coupling factor of the piezoelectric actuator ($0 < k_{ijk} < 1$), as introduced in Chap. 2, Sec. 2.1.1, paragraph 2.1.1.2, and $\alpha = C/C_S$ is the ratio of the shunt circuit capacitance C over the piezoelectric element static capacitance C_S at a constant mechanical stress T_{ij}, where $C_S = \epsilon^T_{ij} A/h_{piezo}$.

It can be seen from Eq. (3.33) that large values of the effective Young's modulus of the piezoelectric element can be achieved only when the capac-

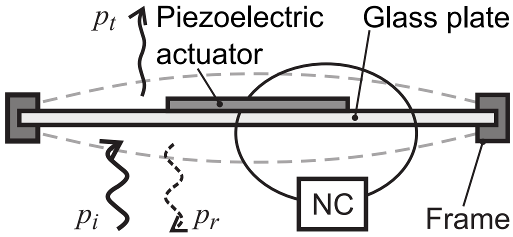

Figure 3.4: Scheme of the noise transmission suppression principle (cf. Fig. 2.5). The acoustic impedance of the plate is controlled using a piezoelectric actuator shunted by an active circuit. Vibration amplitude W normal to the glass surface is reduced by the action of the shunted piezoelectric actuator. In this way of damping, the greater part of the amplitude of the incident acoustic pressure wave is reflected from the plate than transmitted through the plate to the other side.

itance of the external circuit C is negative. It follows from the Eq. (3.33) that, when

$$C = -(1 - k_{ijk}^2)C_S, \tag{3.34}$$

the effective Young's modulus reaches infinity. Already mentioned in Chap. 2, Sec. 2.2, paragraph 2.2.4 that such a situation has been profitably used in several noise suppression devices [91, 92, 93, 109, 89]. On the other hand, when $C = -C_S$, the effective Young's modulus reaches zero. This could be used in various devices for the suppression of transmissibility of vibration (see e.g. [110, 111, 112, 113]). Based on the theory introduced here and the already performed experiments by Okubo et al. and Kodama et al. and calculations by Mokry et al. and Sluka et al, the principle of AEC method could be profitably used when one needs to suppress the noise through the planar structure, e.g. the glass plate. Fig. 3.4 shows the scheme of the noise transmission suppression principle using a piezoelectric actuator shunted by an active circuit with negative capacitance. Following the Eqs. (3.23), (3.25), (3.30), (3.31) and (3.33), vibration amplitude W normal to the glass surface is reduced and subsequently the specific acoustic impedance is increased by the action of the shunted piezoelectric actuator. So, the greater part of the amplitude of the incident acoustic pressure wave is reflected from the plate than transmitted through the plate to the other side without the glass being thicker (cf. Fig. 2.5).

3.4 Summary

This Chapter determines the parameters of the glass plate that control its acoustic impedance and introduces some ideas how to increase this physical property. The key messages of this Chapter could be summarized into several points:

- With an increase of the glass shell curvature ξ, the term $2Yh\xi^2$ in the denominator of Eqs. (3.23) and (3.25) increases. This yields the decrease of the amplitude of the shell displacement and, therefore, the decrease of the normal velocity of vibrations. As a result, the value of the specific acoustic impedance of the glass shell Z_w increases.

- The specific acoustic impedance Z_w of the curved shell, i.e. $\xi > 0$, increases with an increase in the Young's modulus Y and the bending stiffness coefficient G of the shell.

- The value of Z_w of the plane plate, i.e. $\xi = 0$, increases with an increase in the bending stiffness coefficient G of the plate.

- It is possible to control the average elastic properties of the curved glass shell using the piezoelectric layer attached to the shell. In addition, the control of the average Young's modulus and the bending stiffness coefficient of the layered composite structure of the glass shell and piezoelectric actuator can be achieved only using the control of the Young's modulus of the piezoelectric layer (see the Eqs. (3.30) and (3.31)).

- The AEC method offers a technique for the suppression of noise transmission through the piezoelectric composite structures or a technique for active suppression of vibrations of mechanical structures by attaching the piezoelectric elements to them. The effective Young's modulus of the piezoelectric element shunted by the NC circuit follows the theoretical Eq. (3.33). One can notice that, when the capacitance C is negative, the value of the effective Young's modulus of the piezoelectric actuator can be changed to a large extent. Fig. 3.4 shows the piezoelectric actuator attached to the surface of a glass plate. Then, the average value of the Young's modulus Y and the bending stiffness coefficient G of the glass composite plate is controlled to a large extent by the action of shunted NC circuit. Finally, the vibration amplitude W of the plate is reduced due to an increase in the bending stiffness coefficient G of the plate (in the case of the plane plate) and due to an increase in the bending stiffness coefficient G and the Young's modulus Y of the plate (in the case of the curved plate). In such a way of active "stiffening", a greater part of the amplitude of acoustic pressure wave is reflected than transmitted to the other side.

In the next Chapter, there will be introduced a piezoelectric actuator suitable for applications, which involves the potential problems of fragile vibrating structures such as glass plates. Using the finite element method simulations, it will be shown the effect of NC circuit on the average elastic properties of this piezoelectric actuator.

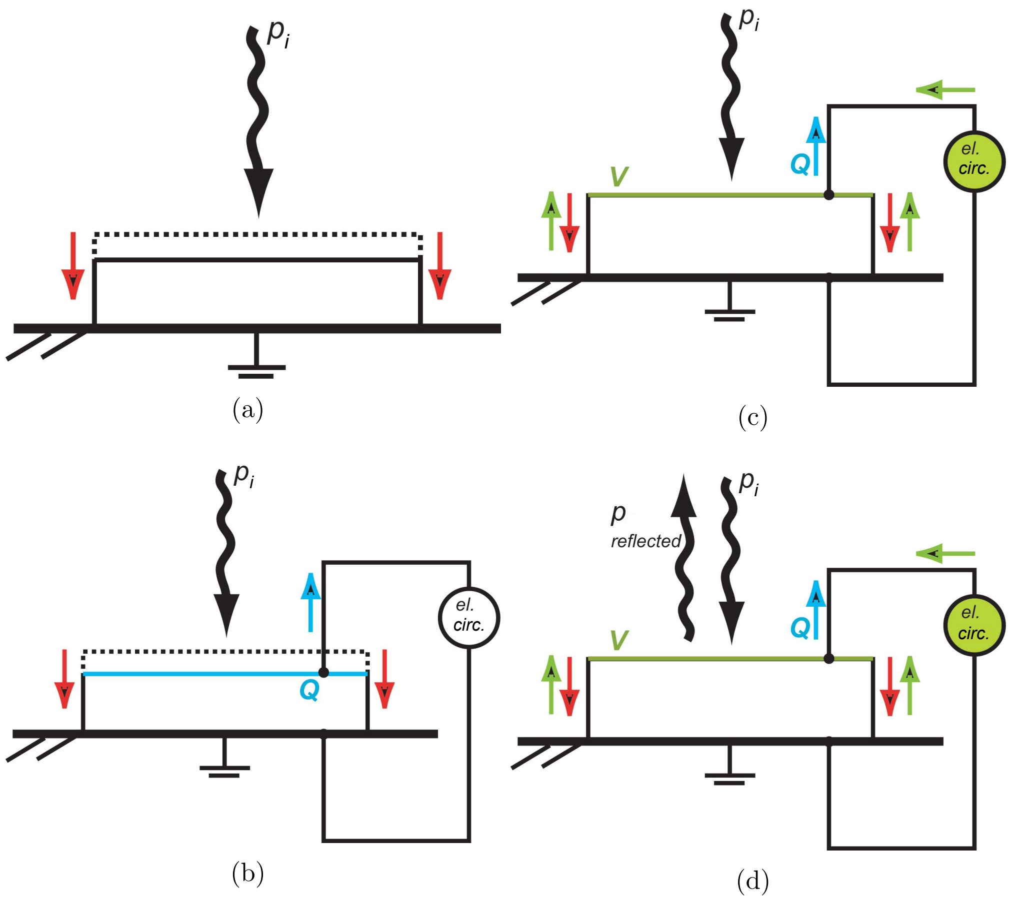

Figure 3.5: (a) The piezoelectric element is exposed to the influence of incoming acoustic pressure p_i. That means, the external mechanical force is applied to the piezoelectric element. It is deformed according to the Hooke's law (red); (b) The external force generates a charge Q on the piezoelectric element's electrodes due to the direct piezoelectric effect, the charge Q is introduced to the shunt electronic circuit (blue); (c) The electronic circuit controls the electric voltage V on the electrodes of the piezoelectric element which is deformed according to the inverse piezoelectric effect (green); (d) The total strain (the stress-induced strain (due to Hooke's law) and the voltage-induced strain (due to the converse piezoelectric effect)) of the piezoelectric actuator equals zero. This means that the effective Young's modulus of the piezoelectric actuator reaches infinity. Then, the all incoming acoustic energy is reflected from the surface and nothing is transmitted to the other side.

Chapter 4

Active elasticity control of macro fiber composite actuator

The flexible piezoelectric actuator, macro fiber composite (MFC) actuator, is introduced in this Chapter. Computation of its effective material properties and demonstration of tuning its effective elastic constants by means of a shunt electric circuit are presented here. The effective material constants are computed using the finite element method (FEM) and compared with MFC manufacturer's data. The effect of the shunt circuit capacitance on the effective non-isotropic Young's moduli is analyzed in detail. A method for finding the proper shunt circuit adjustment that yields maximum values of the MFC actuator effective non-isotropic Young's modulus is shown.

4.1 Introduction

The use of piezoelectric ceramics, such as PZT, materials for structural actuation and sensing is a well-developed field of applied material science. The PZT material itself, however, has some severe application limits. PZT transducers are extremely brittle and they require extra attention during the handling and bonding procedures. They can easily crack, when they are exposed to large mechanical stresses or deformations. In addition, their conformability to curved surfaces is extremely poor [114]. Therefore, the concept of active piezoceramic composite transducers (PCT), which would contain PZT and some flexible adhesive to eliminate the aforementioned drawbacks has been explored.

A typical PCT is made of an active layer sandwiched between two soft thin encapsulating layers. The first generation of PCT actuators were manufactured using a layer of cylindrical piezoceramic fibers embedded

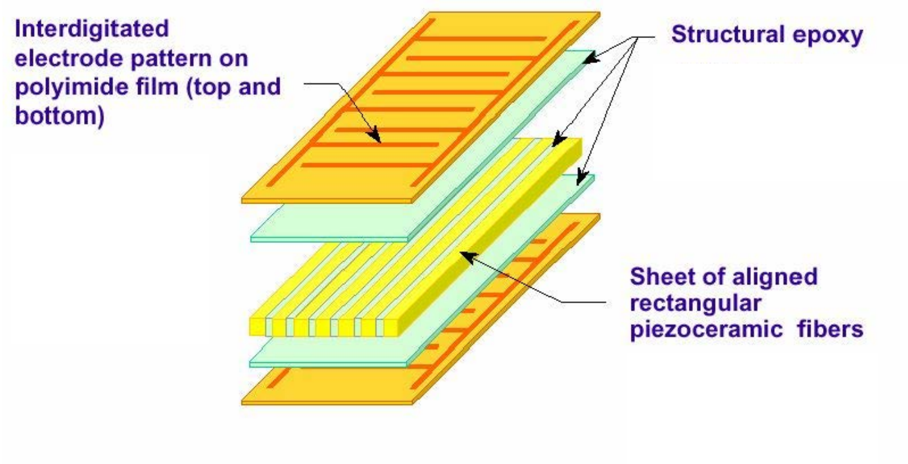

Figure 4.1: Layered structure of the macro fiber composite (MFC) actuator [117, 119]. It consits of rectangular cross-section, unidirectional piezoceramic fibers from PZT-5A lead zirconate-titanate material embedded in an epoxy matrix. It is sandwiched between copper-clad polyimid film layers that have an etched IDE pattern.

in a protective polymer matrix material. They were called Active Fiber Composite (AFC) and were introduced by Hagood and Bent [115] as an alternative to monolithic piezoceramic wafers for structural actuation applications. Strain energy density was improved by utilizing interdigital electrodes (IDEs) to produce electrical fields in the plane of the actuator [116]. However, its performance was rather limited by design and manufacturing issues. Moreover, the round cross-section fibers have minimal contact area with the copper electrodes. The new type of PCT actuator, called macro fiber composite (MFC) actuator was developed at NASA Langley Research Center to eliminate many of the manufacturing and performance disadvantages [117]. Nowadays, both of these types of actuators are produced by Smart Materials Corp. [118] and an overview and their detailed comparison are freely available at [119].

Fig. 4.1 shows a part of structure of the MFC actuator. It is a layered planar actuation device that employs rectangular cross-section, unidirectional piezoceramic fibers from PZT-5A lead zirconate-titanate material embedded in an epoxy matrix which, first, inhibits crack propagation in a ceramic and, second, bonds the actuator together. This active fiber-reinforced layer is sandwiched between copper-clad polyimid film layers that have an etched IDE pattern. Nowadays, the MFC actuator retains the most advantageous features of the early PCT actuators, namely, high strain energy density, directional actuation, conformability to all kind of surfaces and long durability. The fabrication process is uniform and repeatable so the actuator is financially accessible. Full comprehensive manual of manufacture of MFC actuator is patented by Wilkie et al. [120].

The MFC has been used primarily for structural actuation [117]. The sensing capabilities were found as excellent by Sodano [114], when compared to conventional piezoelectric polymer films (PVDF) or piezoceramic-based sensors. Due to the electromechanical coupling characteristics of piezoelectric materials, they are often used as a sensor and actuator simultaneously. The self-sensing function of the MFC actuator was tested in the work by Sodano [114] as well. The self-sensing MFC circuit was designed to suppress the vibration of the aluminum beam. Flexible piezoelectric materials have been also advantageously applied to power harvesting applications because of their ability to withstand large amounts of strain. Larger strains provide more mechanical energy available for conversion into electrical energy. The power harvesting ability of MFC was tested in the work by Sodano [121]. Several examples of various MFC applications are presented by Schönecker [122].

With the onset of design tools based on numerical computing using finite element method (FEM), a fast development of advanced devices required numerical modeling and analysis of systems with MFC actuators. It is clear that considering the detailed structure of the MFC composite would lead to enormous complexity of the numerical model and the knowledge of the mean effective material parameters of the composite transducer has become a necessity. For that reason, an increasing number of investigations, which were focused on the homogenization of composite materials, have been accomplished, in order to predict mechanical and electro-mechanical properties of piezoceramic composites.

Different techniques have been developed, such as analytical mixing rules (see e.g. [123, 124]). These methods provide an overall behavior of piezoelectric fiber composites from known properties and volume fraction of their constituents (fiber and polymer matrix). Analytical mixing rules method particularly for MFC actuator was introduced by Deraemaeker [125]. While the analytical methods are designed just for special cases of a composite geometry, FEM techniques, which are applicable to general geometries, have been used for the computation of effective electro-mechanical properties of piezo-composites (see e.g. [126, 127, 128, 129, 130]). In such models, the representative unit cell and the appropriate boundary conditions are chosen to compute particular material property component. Electromechanical equivalent properties of MFC actuator were numerically evaluated using finite element periodic homogenization in recent works by Deraemaeker [131] and Biscani [132]. Numerical methods seem to be a well-suited approach to describe the behavior of the piezo-composite materials, because there are no restrictions to the geometry, the material properties or the number of phases in the piezoelectric composite.

Recently, MFC actuators have been considered as efficient tools for the noise and vibration transmission suppression [111, A.8]. The aforementioned devices were based on the principle of the AEC method of piezoelectric materials (introduced in the work by Date et al. [90] and analyzed in detail in Chap. 3). In the paper by Date et al. [90], an analytical model for the calculation of the effective Young modulus of the piezoelectric actuator shunted by NC circuit is developed (see Eq. (3.33)). The analytical model can be applied to piezoelectric samples of a simple geometry, e.g. plates of piezoelectric ceramics, where uniform distribution electric and elastic field can be considered. Unfortunately, this is not the case of the MFC actuator, where IDEs and inhomogeneous distribution of dielectric constant produce nonuniform electric fields.

The objective of this Chapter is to present the computation of a complete set of electromechanical material parameters of the MFC actuator and to analyze the effect of NC shunt circuit on the elastic constants of the MFC actuator. A numerical model of the MFC actuator based on the FEM is developed in Sec. 4.2. In particular, the definition of the representative volume element (RVE) geometry of the MFC actuator is shown in Subsec. 4.2.1, Subsec. 4.2.2 presents a formulation of the equations of motion and specification of numerical values of material parameters, electrical and mechanical boundary conditions are specified in Subsec. 4.2.3, state quantities averaging and the method of calculation of effective elastic and piezoelectric properties are defined in Subsec. 4.2.4, and the introduction of the electromechanical interaction of the MFC actuator with the external electric circuit and the implementation of the method of active elasticity control is presented in Subsec. 4.2.5. Section 4.3 presents results of numerical computation, which includes macroscopic elastic constants of short-circuited MFC actuator (Subsec. 4.3.1), macroscopic piezoelectric constants (Subsec. 4.3.2), capacitance per unit area of the MFC actuator (Subsec. 4.3.3), macroscopic Young's moduli of a MFC actuator connected to the negative capacitance (NC) shunt circuit and the electromechanical coupling factor (Subsec. 4.3.4), precise tunning of the NC circuit (Subsec. 4.3.5), and frequency dependence of macroscopic Young's moduli of MFC actuator shunted by NC circuit (Subsec. 4.3.6).

4.2 FEM model of the MFC actuator and the computation method

In this Section, a detailed description of the MFC actuator FEM model is presented. The aim of this study presented in this Chapter is to analyze the effective elastic properties of MFC actuator, which are controlled by the negative capacitance circuit, using numerical simulations. For this purpose it is necessary to develop a realistic numerical model of the piezoelectric composite and to compute the effective elastic properties.

Composite materials, such as MFC, belong to the group of orthotropic materials. Therefore, the effective elastic properties of the MFC actuator can be represented by a matrix of elastic stiffness, introduced in Chap. 2, $\mathbf{c}_{\mathrm{MFC}}$ in a general form:

$$\mathbf{c}_{\mathrm{MFC}} = \begin{pmatrix} c_{11} & c_{12} & c_{13} & 0 & 0 & 0 \\ c_{12} & c_{22} & c_{13} & 0 & 0 & 0 \\ c_{13} & c_{13} & c_{33} & 0 & 0 & 0 \\ 0 & 0 & 0 & c_{44} & 0 & 0 \\ 0 & 0 & 0 & 0 & c_{44} & 0 \\ 0 & 0 & 0 & 0 & 0 & c_{66} \end{pmatrix}. \tag{4.1}$$

As mentioned in Subsec. 2.1.1.2, the inverse of the elastic stiffness matrix is the symmetric matrix of elastic compliances $\mathbf{s}_{\mathrm{MFC}}$ which could be defined in a form of Young's and shear moduli of the orthotropic MFC actuator:

$$\mathbf{s}_{\mathrm{MFC}} = \mathbf{c}_{\mathrm{MFC}}^{-1} = \begin{pmatrix} \frac{1}{Y_{11}} & \frac{-\nu_{21}}{Y_{22}} & \frac{-\nu_{31}}{Y_{33}} & 0 & 0 & 0 \\ \frac{-\nu_{12}}{Y_{11}} & \frac{1}{Y_{22}} & \frac{-\nu_{32}}{Y_{33}} & 0 & 0 & 0 \\ \frac{-\nu_{13}}{Y_{11}} & \frac{-\nu_{23}}{Y_{22}} & \frac{1}{Y_{33}} & 0 & 0 & 0 \\ 0 & 0 & 0 & \frac{1}{2G_{12}} & 0 & 0 \\ 0 & 0 & 0 & 0 & \frac{1}{2G_{23}} & 0 \\ 0 & 0 & 0 & 0 & 0 & \frac{1}{2G_{13}} \end{pmatrix}, \tag{4.2}$$

where Y_{11}, Y_{22}, Y_{33} are the Young's moduli, G_{12}, G_{23}, G_{13} are the shear moduli and ν_{12}, ν_{21}, ν_{13}, ν_{31}, ν_{23}, ν_{32} are the Poisson's ratios of the MFC actuator, whereas $\nu_{ij}/Y_{ii} = \nu_{ji}/Y_{jj}$.

The aforementioned elastic properties are considered as effective parameters of a large-scale/macroscopic structure. A common approach for numerical calculation of macroscopic properties of 3D piezoelectric fiber composites is to define a representative volume element (RVE) or a unit cell that captures the major features of the underlying microstructure. Then, the mechanical and physical properties of the constituent materials are always regarded as a small-scale/microstructure. Basically, the unit cell is the smallest part that contains sufficient information on the geometrical and material parameters at the microscopic level sufficient to derive the effective macroscopic properties of the composite.

4.2.1 Geometry of the FEM model

Fig. 4.2 shows the geometry of the RVE of the MFC actuator. It is placed in the coordinate system in such a way that the RVE center of mass is in the

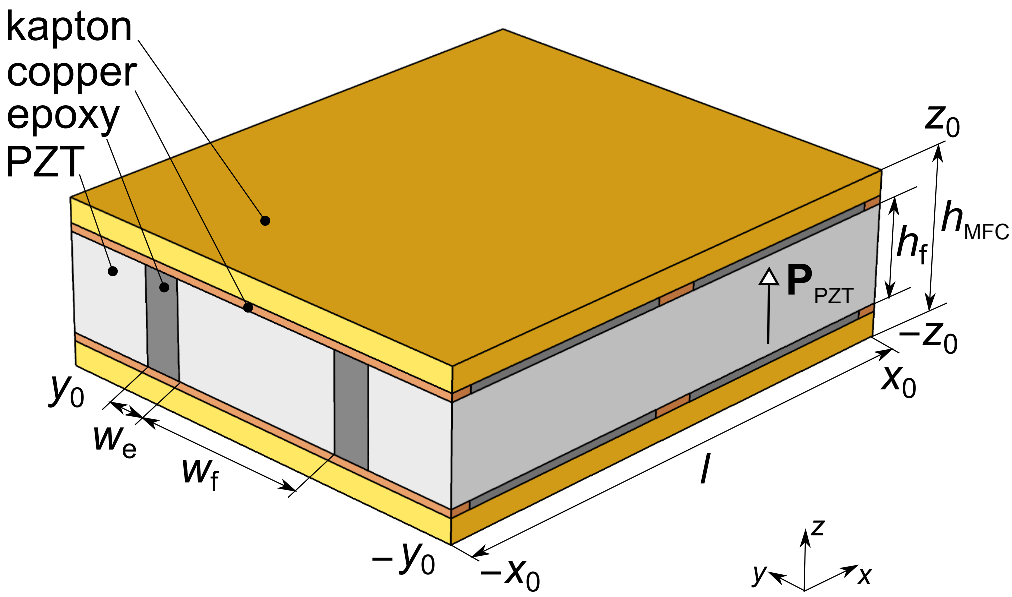

Figure 4.2: Geometry of the representative volume element model of the MFC actuator. The element length is equal to $l = 1000$ μm. Width and thickness of the PZT fiber are equal $w_f = 350$ μm and $h_f = 180$ μm, respectively. Width of epoxy gap between two PZT fibers equals $w_e = 73$ μm. The total thickness of the MFC actuator element equals $h_{\mathrm{MFC}} = 300$ μm. In MFC of P2-type, PZT fibers are polarized in the z direction. IDE copper electrodes are embedded in a thin polyimide layer. Width and pitch of each electrode finger equal 80 μm and 500 μm, respectively.

origin of the coordinate system and the PZT fibers are oriented along the x axis. The length of the cell, $l = 1000$ μm, contains two pitches of IDEs. Width and thickness of the piezo-ceramic fiber are equal $w_f = 350$ μm and $h_f = 180$ μm, respectively. Fiber fill factor equals 83%, which, according to total dimensions of MFC actuators [118], gives the width of the epoxy gap between two PZT fibers, $w_e = 73$ μm. The total thickness of the MFC actuator is equal to $h_{\mathrm{MFC}} = 300$ μm. IDE copper electrodes are embedded in a kapton layer. The electrode finger and their width pitch are equal to 80 μm and 500 μm, respectively. In this Thesis, d_{31} effect MFC actuator is analyzed (it is called MFC of P2-type at Smart Material Corp. [118]). It means that piezoelectric fibers are polarized in the z axis direction and the actuator has an additional thin metal layer on each of the PZT fiber surface.

4.2.2 Equations of motion and material properties

Fundamental equations that govern the electromechanical response of the MFC actuator are, first, the equation expressing the equilibrium of forces in the composite body, which is excited by external stimulus (i.e. mechanical force or electric field) of a harmonic time dependence with angular frequency ω:

$$-\rho\omega^2\mathbf{u} - \nabla\cdot\mathbf{T} = 0, \tag{4.3}$$

where ρ is the density of a material, $\mathbf{u}$ is the displacement vector distribution, and $\mathbf{T}$ is the mechanical stress tensor, and, second, Maxwell equation for the zero flow of electric displacement in the composite body:

$$\nabla\cdot\mathbf{D} = 0, \tag{4.4}$$

where $\mathbf{D}$ is electric displacement vector. In the case of static analyses, the angular frequency is equal to zero, i.e. $\omega = 0$.

In order to calculate the spatial distribution of electrostatic potential V and a deformation given by the displacement vector $\mathbf{u}$, it is necessary to introduce the complementary state quantities: the elastic strain tensor $\mathbf{S}$:

$$\mathbf{S} = \frac{1}{2}[(\nabla\mathbf{u})^T + \nabla\mathbf{u}] \tag{4.5}$$

and the electric field $\mathbf{E}$:

$$\mathbf{E} = -\nabla V. \tag{4.6}$$

In the isotropic non-piezoelectric material (i.e. epoxy, polyimide and copper), the relation between the above state quantities are given by constitutive equations that express the Hooke's law and the linear relationship between electric displacement and electric field,

$$\begin{aligned} \mathbf{S} &= \frac{1}{Y}\mathbf{T} - \frac{\nu}{Y}(\mathrm{tr}(\mathbf{T})\,\mathbf{I} - \mathbf{T}), && (4.7)\\ \mathbf{D} &= \epsilon_0\epsilon_r\,(1 - j\eta)\,\mathbf{E}, && (4.8) \end{aligned}$$

where Y and ν are Young's modulus and Poisson's ratio of an isotropic material, respectively. The symbol $\mathbf{I}$ stands for the second-order identity matrix. Symbols ϵ_0 and ϵ_r are the permittivity of a vacuum and dielectric constant of the material, respectively. Symbol η is the dielectric loss factor.

Material parameters of all isotropic composite constituents used in the numerical model are listed in Table 4.1. Particularly, epoxy material properties are just estimated values according to various existing general epoxy adhesives (i.e. Aremco Products, Inc. [133]) because the real data are under the producer's trade secret according to their NASA license agreement.

Material parameter	epoxy	polyimid	copper	unit
Young's modulus	$3.3 \cdot 10^9$	$3.1 \cdot 10^9$	$110 \cdot 10^9$	Pa
Poisson's ratio	0.3	0.34	0.35	1
Density	1300	1420	8700	kg$\cdot$ m^{-3}
Relative permittivity	3	3.4	-	1
Dielectric loss factor	0.01	0.02	-	1

Table 4.1: Material parameters of epoxy, polyimid and copper used in simulations of MFC actuator.

Material parameter		value	unit
Elastic compliance	$s_{11} = s_{22}$	16.4	10^{-12} m^2/N
	s_{33}	18.8	
	$s_{13} = s_{23}$	-7.22	
	s_{12}	-5.74	
	$s_{44} = s_{55}$	47.5	
	s_{66}	44.3	
Piezoelectric coefficient	$d_{15} = d_{24}$	584	10^{-12} C/N
	$d_{31} = d_{32}$	-171	
	d_{33}	374	
Relative permittivity	$\epsilon_{11} = \epsilon_{22}$	1730	$8.854 \cdot 10^{-12}$ F/m
	ϵ_{33}	1700	
Dielectric loss factor	η	0.02	1

Table 4.2: Material parameters of PZT-5A (polarized along z-axis) that represents the functional part of the MFC actuator.

In the piezoelectric material, the constitutive equations are given by set of Eqs. 2.1, rewritten in the following matrix form:

$$\begin{aligned} \mathbf{D} &= [\epsilon^T]\,(\mathbf{I} - j\eta\mathbf{I})\,\mathbf{E} + [d]\mathbf{T}, \\ \mathbf{S} &= [d]\mathbf{E} + [s^E]\mathbf{T}, \end{aligned} \tag{4.9}$$

where $[s^E]$ are the elastic coefficients matrix for constant electric field, $[d]$ is the piezoelectric coefficients matrix, $[\epsilon^T]$ is the dielectric permittivity matrix at constant mechanical stress, and η is the dielectric loss factor.

The piezoelectric material of the composite fibers in our numerical model is the commonly used piezoelectric ceramic PZT-5A (e.g. in [134]). The numerical values of material parameters adopted in our model are presented in Table 4.2.

4.2.3 Boundary conditions

In order to extent the validity of material parameters that were computed for the RVE of the MFC actuator to the full-size MFC actuator, several boundary conditions must be carefully specified.

4.2.3.1 Electrical boundary conditions

In all our simulations, we consider a defined voltage on IDE electrodes of the MFC actuator. The bottom IDE electrode is grounded in all simulations. The top IDE electrode is considered grounded in the simulations of elastic parameters Y_{ii}, G_{ij}, and ν_{ij}. The applied testing voltage $V_0 = 100\,\mathrm{V}$ to the top IDE electrode is considered in the simulations of static capacitance per unit area of the MFC actuator and the piezoelectric coefficients d_{3i}.

The charge generated on the top IDE electrode is computed using a standard formula of electrostatics:

$$Q_0 = -\oint_{S_E} D_i n_i dS, \tag{4.10}$$

where S_E is the surface of the electrode, D_i is the electric displacement in a dielectric at the point of contact with the electrode, and n_i is the outer normal vector of the electrode.

The top and bottom surfaces are considered to be electrically isolated, i.e. they are on a floating potential and with the absence of free charge.

4.2.3.2 Periodic boundary conditions

If it is not specified otherwise, we consider following periodic boundary conditions:

$$u_y(-x_0, y, z) = u_y(x_0, y, z), \qquad u_{y,x}(-x_0, y, z) = u_{y,x}(x_0, y, z), \tag{4.11a}$$

$$u_z(-x_0, y, z) = u_z(x_0, y, z), \qquad u_{z,x}(-x_0, y, z) = u_{z,x}(x_0, y, z), \tag{4.11b}$$

$$V(-x_0, y, z) = V(x_0, y, z), \qquad V_x(-x_0, y, z) = V_x(x_0, y, z), \tag{4.11c}$$

$$u_x(x, -y_0, z) = u_x(x, y_0, z), \qquad u_{x,y}(x, -y_0, z) = u_{x,y}(x, y_0, z), \tag{4.11d}$$

$$u_z(x, -y_0, z) = u_z(x, y_0, z), \qquad u_{z,y}(x, -y_0, z) = u_{z,y}(x, y_0, z), \tag{4.11e}$$

$$V(x, -y_0, z) = V(x, y_0, z), \qquad V_y(x, -y_0, z) = V_y(x, y_0, z), \tag{4.11f}$$

where V_x and V_y are partial derivatives of the electrostatic potential V with respect to x and y, respectively. The above Eqs. (4.11) express the continuity of electrostatic voltage and tangential components of a displacement at the surfaces parallel to the z-axis.

The boundary conditions for the normal component of the displacement at the surfaces parallel to the z-axis are more complicated and it is discussed in the next Subsection.

4.2.3.3 Boundary conditions for the flatness of RVE surfaces

Inhomogeneity and strong anisotropy of the MFC actuator rather complicate the mechanical boundary conditions for normal components of the displacement. The reason is following: when the electric voltage is applied to IDE electrodes, PZT fibers expand, while the epoxy matrix does not. This yields the presence of inhomogeneous shear stress distributed along the RVE surfaces at $x = \pm x_0$ and $y = \pm y_0$. If such an inhomogeneous stress is not compensated by a proper boundary condition in the numeric model of the MFC actuator, it yields bulging the RVE surfaces. Such a bulging of the RVE surfaces violates the requirements for periodicity imposed on the RVE model. Unfortunately, introduction of the proper boundary condition is not a straightforward task, since it must allow the uniform expansion of the whole volume of the RVE element.

To avoid bulging the RVE surfaces, the average normal displacements of the RVE surfaces could be introduced by following formulae:

$$\overline{u_x(\pm x_0)} = \frac{1}{4y_0 z_0}\int_{-y_0}^{y_0} dy \int_{-z_0}^{z_0} u_x(\pm x_0, y, z)dz, \qquad (4.12)$$

$$\overline{u_y(\pm y_0)} = \frac{1}{4x_0 z_0}\int_{-x_0}^{x_0} dy \int_{-z_0}^{z_0} u_x(x, \pm y_0, z)dz. \qquad (4.13)$$

In the next step, we introduce local surface external forces $\mathbf{f}$ (in N·m^{-2}):

$$\mathrm{f}_x(\pm x_0, y, z) = \pm\gamma \left[u_x(\pm x_0, y, z) - \overline{u_x(\pm x_0)}\right], \qquad (4.14)$$

$$\mathrm{f}_y(x, \pm y_0, z) = \pm\gamma \left[u_y(x, \pm y_0, z) - \overline{u_y(\pm y_0)}\right], \qquad (4.15)$$

where γ is the elastic stiffness of the “surface” region of the RVE element. Its numeric value is set in the model to be several orders of magnitude higher than the average Young’s modulus of PZT. Finally, we introduce the boundary condition in the form

$$\mathbf{T} \cdot \mathbf{n} = \mathbf{f}, \qquad (4.16)$$

where $\mathbf{n}$ is the normal vector to the particular surface of the RVE element.

The physical meaning of the above type of a boundary condition can be explained as follows: Such type of a boundary condition allows the nonzero values of the uniform/average normal strains S_{xx} and S_{yy}, which is controlled by bulk values of material parameters. On the other hand, the inhomogeneity and anisotropy of the MFC actuator may produce bulging the particular RVE surface, i.e. local deviations of the displacement from its average value calculated over the particular surface. In order to keep the particular surface of the RVE element approximately flat, we introduce into the model a local external force, which acts on the particular RVE surface and which is proportional to the difference between local and average values of displacement and acts in the opposite direction. Using this procedure, it is possible to approximate the requirement for the flatness of the RVE surfaces with arbitrarily high accuracy.

4.2.4 Averaging of state quantities and effective elastic and piezoelectric properties

As it was introduced earlier in this Section, composite materials such as MFC actuators can be represented as a periodical array of RVEs. Therefore, periodic boundary conditions must be introduced to the numerical model [135]. This implies that each RVE in the composite has the same deformation mode and there is no separation or overlap between the neighboring RVEs.

It is assumed that the average mechanical and electrical properties of a RVE are equal to the average properties of the particular composite. The average stresses $\overline{T_{ij}}$ and strains $\overline{S_{ij}}$ in the RVE are calculated using formulas:

$$\overline{T_{ij}} = \frac{1}{V}\int_V T_{ij}dV, \tag{4.17a}$$

$$\overline{S_{ij}} = \frac{1}{V}\int_V S_{ij}dV, \tag{4.17b}$$

where V is the RVE volume. Then, the effective Young's moduli Y_{ii}, shear moduli G_{ij}, and Poisson ratios ν_{ij} can be expressed as:

$$Y_{ii} = \frac{\overline{T_{ii}}}{\overline{S_{ii}}}, \tag{4.18a}$$

$$G_{ij} = \frac{\overline{T_{ij}}}{2\overline{S_{ij}}}, \tag{4.18b}$$

$$\nu_{ij} = -\frac{\overline{S_{ii}}}{\overline{S_{jj}}}. \tag{4.18c}$$

When one needs to compute all effective elastic properties of the composite (i.e. Young's and shear moduli), it is necessary to apply macroscopic boundary conditions, which are specified in Table 4.3 for each analysis of the appropriate component of the Young's or shear modulus. As mentioned above, both IDEs are considered being grounded (i.e. $V_{IDE+} = 0$ V and $V_{IDE-} = 0$ V).

In a similar way, our FEM model of the MFC actuator allows a simple method for the computation of the effective piezoelectric constants of the

Material parameter	RVE surface	Testing force direction
Y_{11}	$x = \pm x_0$	$(\pm 1,\ 0,\ 0)$
Y_{22}	$y = \pm y_0$	$(0,\ \pm 1,\ 0)$
Y_{33}	$z = \pm z_0$	$(0,\ 0,\ \pm 1)$
G_{12}	$x = \pm x_0$	$(0,\ \pm 1,\ 0)$
	$y = \pm y_0$	$(\pm 1,\ 0,\ 0)$
G_{23}	$y = \pm y_0$	$(0,\ 0,\ \pm 1)$
	$z = \pm z_0$	$(0,\ \pm 1,\ 0)$
G_{13}	$z = \pm z_0$	$(\pm 1,\ 0,\ 0)$
	$x = \pm x_0$	$(0,\ 0,\ \pm 1)$

Table 4.3: Specification of the mechanical boundary conditions considered in the computation of particular effective elastic constants. RVE surfaces are specified using following constants: $x_0 = (1/2)l$, $y_0 = (1/2)(w_e + w_f)$, and $z_0 = (1/2)h_{\mathrm{MFC}}$.

MFC actuator. In this case, a specific testing voltage V_0 is applied to the MFC actuator electrodes and the average strain in the RVE is computed. Then the average piezoelectric moduli are calculated according to following formula:

$$d_{3ii} = \frac{\overline{S_{ii}}\, h_{\mathrm{MFC}}}{V_0}. \tag{4.19}$$

Using this approach, computed values of piezoelectric moduli correspond to a situation where the MFC actuator is replaced by a uniform piezoelectric medium with top and bottom parallel plate electrodes.

4.2.5 Electromechanical interaction and the principle of AEC method adapted to MFC actuator elasticity control

As introduced before (see Chap. 3, Sec. 3.3), the electrical boundary conditions of piezoelectric actuators greatly affect their effective elastic properties. The role of electromechanical interaction on the effective elastic properties can be amplified if an active shunt circuit is connected to the piezoelectric actuator by means of AEC method. The essential point of the control of effective elastic properties of the MFC actuator can be explained using the an over-simplified model of the MFC actuator, where the movement in x axis direction is considered only.

Fig. 4.3 shows the scheme of d_{31}-effect type MFC actuator placed in the system of coordinates. PZT fibers enclosed by an epoxy material are

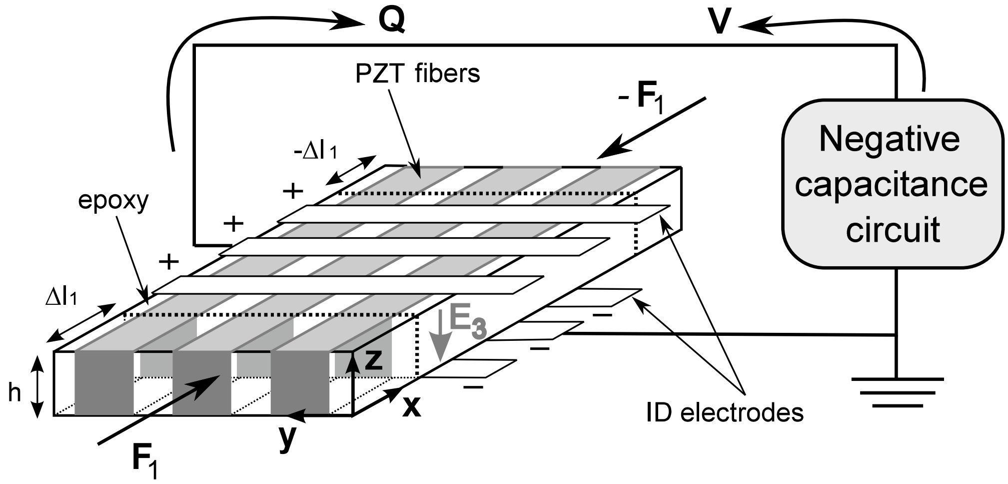

Figure 4.3: Scheme of the macro fiber composite (MFC) actuator of d_{31}-effect type placed in the system of coordinates. PZT fibers enclosed by an epoxy material are arranged along the x axis and polarized in the z axis direction. Top and bottom layers of IDEs are indicated. The mechanical force F_1 is applied to the piezoelectric element and causes the displacement Δl_1. NC shunt circuit is connected to the MFC actuator. Charge Q generated on IDE electrodes of the MFC actuator due to the direct piezoelectric effect is introduced to the shunt circuit and the electric voltage is fed back to the IDE electrodes. The total strain of the MFC actuator is given by the sum of the stress-induced strain (according to the Hookes's law) and the voltage-induced strain (due to converse piezoelectric effect).

arranged along the x axis and polarized in the z axis direction. The bottom IDEs are grounded and the top IDEs are connected to the NC shunt circuit. When the external force F_1 is applied to the MFC actuator, the in-plane strain S_{11} is produced according to the Hooke's law. In the piezoelectric MFC actuator, the external force F_1 generates a charge Q on the IDEs due to the direct piezoelectric effect. The generated charge is introduced to the shunt circuit, which controls the electric voltage V on the IDE electrodes. The total strain S_{11} of the MFC actuator is then equal to the sum of both: the stress-induced strain (due to Hooke's law) and the voltage-induced strain (due to the converse piezoelectric effect). When the voltage-induced strain cancels the stress-induced strain, the total strain of the MFC actuator equals zero which actually means that the effective Young's modulus of the MFC actuator could reach infinity.

In this particular arrangement, it is possible to analytically derive the effective value of the Young's modulus component Y_{11} of the MFC actuator. Again, the equations of state for the average electric displacement $\overline{D_3}$ and strain $\overline{S_{11}}$ in the MFC actuator has to be employed:

$$\begin{aligned} \overline{D_3} &= \epsilon_{33}^T \overline{E_3} + d_{311} \overline{T_{11}}, \\ \overline{S_{11}} &= d_{311} \overline{E_3} + s_{1111}^E \overline{T_{11}}. \end{aligned} \tag{4.20}$$

These equations are appended by the Eq. 3.32 for the voltage $V = \overline{E_3} h$ applied back to the MFC electrodes from the external capacitor of capacitance C. The electric charge Q generated on the electrodes of the MFC actuator of an area A could be expressed by the formula $Q = \overline{D_3} A$. Symbols ϵ_{33}^T, d_{311} and s_{1111}^E stand for the permittivity, piezoelectric coefficient, and elastic coefficient of the MFC actuator with short-circuited electrodes, respectively, i.e. the tensor components which play the role when the movement in x axis direction is considered only.

Combining Eqs. 4.20 and 3.32, it is possible to obtain the formula for the effective Young's modulus, particularly Y_{11}, of the MFC actuator shunted by the external capacitor with capacitance value C which is the key parameter, which controls the value of the effective elastic constant:

$$Y_{11,\mathrm{sh}} = \frac{\overline{T_{11}}}{\overline{S_{11}}} = \frac{1}{s_{1111}^E} \left(1 + \frac{k_{311}^2}{1 - k_{311}^2 + \alpha} \right), \tag{4.21}$$

where k_{311} is the electromechanical coupling factor of the MFC actuator when the electric filed is in the z direction and the deformation of the element is considered in x direction, $\alpha = C/C_S$ is the ratio of the shunt circuit capacitance C over the piezoelectric element static capacitance C_S, where $C_S = \epsilon_{33}^T A/h_f$.

Again, the condition when the effective Young's modulus theoretically reaches infinity, could be derived from Eq. 4.21:

$$C = -(1 - k_{311}^2) C_S, \tag{4.22}$$

This simplified analytical model serves as explanation of the theoretical ideas of active "stiffening" of MFC actuator. Using the FEM simulations electromechanical interaction of the MFC actuator with a NC shunt circuit could be analyzed in more complex way. In the next Section, there will be presented results of our FEM model of the MFC actuator and the calculation of its macroscopic effective material parameters.

4.3 Results of FEM model simulations and discussion

At first, results of FEM model simulations of the effective elastic properties of a short-circuited MFC actuator will be presented. Second, frequency dependence of the capacitance is computed time-dependent FEM

Material parameter	FEM model (this work)	Deraemaeker et al. [125]	Williams et al. [136]	Producer's datasheet [118]
Y_{11} (10^9 Pa)	32.58	27.27	29.4	30.34
Y_{22} (10^9 Pa)	15.33	14.76	15.2	15.86
Y_{33} (10^9 Pa)	9.37	-	-	-
G_{12} (10^9 Pa)	5.26	4.13	6.06	5.52
G_{23} (10^9 Pa)	2.47	-	-	-
G_{13} (10^9 Pa)	2.76	-	-	-
ν_{12} (1)	0.313	0.303	0.312	0.310
ν_{21} (1)	0.147	-	0.161	0.160
ν_{13} (1)	0.405	-	-	-
ν_{31} (1)	0.116	-	-	-
ν_{23} (1)	0.334	-	-	-
ν_{32} (1)	0.188	-	-	-

Table 4.4: Comparison of elastic parameters of the MFC (P2-type) actuator computed using FEM model (this work), analytical mixing rules by Deraemaeker et al. [125], experimental measurements by Williams at al. [136], and MFC producer's datasheet values [118].

model. Third, the static FEM model will be used to analyze the electromechanical interaction of the MFC actuator with a NC shunt circuit. And finally, frequency dependence of elastic properties is computed using a time-dependent FEM model.

4.3.1 Macroscopic elastic properties of a short-circuited MFC actuator

Using the developed FEM model and adopting the sets of Eqs. (4.17) and (4.18) and specifying the boundary conditions stated in Table 4.3, effective elastic constants were computed and compared with data obtained using analytical mixing rules and classical laminate theory by Deraemaeker [125], with results of experimental measurements by Williams at al. [136], and with values from the producer's datasheet [118]. The comparison is presented in Table 4.4. We can see an acceptable agreement of the results computed in this work with the producer's values and with values obtained using another computational method.

The next Subsection presents results of the computation of macroscopic piezoelectric properties of the MFC actuator.

Material parameter	FEM model (this work)	Producer's datasheet [118]
S_{11}/V_0 (ppm/V)	-0.89	-1.1
S_{22}/V_0 (ppm/V)	-0.65	-
S_{33}/V_0 (ppm/V)	1.45	-
d_{31} (pm/V)	-267	-330
d_{32} (pm/V)	-196	-
d_{33} (pm/V)	425	-

Table 4.5: Comparison of free strain values S_{ii} produced by the testing voltage V_0 in the MFC (P2-type) actuator computed using FEM model (this work) and MFC producer's datasheet values [118]. The free strain per voltage values were recalculated to the effective piezoelectric moduli d_{3i} that correspond to a situation where the MFC actuator is replaced by a uniform piezoelectric with identical geometrical dimensions and top and bottom parallel plate electrodes.

4.3.2 Macroscopic piezoelectric properties of a MFC actuator

In this Subsection, the mechanical response of the MFC (P2-type) actuator to the testing voltage V_0 applied to the electrodes is analyzed. First, the testing voltage V_0 was applied to the upper IDEs of the MFC actuator and the average strain $\overline{S_{ii}}$ of the mechanically free RVE of the MFC actuator was computed. Free strain values per volt were computed and compared with MFC producer's datasheet values [118]. The comparison is presented in Table 4.5.

According to Eq. (4.19), the computed free strain values per volt were used for the calculation of the effective piezoelectric moduli d_{3ii} that correspond to a situation where the MFC actuator is replaced by a uniform piezoelectric with identical geometrical dimensions and top and bottom parallel plate electrodes.

The next Subsection presents results of computation of the static capacitance per unit area of the MFC actuator.

4.3.3 Capacitance per unit area of the MFC actuator

The static capacitance of the MFC actuator $C_{S,0}$ and the capacitance of the MFC actuator, which is driven by a harmonic voltage on electrodes, $C_{S,\omega}$ were computed using our FEM model.

The static capacitance is given by the fundamental formula of electro-

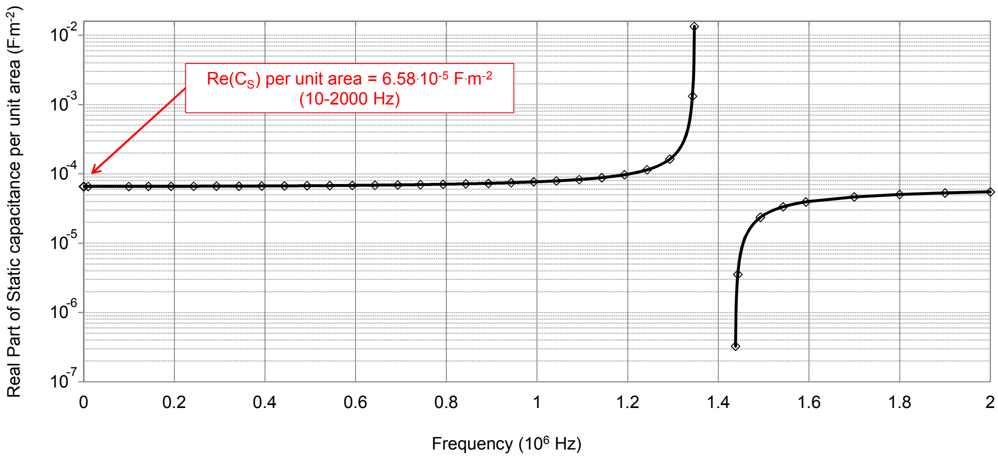

Figure 4.4: Frequency dependence of real part of capacitance $C'_{S,\omega}(f)$ of the MFC actuator. The resonant frequency is $f_r = 1.34$ MHz.

statics:

$$C_{S,0} = Q_0/V_0, \tag{4.23}$$

where V_0 is a testing voltage applied to the top IDE electrode and Q_0 is the total free charge generated on the surface of that electrode. Bottom IDE electrode is grounded. Elastic boundary conditions corresponds to mechanically free sample.

When the MFC actuator is driven by a harmonic voltage of angular frequency ω, the dielectric relaxation and piezoelectric resonance of the MFC actuator takes place. Then, below the resonance frequency, the capacitance of the MFC actuator is considered complex and it is written in the form:

$$C_S^* = C'_S + jC''_S = C'_S(1 - j\eta_S), \tag{4.24}$$

where C'_S and C''_S are the real and imaginary parts of capacitance, respectively. Symbol $\eta_S = -C''_S/C'_S$ is the dielectric loss factor of the MFC actuator. Value of static capacitance per unit area of the MFC actuator was computed using the static analysis of the model. In the next step, a harmonic voltage of angular frequency ω to the top IDE was applied and the frequency analysis in the range from 10 Hz to 2 MHz was performed. The result is shown in Fig. 4.4. The resonant frequency of the RVE of the MFC actuator is $f_r = 1.34$ MHz. Numerical results of the both static and frequency analyses indicate, that the real part of capacitance C'_S is practically identical to the static capacitance $C_{S,0}$ in a wide frequency range below the resonant frequency.

Results of static capacitance and dielectric loss factor obtained from the developed FEM model and are presented in Table 4.6. The computed

Material parameter	FEM model (this work)	Analytical formula Eq. (4.25)	Producer's datasheet [118]
$C_{S,0} = C'_S$ (10^{-5} F·m^{-2})	6.78	6.92	6.63
η_S (1)	0.010	-	-

Table 4.6: Results of the computed capacitance per unit area of the MFC (P2-type) actuator and the dielectric loss factor of the MFC (P2-type) actuator. Computed values are compared with rough estimate values using the formula for the capacitance of a capacitor with different dielectrics placed next to each other, and with the value obtained from the producer's datasheet [118]. It is seen that the values are in a reasonable agreement.

value of static capacitance is compared, first, with the value calculated from producer's datasheet [118], and, second, with a rough estimate of the static capacitance per unit area of a capacitor, which is formed by in-parallel connection of two capacitors of the same thickness but with different dielectric constants. The rough analytical estimate is then given by a basic formula:

$$\frac{C_{MFC}}{S_1 + S_2} = \frac{\epsilon_0 (S_1 \epsilon_{1,r} + S_2 \epsilon_{2,r})}{h\,(S_1 + S_2)}, \tag{4.25}$$

where S_1, S_2 and $\epsilon_{1,r}$, $\epsilon_{2,r}$ are the surfaces and relative permittivities of each single component of the dielectric, respectively. The two dielectrics are in this case PZT-5A and the epoxy material. The $\epsilon_{2,r}$ is equal to ϵ_{33}^T of PZT-5A and h is equal to the fiber/epoxy thickness h_f. Results shown in Table 4.6 indicate that the computed value of static capacitance per unit area of MFC actuator is in a good agreement with the producer's value.

The next Subsection presents results of computation of the macroscopic elastic properties of a MFC actuator, which is shunted by NC circuit. Calculated parameters, shown in Table 4.4, are considered as reference values in the analysis below.

4.3.4 Negative capacitance shunt and electromechanical coupling coefficient

When the MFC actuator is shunted by the NC circuit, the effective Young's modulus Y_{11} of the dominant vibrational mode is changed according to the formula given by the Eq. 4.21. It is possible to implement the effect of the NC circuit into the FEM model as an electric circuit boundary condition on the top electrode while the bottom IDE electrode remains grounded.

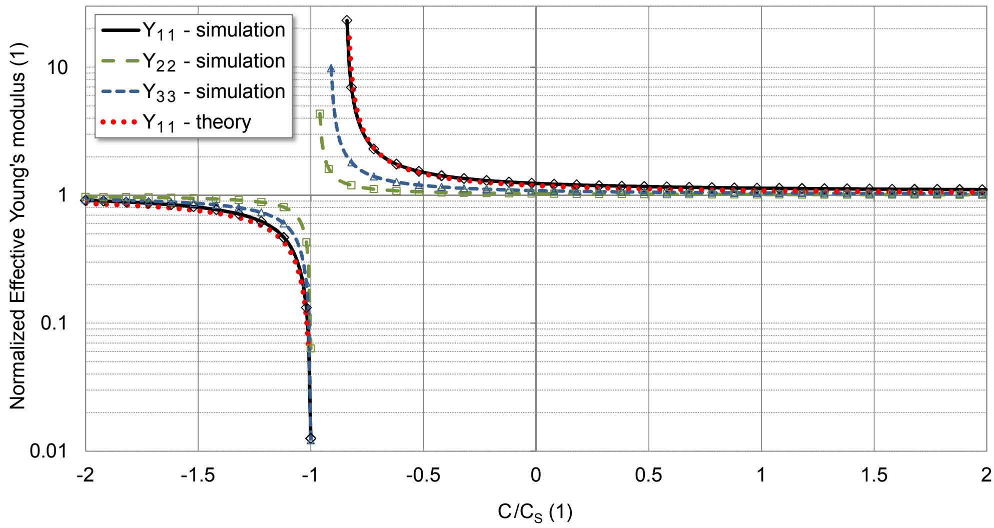

Figure 4.5: Normalized effective value of Young's moduli Y_{11}, Y_{22} and Y_{33} of MFC actuator dependent on the various adjustment of NC circuit. The parameter $\alpha = C/C_S$ is ranged from -2 to 2. Strong dependence of Young's moduli on the parameter α could be seen. From the distinguishable maximal value of the Young's modulus Y_{11} it is possible to estimate the effective electromechanical coupling coefficient k_{311} and then compute the theoretical dependence of Y_{11} on the parameter α (redb dotted line) which corresponds to the simulated data.

The circuit connected in-parallel to the top electrode of the MFC actuator is a capacitor with a capacitance denoted by a symbol C.

Since the MFC actuator is a composite structure with orthotropic elastic properties, it is appropriate to perform the analysis for effective Young's moduli Y_{11}, Y_{22}, and Y_{33} and effective shear moduli G_{12}, G_{13}, and G_{23} computation independently. For each case, the specific testing force is applied in a certain direction to a particular surface of the RVE of the MFC actuator as it is introduced in Table 4.3. Then, the charge generated on the top electrode due to the action of the testing force via direct piezoelectric effect is introduced to the shunt circuit of capacitance C and the voltage is applied back to the top electrode of the MFC actuator. Then the macroscopic stresses and strains in the RVE are computed using Eqs. 4.17 taking into account the converse piezoelectric effect in PZT fibers. The value of the applied voltage is controlled by the capacitance of the shunt capacitor C, whose value is parametrized using the formula $C = \alpha C_S$, where α is a real number running through the interval from -2 to 2.

Values of effective Young moduli of the MFC actuator were computed

Electromechanical coupling factor (1)	FEM model (This work)	Williams et al. [136]	Producer's datasheet [118]
k_{31}	0.339	0.357	0.362
k_{32}	0.177	0.213	0.218
k_{33}	0.286	-	-

Table 4.7: Comparison of computed values of the electromechanical coupling factors of the MFC (P2-type) actuator with a rough estimate calculated from the datasheet values. There is seen a reasonable agreement.

using Eqs. 4.18 and normalized using the reference values presented in Table 4.4. The normalized values of Young moduli plotted as functions of the parameter α are presented in Fig 4.5. It is seen that the values of the Young's moduli of MFC actuator are strongly influenced by the shunt circuit capacitance. On the other hand, all shear moduli have constant values with no influence of the shunt capacitance (for the clear arrangement of the picture, the constant curves are not shown in Fig. 4.5).

The curve of the normalized Young's moduli can be compared with theoretical formula Eq. 3.33. In accordance with the theory, results of our computations show that, when α approaches -1, the values of Young's moduli Y_{11}, Y_{22}, and Y_{33} are decreased by the factor of approximately 1/100. In the same way, when α approaches $-1-k_{3ii}^2$, the values of Young's moduli Y_{ii} are increased by a factor of approximately 100. Using curves presented in Fig. 4.5, the values of effective electromechanical coupling factors can be obtained. Table 4.7 presents the values of electromechanical coupling factors k_{3ii}, which were calculated using the least squares method.

4.3.5 Electrical properties of the NC circuit

The electrical scheme of a system, where the piezoelectric MFC actuator is shunted by a circuit that realizes negative values of capacitance, is shown in Fig. 4.6. The NC shunt circuit is realized as a negative impedance converter circuit (i.e. a one port circuit with an operational amplifier), where the reference impedance is realized as a capacitor C_0 connected in-series to the resistor R_0. The effective value of the shunt circuit capacitance is given by the formula:

$$C(\omega) = -\left(\frac{C_0}{1 + j\omega R_0 C_0}\right)\frac{R_2}{R_1}. \tag{4.26}$$

By proper adjustment of tunable resistors R_0 and R_1, the real and imaginary part of the shunt circuit effective capacitance can be adjusted in such

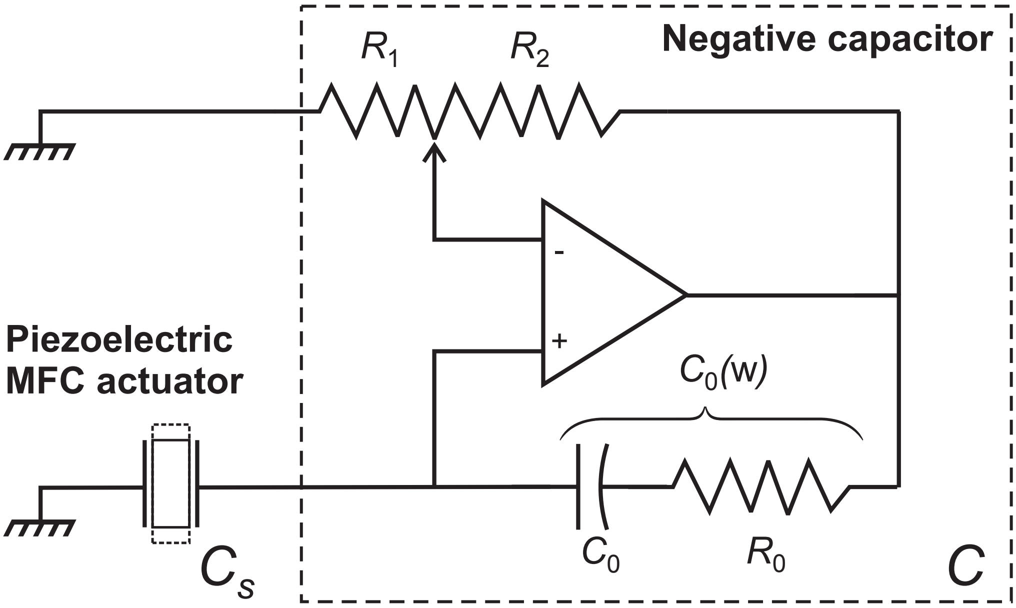

Figure 4.6: Electrical scheme of the piezoelectric MFC actuator shunted by the circuit that realizes negative values of effective capacitance. Symbol C_S stands for the piezoelectric element static capacitance, C_0 is the reference capacitance and R_0 and R_1 are tunable resistors.

a way that the condition given by Eq. (4.22) is satisfied and the effective Young's modulus of the MFC actuator is increased by several orders of magnitude.

The proper adjustment of tunable resistors R_0 and R_1 can be found from Eq. (4.22). For the sake of clarity, it is convenient to express Eq. (4.26) in the form

$$C(\omega) = C'(\omega)\left[1 - j\,\eta(\omega)\right], \tag{4.27}$$

where

$$C'(\omega) = -\frac{C_0 R_2}{R_1\left[1+\eta^2(\omega)\right]}, \tag{4.28a}$$

$$\eta(\omega) = \omega C_0 R_0. \tag{4.28b}$$

Since the capacitance of the RVE of the MFC actuator is practically frequency independent below the resonance frequency (see Fig. 4.4) and the NC circuit shown in Fig. 4.6 has a pronounced frequency dependence, it is evident that the condition given by Eq. (4.22) can be satisfied at a single frequency $\omega_0 = 2\pi f_0$. Thus, Eqs. (4.24) and (4.27) and the condition given

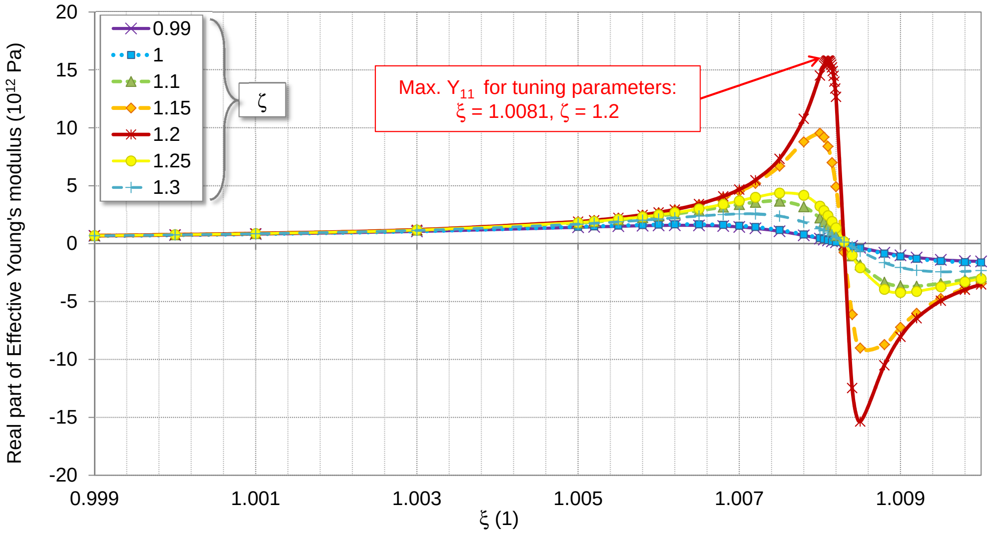

Figure 4.7: Tuning procedure of the capacity value of the NC circuit in order to maximize the real part of Young's modulus Y_{11}. Parameter of the curves is the parameters ζ. For each value of the parameter ζ, the effective value of the Young's modulus is plotted versus the value of the parameter ξ. It is seen that the Young's modulus reaches the greatest values for $\zeta = 1.2$ and $\xi = 1.0081$.

by Eq. (4.22) yield the following optimal values of resistances:

$$R_{0,\mathrm{opt}} = \frac{\eta_S}{\omega_0 C_0}, \tag{4.29a}$$

$$R_{1,\mathrm{opt}} = \frac{R_2\, C_0}{\left(1 - k_{31}^2\right)\, C'_S\, \left(1 + \eta_S^2\right)}. \tag{4.29b}$$

In order to demonstrate the sensitivity of the NC circuit adjustment, it is convenient to rewrite the frequency dependence of the NC circuit into following parametrized form:

$$C(\omega) = -\frac{\xi\left(1 - k_{311}^2\right)\, C'_S\, \left(1 + \eta_S^2\right)}{1 + j\zeta(\omega/\omega_0)\eta_S}, \tag{4.30}$$

where $\xi = R_{1,\mathrm{opt}}/R_1$ and $\zeta = R_0/R_{0,\mathrm{opt}}$.

Although the above theoretical procedure seems to be simple, the system is very sensitive to slight deviations from its optimal adjustment. To demonstrate that phenomenon, the sensitivity of the Young's modulus Y_{11} effective value to parameters ξ and ζ at the fixed critical frequency $f_0 = 850$ Hz was performed. The tuning analysis is focused on the Young's modulus Y_{11} because this component represents the dominant operational mode of the MFC actuator of the d_{31}-effect studied in this Thesis. A parametric analysis at the critical frequency was performed for the the parameters, ζ in an interval from 0.99 to 1.3 and ξ in an interval from 0.999 to 1.01. The macroscopic values of Y_{11} were computed using a formula Eq. 4.18. The effective real part of Young's modulus Y_{11} is shown in Fig. 4.7. The presented curves differ in the parameter ζ. For each value of the parameter ζ, the effective value of the Young's modulus is plotted versus the value of the parameter ξ. It is seen that the Young's modulus reaches the greatest values for $\zeta = 1.2$ and $\xi = 1.0081$.

4.3.6 Frequency dependence of effective Young moduli of the MFC actuator

Due to the mismatch in frequency dependencies of the MFC actuator and the NC circuit capacitances, the essentially enhanced values of the Young's modulus can be achieved only in a narrow frequency range, as it was introduced before. Using the computed parameters ξ and ζ of the tuned NC circuit the frequency dependence of the effective orthotropic Young's modulus of the MFC actuator could be performed. The computed frequency dependence of the Young's modulus in the frequency range from 10 Hz to 2 kHz is shown in Fig. 4.8, where real parts and the loss factors of the normalized effective Young's moduli are plotted for each Y_{11}, Y_{22} and Y_{33}. The red dotted line stands for the theoretical frequency dependence of Y_{11} calculated using Eqs. (4.21) and (4.30). It can be seen that the theoretical dependence acceptably corresponds to computed data.

Performed simulations show that it is possible to increase the effective Young's modulus Y_{11} by the factor of 1000 at the critical frequency (850 Hz), by the factor of 100 in a narrow frequency range around the critical frequency ($800 - 900$ Hz) and by the factor of 20 in a wider frequency range ($700 - 1000$ Hz). The Y_{22} component of the orthotropic Young's modulus was calculated to be increased by about 400 times at the critical frequency and about 20 times in a certain frequency range around the critical frequency ($780 - 910$ Hz). Since the value of Y_{33} is controlled by the different component of electromechanical coupling factor, the computations indicate a slight decrease in the whole range of frequencies for the particular adjustment of the NC circuit.

Finally, the graphical representation of the spatial distribution of the MFC actuator elastic displacement along the x axis is shown in Fig. 4.3.6. The effect of the connected and tuned NC circuit, where the piezoelectric deformation caused by the NC circuit acts against to the deformation according the Hooke's law, can be seen there. As a result, the MFC actuator is effectively stiffened.

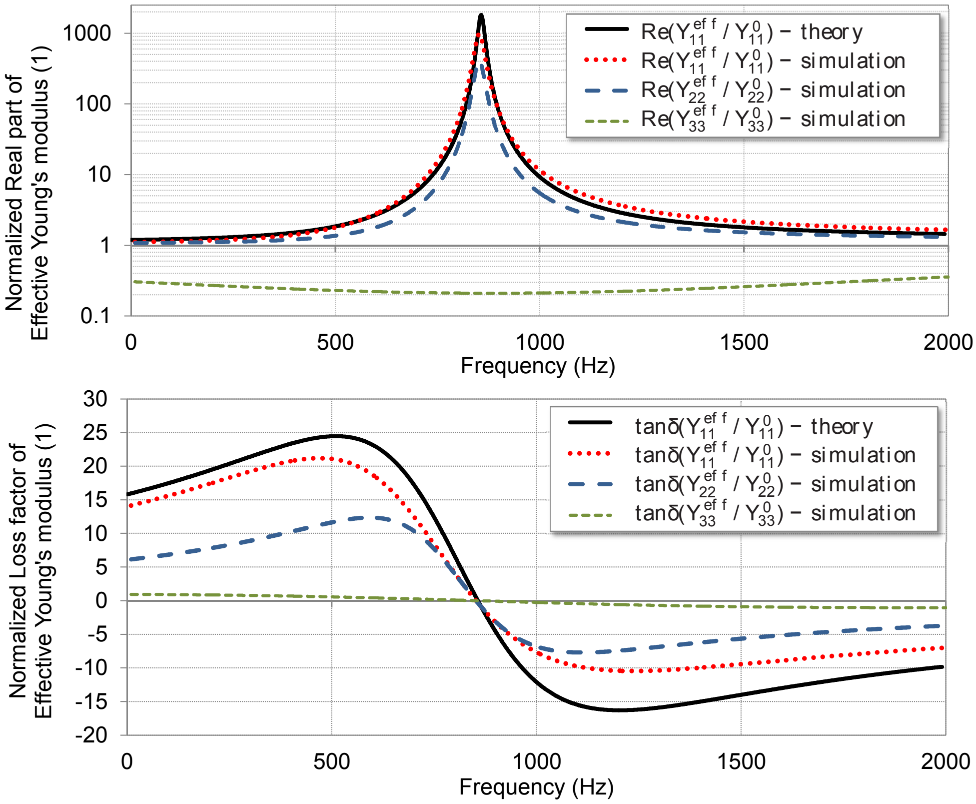

Figure 4.8: The real parts and loss factors of the normalized effective Young's moduli Y_{11} (thick solid), Y_{22} (thin solid), Y_{33} (dashed) and theoretical Y_{11} frequency dependence (dotted). It can be seen that the theoretical values acceptably correspond to our simulated data. It is possible to increase the effective Young's modulus Y_{11} by the factor 1000 at the one given frequency (850 Hz), by the factor 100 in a narrow frequency band around the given frequency (800 – 900 Hz) and by the factor 20 in a wider frequency range (700 – 1000 Hz). The second most dominant Young's modulus Y_{22} could be increased about 400times at the given frequency and about 20times in a certain frequency range around the given frequency (780 – 910 Hz). Since the value of Y_{33} is controlled by the different component of electromechanical coupling, for this kind of tuned NC circuit, it is slightly decreased in the whole range of frequencies.

4.4 Summary

Here, let us summarize the knowledge gained in this Chapter and point out the message, which is important to understand the topic discussed in next Chapter, i.e. the numerical model of the noise transmission suppression system, i.e. the glass plate with MFC actuators attached on its surface.

- A numerical model of the macro fiber composite (MFC) actuator based on the finite element method (FEM) has been developed here. The numerical model includes: (i) definition of the representative volume element (RVE) geometry of the MFC actuator (see Subsec. 4.2.1), (ii) formulation of the equations of motion and specification of numerical values of material parameters (see Subsec. 4.2.2), (iii) specification of the electrical and mechanical boundary conditions (see Subsec. 4.2.3), (iv) definition of state quantities averaging and the method of calculation of effective elastic and piezoelectric properties (see Subsec. 4.2.4), and (v) introduction of the electromechanical interaction of the MFC actuator with the external electric negative capacitance (NC) circuit and the implementation of the method of active elasticity control (AEC) on a simplified model of the MFC actuator where the movement only in the x direction is allowed (see Subsec. 4.2.5).

- The numerical model has been used for numerical computation of Young's moduli, shear moduli and Poisson's ratios of short-circuited MFC actuator (see Subsec. 4.3.1). There can be seen an acceptable agreement between the results of the numerical computations, the producer's values and with the values obtained by other computational methods. In a similar manner, macroscopic piezoelectric constants were computed from average strains in mechanically free MFC actuator with a given testing voltage on its electrodes (see Sec. 4.3.2). Again, an agreement between computed values and producer's data sheet values is appreciable. Finally, the capacitance per unit area of the MFC actuator was computed from the charge generated on the electrodes under the applied testing voltage (see Sec. 4.3.3). The computed value was compared to a roughly estimated value using the analytical formula for the in-parallel connection of two capacitors with different values of dielectric constant and to the producer's data sheet value.

- The effect of the electromechanical interaction of the MFC actuator and an external shunt circuit with a given capacitance was analyzed in Subsec. 4.3.4. It was roughly verified that the capacitance value of the shunt circuit controls only the values of the Young's moduli (Y_{11},

Y_{22}, Y_{33}). Values of shear moduli (G_{12}, G_{13}, G_{23}) are not influenced by the shunt circuit. The electromechanical coupling factors were calculated from the computed data using the method of least squares.

- In the next step of the analysis, the implementation of the negative impedance inverter (negative capacitor) was introduced in Subsec. 4.3.5. At first, several simulations were computed in order to determine the optimal adjustment of the NC circuit parameters that yield the maximum value of effective Young's modulus component Y_{11}. An increase in the effective Young's modulus Y_{11} by the factor of 1000 at the frequency 850 Hz was demonstrated. After that, the frequency dependence of macroscopic Young's moduli of MFC actuator shunted by the implemented NC circuit was measured. It was demonstrated that the value of effective Young's modulus Y_{11} can be increased by the factor of 100 in a narrow frequency range $800 - 900$ Hz and by the factor of 20 in a frequency range $700 - 1000$ Hz. The value of the Young's modulus component Y_{22} can be increased by about 400 times at the given frequency and by about 20 times in a frequency range $780 - 910$ Hz.

All in all, the macroscopic dielectric, elastic, and electromechanical properties of the MFC actuator under various electrical and mechanical boundary conditions were analyzed. It was demonstrated that it is possible to control the effective values of the Young's moduli to a large extent by connecting the MFC actuator to the NC circuit. Such an approach can be profitably used in systems for noise and vibration transmission suppression. The results of the frequency dependences of the Young's moduli can be used further in the FEM analysis, i.e. the glass plate with the MFC actuators attached, each with the computed effective elastic properties.

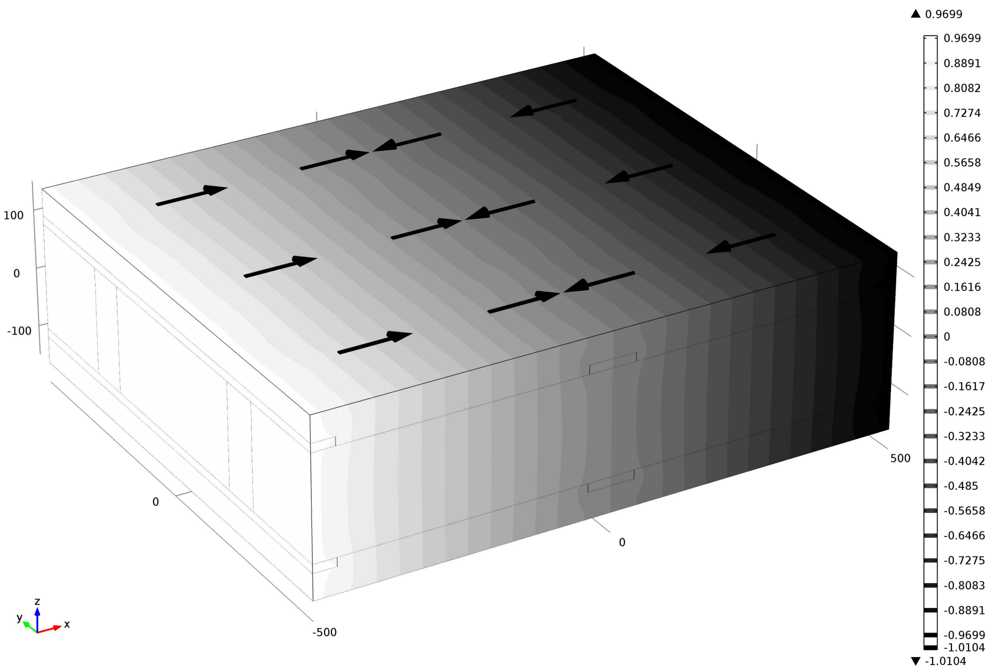

(a)

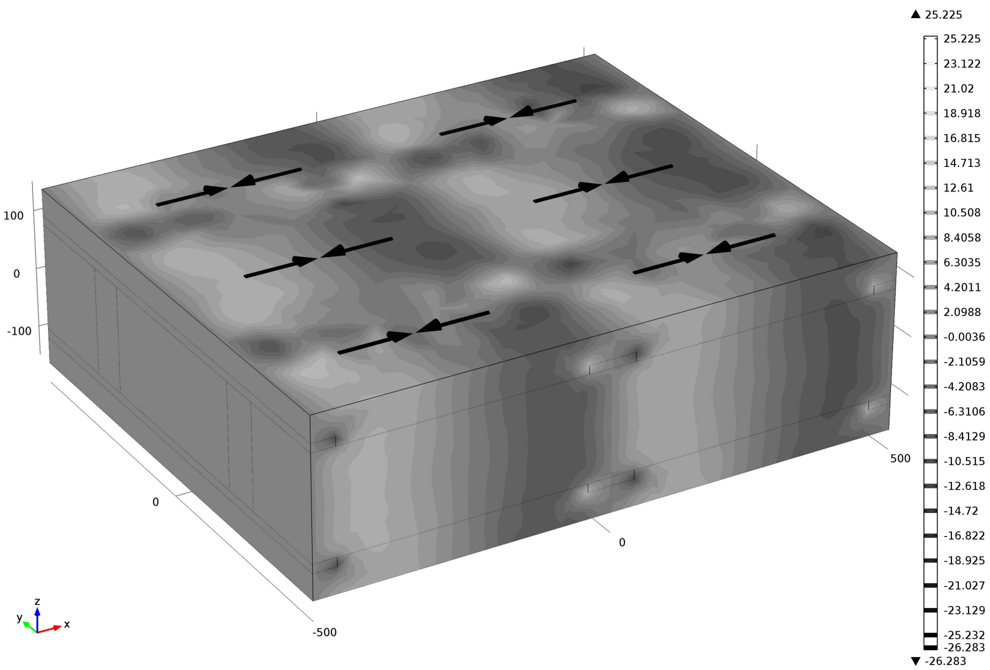

(b)

Figure 4.9: Spatial distribution of the elastic displacement of the MFC actuator along the x axis, the gray-scale legend indicates the displacement values in μm, (a) displacement in the MFC actuator disconnected from the NC circuit, (b) The effect of the connected and tuned NC circuit, where the piezoelectric deformation caused by the NC circuit compensates the deformation according the Hooke's law. As a result, the MFC actuator is effectively stiffened.

Chapter 5

Glass plate noise transmission suppression by means of distributed MFC actuators shunted by the negative capacitance circuit

Using the theoretical formula for the acoustic transmission loss calculated in Chap. 2, using the principles of the active elasticity control (AEC) method introduced in Chap. 3, and using the numerical results of the actively controlled Young's modulus of the macro fiber composite (MFC) actuator obtained in previous Chap. 4, the possibility of increasing the acoustic transmission loss of sound transmitted through planar or curved glass plates using attached piezoelectric MFC actuators shunted by the NC circuits is analyzed here.

The objective of the study presented in this Chapter is to analyze the most efficient ways for suppression of noise transmission through the glass plates using active elasticity control of attached piezoelectric elements. The key features that control the sound transmission through the curved glass shells using an analytical approximative model have been previously analyzed in Chap. 3 and also presented the key aspects of the application of the AEC method to the noise transmission suppression through composite structures with piezoelectric layers. Here, in order to verify the applicability of the APSD method to the noise transmission suppression through the glass plates, the finite element method (FEM) simulations of the sound transmission through the glass plate with that attached piezoelectric elements shunted with negative capacitance circuits are used. The detailed analysis of the FEM model implementation of the particular arrangement of MFC actuators on the glass plate is performed in Sec. 5.1. Besides other

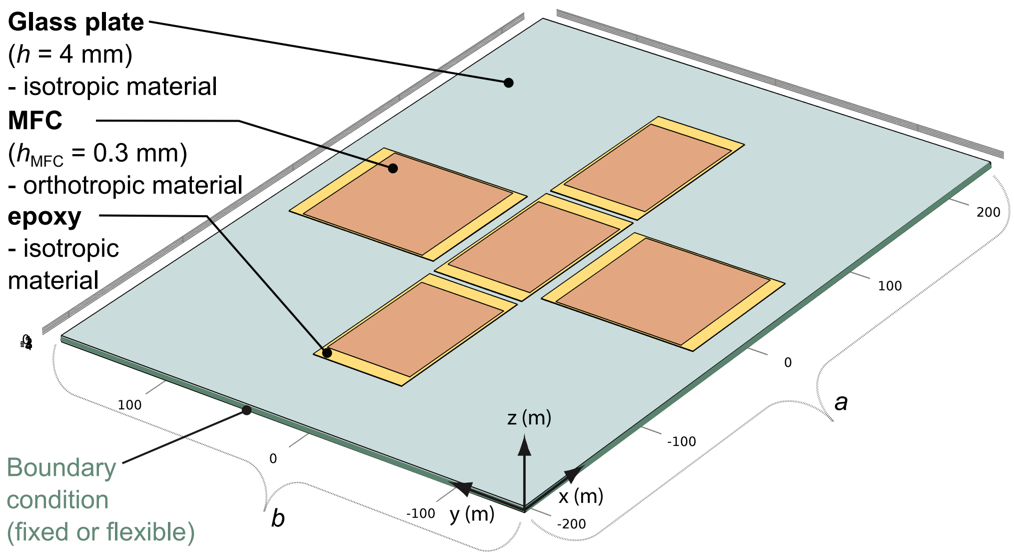

Figure 5.1: Geometry of the finite element method (FEM) model of a plane or curved glass plate of thickness h and dimensions a and b with 5 attached macro fiber composite (MFC) actuators. The presented configuration is selected in order to allow the suppression of majority of low-frequency vibrational modes. The considered coordinate system and boundary conditions are indicated.

things, the FEM model takes into account the effect of a flexible frame that clamps the glass plate at its edges. Sec. 5.2 describes a simple experimental setup for the approximative measurements of the acoustic transmission loss. Results of the FEM model simulations and their comparison with experimental data are presented in Sec. 5.3. Finally, numerical simulations and experimental results are discussed and summarized in Sec. 5.4.

5.1 FEM model of the glass plate with attached MFC actuators

In order to analyze the noise transmission through the glass plate with attached MFC actuators it is convenient to develop a realistic FEM model which would be robust enough to see all the aspects of the vibrational response of the plate to the incoming pressure wave. So, in this Section, a detailed description of the particular arrangement of MFC actuators on the glass plate is and presented.

5.1.1 Geometry of the FEM model

Figure 5.1 shows the geometry of the FEM model of a planar or curved glass plate of thickness h and dimensions a and b with 5 attached MFC actuators, placed in the system of coordinates. It the case of the curved geometry it is considered a glass plate, which could be fabricated by thermal bulging of the originally planar glass plate. The presented configuration of MFC actuators is selected in order to allow the suppression of majority of low-frequency vibrational modes. The shapes of the vibrational modes follow.

5.1.2 Modal analysis of the glass plate with attached MFC actuators

Knowledge of the panel natural frequencies and mode shapes is extremely helpful. It allows to predict at which frequency the plate's vibration will be more significant and, therefore, when the plate will transmit more acoustic power to the other side. Knowledge of the mode shape is useful, because it provides a guidance for stiffening the composite structure in order to change its natural frequencies or to decrease the vibrational amplitude at the specific critical place of the structure.

A plate is an example of a continuous system, which has an infinite number of mode shapes and natural frequencies. The free harmonic vibration of a thin plate with constant thickness h is governed by the commonly known differential equation:

$$G\,\Delta^2 w(x,y) - \omega^2 \rho h w(x,y) = 0, \tag{5.1}$$

where $w(x,y)$ is a typical vibrational mode.

For complicated geometries, such as the flexible plate with attached piezoelectric actuators, discretized numerical solutions, such as FEM models, are commonly used. Before the FEM modal analysis could be performed, boundary conditions have to be treated. Lets take the simplest case of the plate with clamped edge:

$$w(x,y) = 0 \tag{5.2a}$$

$$\frac{\partial w(x,y)}{\partial n} = 0, \tag{5.2b}$$

where n is the normal directional component from the clamped boundary edge. The clamped edge boundary condition is satisfied at the surfaces with coordinates: $x = -a/2$, $x = a/2$, $y = -b/2$ and $y = b/2$.

The first 12 vibrational mode shapes of (i) the clamped glass plate with attached MFC actuators are illustrated in Fig. 5.2 and (ii) the glass plate with attached MFC actuators with added mass of the clamped steel frame are illustrated in Fig. 5.3. The frequency range is limited to 2000 Hz. The modes could be numbered according to how many half sine waves are found in each direction. Hence, the $(3, 1)$ mode would have three half sine waves in the x-direction and one half sine wave in the y-direction. This particular mode of frequency 850 Hz was chosen to illustrate the function of the MFC actuators shunted by the NC circuit attached to the glass plate which is exposed to the acoustic pressure. In the case of the steel frame, added as a additional solid domain, this particular mode is shifted to the value of 746 Hz.

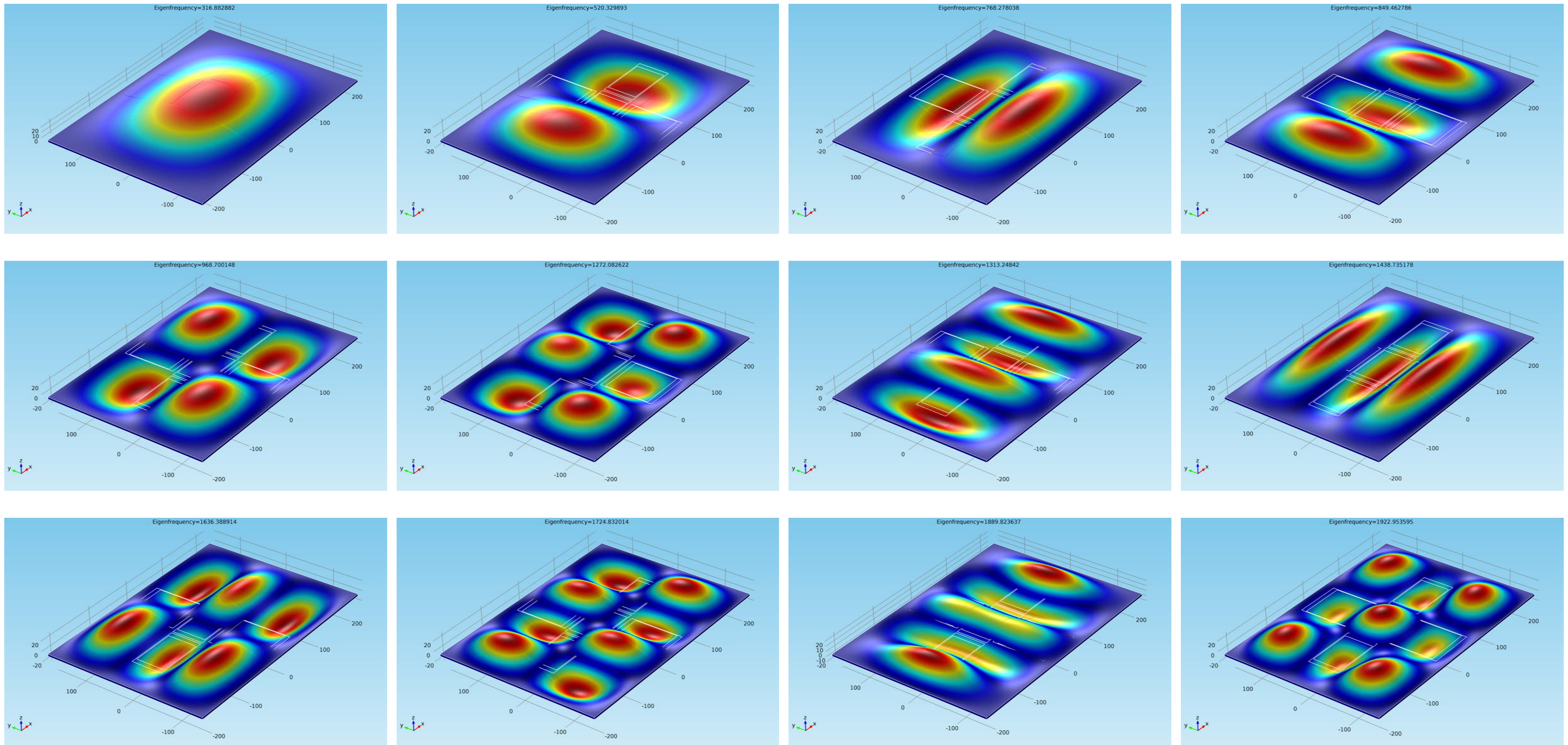

Figure 5.2: Vibrational modes of the glass plate with attached MFC actuators. The frequency range is limited to 2000 Hz.

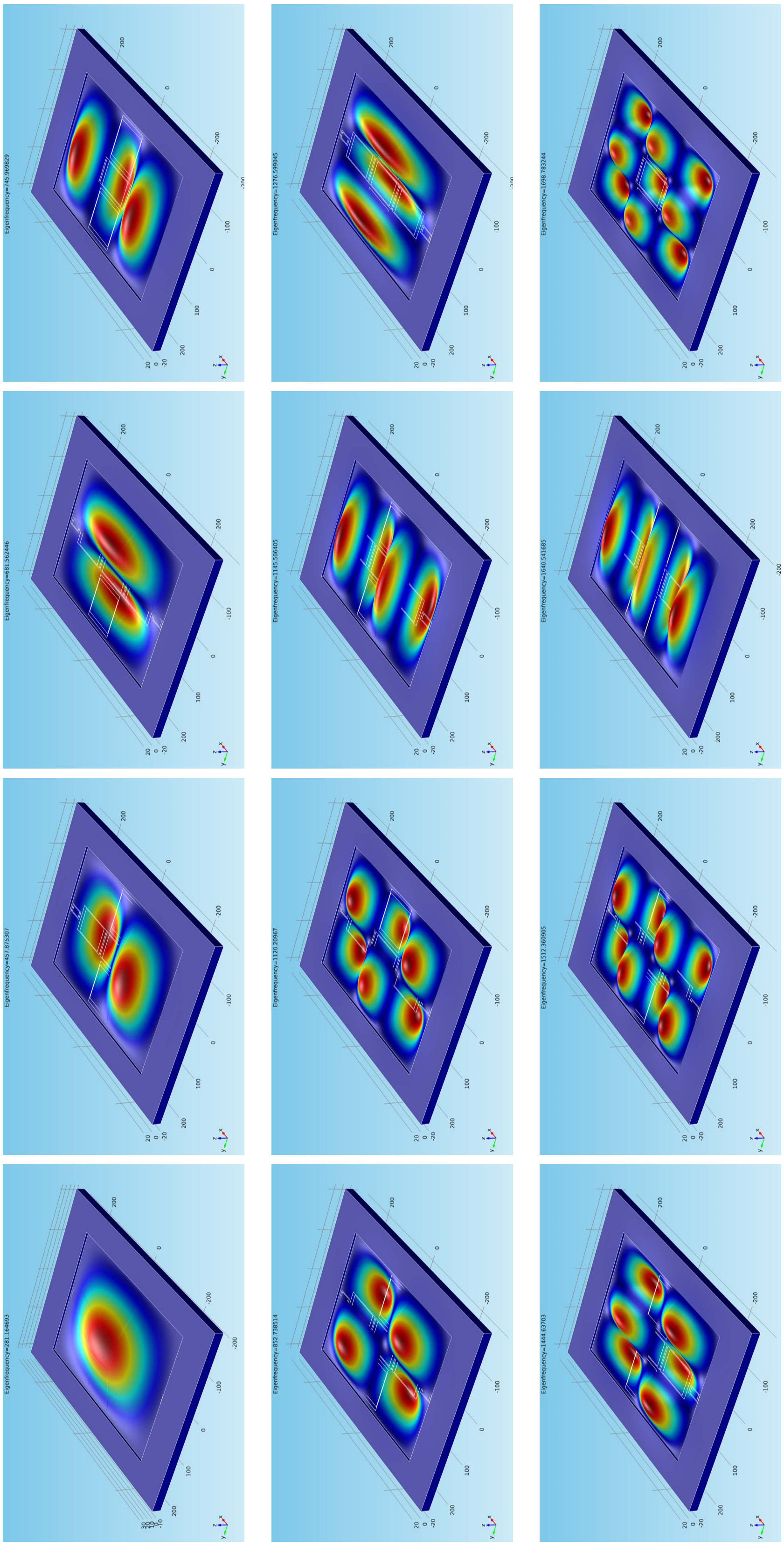

Figure 5.3: Vibrational modes of the glass plate with attached MFC actuators with added mass of a steel frame. The frequency range is limited to 2000 Hz.

5.1.3 Coupled system of the flexible plate and piezoelectric MFC actuator

It is convenient to perform the coupled analysis of the piezoelectric domain of the MFC actuator with the linear solid domain of the glass plate to verify the actuation function of the MFC actuators on the glass plate. Basically, it is the same type of analysis as it was introduced in the previous Chapter when the piezoelectric domain of the PZT fibers was coupled with an epoxy and polyimide material representing the linear elastic solid domain. Therefore, to check the governing equations, the reader is referred to the Sec. 4.2.2 to see the Eqs. (4.3)-(4.9). Here, the piezoelectric domains are the macroscopic plates of the thickness h_{MFC} representing the active part of MFC actuators and, the linear elastic domains are the glass plate with an epoxy embedding the active part of MFC actuators.

In the case of static analysis, a direct testing voltage is applied to the top electrode of the MFC actuator and the angular frequency is equal to zero, i.e. $\omega = 0$ and, in the case of dynamic analysis, a harmonic voltage of angular frequency $\omega = 2\pi f$ is applied to the top electrode of the MFC actuator, where the frequency f ranges from 10 Hz to 2 MHz. In both analyses, the bottom electrode is supposed to be grounded, i.e. the electric potential $V = 0$ V.

Just like in the modal analysis, in the same manner the external boundary conditions are introduced, i.e. the clamped glass plate or the clamped steel frame for the static or dynamic analysis, respectively.

5.1.4 Coupled system of the flexible plate with attached MFC actuators and acoustic media

In the case of a coupled system of the flexible planar structure and the acoustic media, the effect of the flexible glass plate on the sound field below and above the plate as well as the effect of sound field on the flexible glass plate must be considered together. First, the governing equation for each type of physics and second, the coupling variables should be introduced, respectively.

5.1.4.1 Governing equations

The vibrational response of the curved glass plate expressed by the displacement vector u_i is governed by the equations of motion on the form:

$$2\varrho \frac{\partial^2 u_i}{\partial t^2} - \nabla_j \left[c_{ijkl} \left(\nabla_k u_l + \nabla_l u_k \right) \right] = 0, \tag{5.3}$$

where ϱ is the mass density of glass, c_{ijkl} are the components of elastic stiffness tensor, and $\nabla_i = \partial/\partial x_i$ is the i-th component of the gradient operator. Since we are interested in the steady-state vibrational response of the plane/curved glass plate, we consider the harmonic time dependence of the displacement vector, i.e. $u_i(x, y, z, t) = u_i(x, y, z)\, e^{i\omega t}$, and the equations of motion Eq. (5.3) can be written in the form:

$$2\omega^2 \varrho\, u_i + \nabla_j \left[c_{ijkl} \left(\nabla_k u_l + \nabla_l u_k\right)\right] = 0, \tag{5.4}$$

In this study, the same governing equations can be also applied to describe the vibrational response of the MFC actuators. Justification for such a simplification is as follows. Since the MFC actuator consists of many thin piezoelectric fibers embedded in an epoxy matrix, connected to interdigital electrodes, and laminated in thin polyimide layers, one can expect that detailed vibration of such a complicated composite structure is difficult to model in full detail together with the macroscopic structure of the glass plate. On the other hand, the MFC actuator of P2-type operates as d_{31}-type piezoelectric actuator with some macroscopic values of piezoelectric coefficients (see Chap. 4, Sec. 4.2.4).

In the same manner, one can introduce the effect of the shunt circuit, however, with the frequency dependent values of the components of elastic stiffness tensor of the MFC actuator. As it follows from the Eq. (3.33) and as it has been written previously in Chap. 3, the effective value of Young's modulus of the shunted piezoelectric actuator is a function of the ratio of the shunt capacitance C over the static capacitance C_S of the piezoelectric actuator. Since the capacitance of the negative capacitor is frequency-dependent, as it is seen in Eq. (4.26), written in Chap. 4, the matching of capacitances C and C_S according to the condition expressed by Eq. (3.34) required for obtaining large effective values of Young's modulus can be obtained only in a relatively narrow frequency range due to virtually constant value of the capacitance C_S.

The frequency dependence of the effective Young's modulus of the MFC actuator shunted by the negative capacitor was briefly analyzed in the recent work by Nováková and Mokrý [A.3] and analyzed in full detail in recently submitted article by Nováková and Mokrý [A.10]. Fig. 4.8 shows the computed frequency dependence of the real parts and the loss factors of the normalized effective Young's moduli of the MFC actuator in a broad frequency range (see Chap. 4, Sec. 4.3.6). The frequency 850 Hz of the peak values of the real part of Young's moduli Y_{11} and Y_{22} is adjusted to the frequency of a particular resonant mode of the glass plate via the particular values of the circuit parameters of the negative capacitor (see Chap. 4, Sec. 4.3.5). Performed simulations show that the Young's modulus of the MFC actuator shunted by the NC circuit is strongly frequency dependent. In addition, each component of the orthotropic Young's modulus has a different frequency dependence for the particular adjustment of the NC

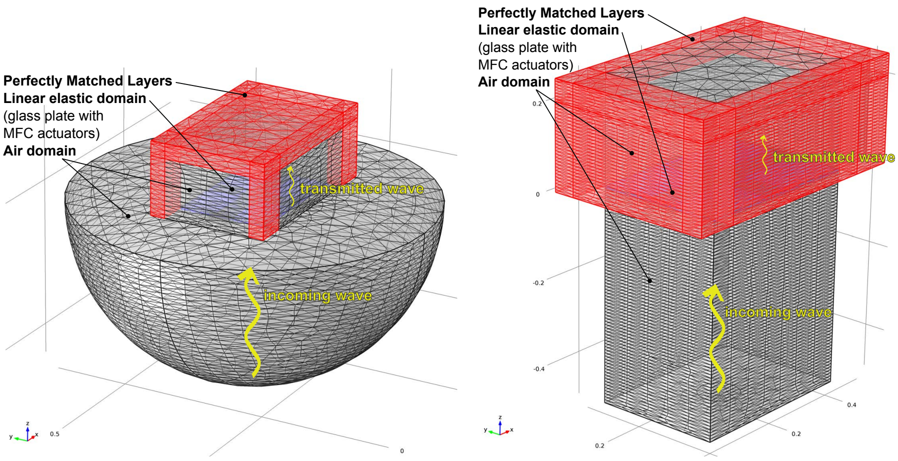

(a) (b)

Figure 5.4: Geometry and mesh of the considered linear elastic and air domains in the FEM model; (a) The incoming wave, which strikes the plate, goes from infinity; (b) The acoustic wave has a source in the bottom of the acoustic box.

circuit. Of course, it is possible to adjust the NC circuit at a different frequency, so, the peak of the macroscopic Young's modulus frequency dependence of the MFC actuator would be shifted.

Further, we consider that the glass plate with MFC actuators interacts with the acoustic field in the air above and below the plate. Fig. 5.4 sketches the acoustic air domains surrounding the linear elastic domain of the glass plate. Two different cases are considered. First, the incoming wave, which strikes the plate, goes from infinity (Fig. 5.4(a)), second, the acoustic wave has a source in the bottom of the acoustic box which is supposed to simulate the real situation of the experiment performed to verify the simulations Fig. 5.4(b). In both analyses we consider a sound source that produces a plane incident wave below the glass plate:

$$p_i(z,t) = P_i\, e^{i(\omega t - kz)}, \tag{5.5}$$

where k is the wave number of the incident sound wave, which is oriented along the z-axis. The acoustic pressure p distribution in the air above and below the glass plate is governed by the following equation:

$$\frac{1}{\rho_0 c^2}\frac{\partial^2 p}{\partial t^2} + \nabla_i\left(-\frac{1}{\rho_0}\nabla_i p\right) = 0, \tag{5.6}$$

where ϱ_0 and c stand for the mass density and the sound speed in the air. Again, we are interested in the steady-state distribution of the acoustic pressure, i.e. $p(x, y, z, t) = p(x, y, z)\, e^{i\omega t}$, and the equation above reduces down to the form:

$$-\frac{\omega^2 p}{\rho_0 c^2} + \nabla_i \left(-\frac{1}{\rho_0} \nabla_i p \right) = 0. \tag{5.7}$$

It should be noted that below the glass plate the acoustic pressure is given by the sum of the acoustic pressures of the incident and reflected sound waves, i.e. $p = p_i + p_r$. Above the glass plate, the acoustic pressure is equal to the acoustic pressure of the transmitted sound wave, i.e. $p = p_t$. That means that the waves propagate into an unbounded domain. In simulations, such a situation can be easily numerically simulated using the method of perfectly matched layers (PMLs) [137]. Usually, in many scattering and waveguide-modeling problems, it is not possible to describe the wave radiation as a plane wave with a well-known direction of propagation. In such situations, one should consider the implementation of PMLs into a numerical FEM model. A PML is strictly speaking not a boundary condition but an additional air domain that absorbs the wave radiation without producing reflections. It provides good performance for a wide range of incidence angles and it is not particularly sensitive to the shape of the wave fronts. It is implemented as a coordinate stretching following the coordinate transformation inside the PML domain as introduced in [138]:

$$\xi' = \mathtt{sign}(\xi - \xi_0)\, |\xi - \xi_0|^n \, \frac{L}{\delta \xi^n} (1 - i), \tag{5.8}$$

where ξ is the coordinate direction in which the PML absorbs the acoustic waves, ξ_0 is the coordinate of the inner PML boundary and $L/\delta\xi^n$ is the scaling factor, where L is one wavelength. Basically, the PML region should be designed to model uniform regions extended towards infinity. See Fig. 5.4 to check where the PMLs are located. They are sketched by the red domains surrounding the area of the transmitted acoustic waves.

5.1.4.2 Internal and external boundary conditions

The calculation of acoustic transmission loss is based on analysis of the interaction between the vibrating glass plate and the surrounding air. In order to proceed the calculation, the system of partial differential equations Eqs. (5.4) and (5.7) should be appended by the system of boundary and internal boundary conditions: First, the acoustic pressure exerts the force on the glass plate at its interface with the air, which can be expressed by the following internal boundary condition:

$$n_j \left[c_{ijkl} \left(\nabla_k u_l + \nabla_l u_k \right) \right] = 2 n_i p, \tag{5.9}$$

where n_i is the i-th component of the outward-pointing (seen from the inside of the glass plate) unit vector normal to the surface of the glass plate with the MFC actuators. Second, the normal accelerations of the glass surface and the air particles are equal at the interfaces of the glass plate and the air:

$$\omega^2 \, (n_i u_i) = n_i \, (1/\varrho_0) \, \nabla_i p. \tag{5.10}$$

Finally, a special attention must be paid to the external boundary conditions for the displacement u_i at the edges, where the glass plate is clamped at the frame. In the most of the FEM simulations results presented in Thesis below, just like in the modal analysis, the ideally fixed frame is considered (Eq. (5.2)). However, in many real situations, the glass plate is not ideally fixed and the frame that clamps the glass plate is somehow flexible. In order to take this effect into account, the boundary condition was approximated by considering a reaction force $\mathbf{f}_{\rm fr}$ from the spring system of the frame as being proportional to the frontal displacement of the glass plate with respect to the frame, i.e. $\mathbf{f}_{\rm fr} = -k_{\rm fr}\mathbf{u}$, where the symbol $k_{\rm fr}$ stands for the effective spring constant of the frame, which can be estimated from geometrical parameters and Young's moduli of the frame. This yields the following boundary conditions:

$$\begin{aligned} f_1 = c_{11kl} \left(\nabla_k u_l + \nabla_l u_k \right) &= -k_{\rm fr} \, u_1, && (5.11a) \\ u_2 &= 0, && (5.11b) \\ u_3 &= 0 && (5.11c) \end{aligned}$$

on the glass edges where $x = -a/2$ and $x = a/2$ and

$$\begin{aligned} u_1 &= 0, && (5.12a) \\ f_2 = c_{22kl} \left(\nabla_k u_l + \nabla_l u_k \right) &= -k_{\rm fr} \, u_2, && (5.12b) \\ u_3 &= 0 && (5.12c) \end{aligned}$$

for $y = -b/2$ and $y = b/2$. It should be noted that the boundary conditions given by Eqs. (5.11) and (5.12) express the limited ability of the frame to keep the glass plate edge at the same position during the vibration movements. As a result, the glass plate movements acquire some properties typical for membranes, which yield the shift of the resonant frequencies to lower values.

5.1.4.3 Acoustic transmission loss calculation

The boundary problem for partial differential equations given by Eqs. (5.4), (5.7)-(5.12) was solved using COMSOL Multiphysics software. The solution yields spatial distributions of the acoustic pressure p and the glass plate displacements u_i. Then, the specific acoustic impedance of the glass plate Z_w was estimated for every frequency ω of the incident sound wave using the following approximative formula:

$$Z_w(\omega) \approx \frac{\Delta P(\omega)}{i\omega W(\omega)}, \tag{5.13}$$

where ΔP is the amplitude of the acoustic pressure difference above and below the middle point of the glass plate, W is the amplitude of the normal displacement at the middle point of the glass plate. The acoustic TL was obtained using Eq. (2.27).

5.1.4.4 Material properties

The governing equations should be appended by the numerical values of the material parameter and input variables. Isotropic material constants for the glass and air domains, which are required for the coupled analysis are listed in Table 5.1 together with geometrical parameters. The value of acoustic pressure of the sound source is also included as a sound pressure level (SPL), which is defined by the formula:

$$\mathtt{SPL} = 20 \log_{10} \left(\frac{p}{p_{ref}} \right), \tag{5.14}$$

where $p_{ref} = 20\ \mu$Pa is the reference sound pressure. Material parameters of the orthotropic MFC actuator are computed using the developed FEM model presented in previous Chapter. The effective values are listed in Table 4.4. These parameters are suitable for the acoustic-structural analysis without the influence of the NC circuit. When the NC circuit is connected to the MFC actuators, the effect of the negative capacitance is introduced as a frequency dependent orthotropic Young's modulus according to the Fig. 4.8.

Numerical predictions of the FEM models should be compared with experimental data. The next Section presents a simple setup for obtaining experimental data.

5.2 Experimental setup for the FEM model verification

In this Section, a brief description of two different experimental setups that were used for the verification of FEM model predictions will be given. First, the measurement of the surface displacement of the glass plate using the digital holographic interferometry (DHI) method and, second, the approximative acoustic measurements of the acoustic transmission loss.

Material/Geometrical parameter	glass	steel	air	unit
Young's modulus	$70 \cdot 10^9$	$205 \cdot 10^9$	-	Pa
Poisson's ratio	0.20	0.28	-	1
Density	2400	7850	1.2	kg$\cdot$ m^{-3}
Speed of sound	-	-	343.2	m$\cdot$ s^{-1}
SPL of the sound source	-	-	80	dB
Dimension a of the plate	0.42	-	-	m
Dimension b of the plate	0.30	-	-	m
Thickness h of the glass	0.004	-	-	m
Dimension of the frame along x	-	0.60	-	m
Dimension of the frame along y	-	0.42	-	m
Thickness of the frame	-	0.02	-	m
Spring constant k_{fr} of the steel frame implemented as a BC	$1 \cdot 10^{10}$	-	-	N$\cdot$m^{-1}
Spring constant k_{fr} of the wooden frame implemented as a BC	$1 \cdot 10^7$	-	-	N$\cdot$m^{-1}

Table 5.1: Material and geometrical parameters used in coupled analysis of interaction of the glass plate with an acoustic fluid. Material parameters of the glass are commonly used values for the flat glass in practice (see e.g. [139, 140]).

5.2.1 Digital holographic interferometry method for the surface displacement measurement

The predictions of the numerical FEM simulations were verified by the digital holographic interferometry (DHI) measurements performed by the research group under the supervision of Dr. Vít Lédl, a specialist in optics and optical measurements.

DHI method is a possible way how to detect the distribution of surface vibration displacement of the planar structure. Fig. 5.5(a) shows a scheme of the setup for the measurement of the surface displacement distribution of the glass plate placed on the acoustic box.

The laser beam of the wavelength of 532 nm and the power of 100 mW is split into two beams by the polarizing beam splitter 1, which is equipped with half wavelength retardation plates. Half wavelength retardation plates help set the intensities in both beams as well as the polarization of each beam. Both beams are then spatially filtered and collimated. The second beam acting as a reference wave can be further attenuated if necessary by a set of gray filters placed in filter wheels. The object beam, the first beam, illuminates the sample – the glass plate – and the light scattered from its

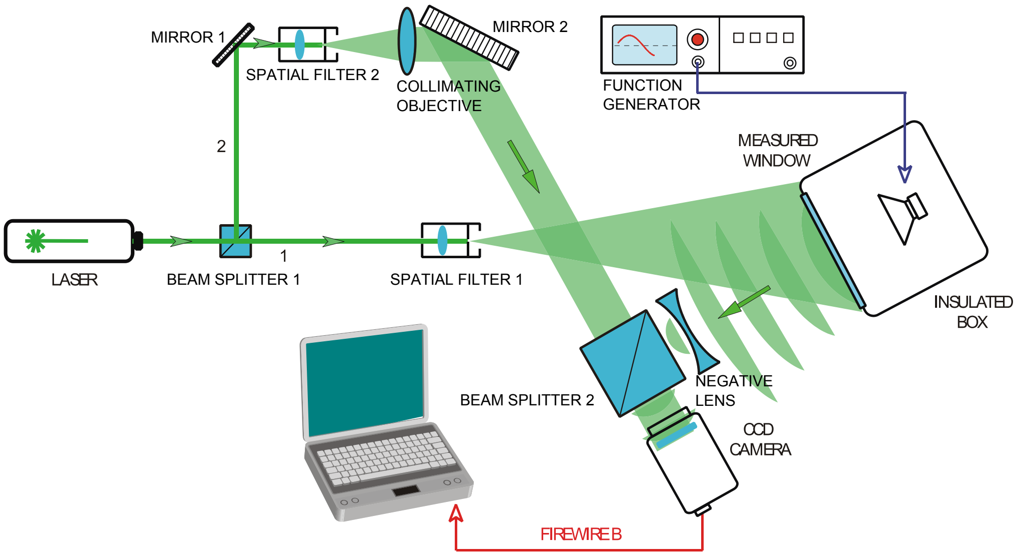

(a)

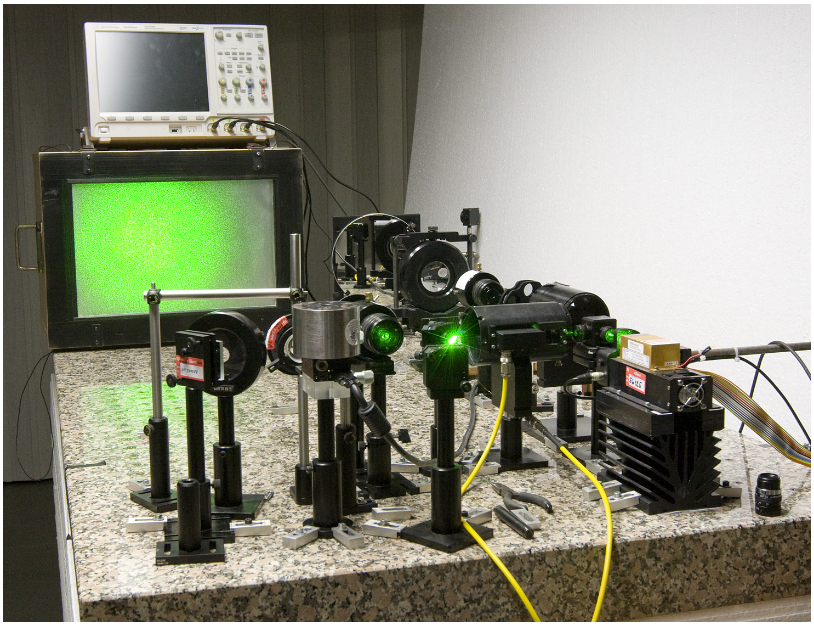

(b)

Figure 5.5: Digital holographic interferometry (DHI) measurement setup and realization; (a) Scheme of the glass plate surface displacement measurement using the DHI method. The laser beam is split into two beams by the polarizing beam splitter 1 which is equipped with half wavelength retardation plates. Both beams are then spatially filtered and collimated. The object beam, the first beam, illuminates the glass plate and the light scattered from its surface impinges on the beam splitter 2, where the reference and the object waves are recombined. The both waves interfere and a digital hologram is captured. The CCD camera is connected to the computer via a fire wire B interface; (b) The photograph of a realization of the experimental setup of the glass plate surface displacement distribution measurement using the DHI method.

surface impinges on the beam splitter 2, where the reference and the object waves are recombined. The both waves interfere and a digital hologram is captured. The angle between the beams is set to be approximately 3 degrees. The CCD camera has a resolution of 2049 $\times$ 2056 pixels, each pixel having the size of 3.45 $\times$ 3.45 μm. The camera is connected to the computer via a fire wire B interface enabling a frame rate of 6.5 FPS.

The realization of the experimental setup of the glass plate surface displacement distribution measurement using the DHI method could be seen in Fig. 5.5(b). The glass plate is fixed in a wooden frame and placed on the acoustic box. Inside the acoustic box, the loudspeaker is used as a sound source. The acoustic waves generated by the loudspeaker strike the window plate making it vibrate. Using the DHI method, first, mode shapes of the glass plate are measured, and second, the static displacement of the glass plate with two attached MFC actuators connected to the direct voltage source is measured.

5.2.2 Approximative acoustic measurements of the acoustic transmission loss

Figure 5.6 shows the experimental setup for the approximative measurements of the specific acoustic impedance. The glass plate is clamped in a wooden or steel frame of the inner dimensions $a \times b$. This structure forms a lid of the soundproof box with a loudspeaker that produces the source of the incident sound wave. According to the scheme in Fig. 5.6(a), the microphone IN inside the box and the microphone OUT out of the wooden box measures the difference of acoustic pressures amplitudes ΔP at the opposite sides of the glass plate. They are placed approximately 1 cm above and below the middle point of the glass plate. Laser Doppler vibrometer measures the amplitude of the vibration velocity V of the glass plate middle point. The specific acoustic impedance Z_w is then approximated by the ratio $\Delta P/V$ and the value of the acoustic TL is estimated using Eq. (2.27).

The realization of the experimental setup of the TL measurement could be seen in Fig. 5.6(b). The NC circuit is connected to the MFC actuators. Both cases, when the NC circuit is turned on and off, are measured.

Using such a measurement setup, only an approximative value of the TL can be obtained because of limited dimensions of the box. However, it is acceptable for the demonstration of the noise suppression efficiency. The acoustic transmission loss was measured for two cases, (i) when the MFC actuators are not connected to the NC circuit and (ii) when MFC actuators are shunted by the NC circuit. The next section presents the numerical results of our FEM model simulations and their comparison with the approximative experimental data.

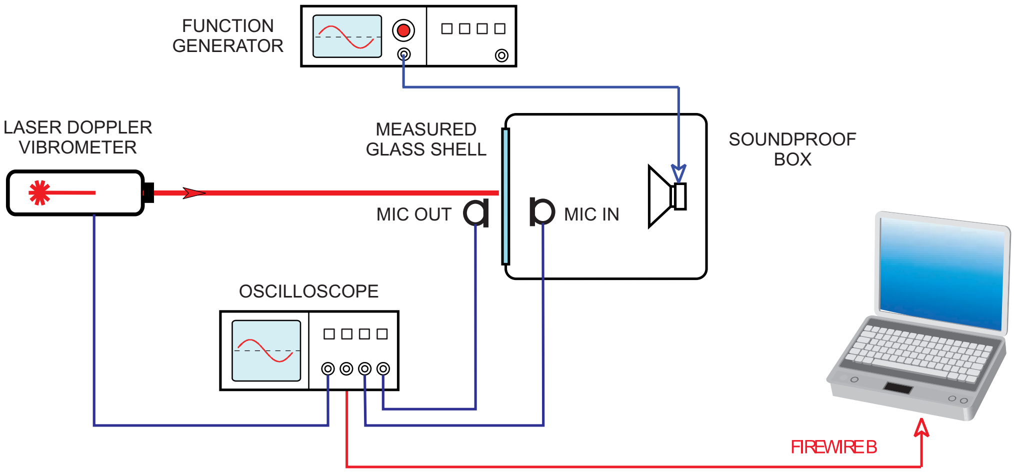

(a)

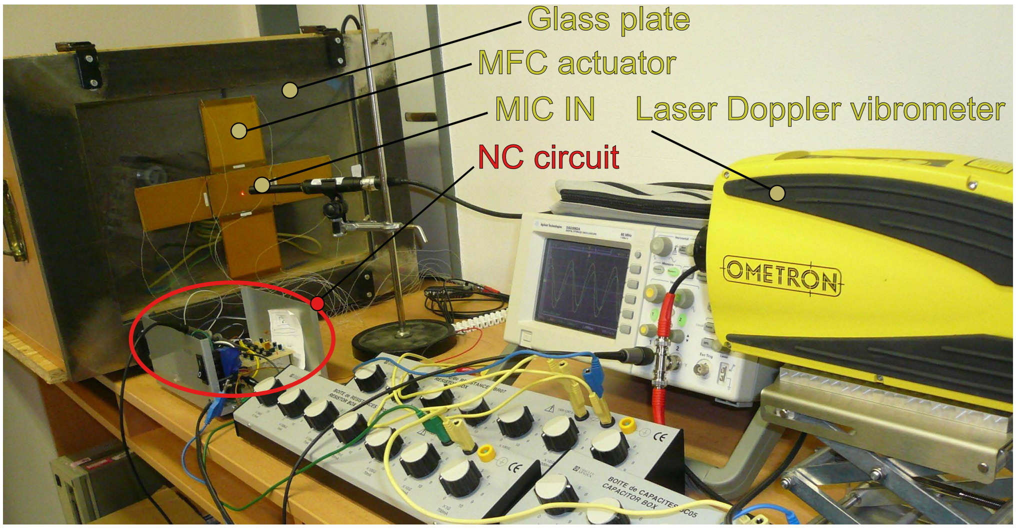

(b)

Figure 5.6: Experimental setup for the approximative measurements of the specific acoustic impedance; (a) Scheme of the measurement, when the glass plate is placed on the top of the soundproof box with a loudspeaker that produces the source of the incident sound wave. The microphone IN inside the box and the microphone OUT out of the wooden box measures the difference of acoustic pressures amplitudes ΔP at the opposite sides of the glass plate. They are placed approximately 1 cm above and below the middle point of the glass plate. Laser Doppler vibrometer measures the amplitude of the vibration velocity V of the glass plate middle point. The specific acoustic impedance Z_w is then approximated by the ratio $\Delta P/V$; (b) The photograph of a realization of the experimental setup of the approximative measurements of the specific acoustic impedance. The NC circuit is connected to the MFC actuators. Both cases, when the NC circuit is turned on and off, are measured.

5.3 Results of the FEM model simulations and the experimental verification

At first, results of FEM model simulations and DHI measurements of the surface displacement distribution will be presented. Second, the results of FEM model simulations and approximative measurements of the acoustic transmission loss frequency dependences will be shown appended by the graphical representations of the acoustic pressure distribution at the treated glass plate resonant mode.

5.3.1 Coupled system of the glass plate and piezoelectric MFC actuator – static and dynamic response on electric voltage

Fig. 5.7 shows the static bending of the glass plate when the direct voltage of 300 V was applied on the electrodes of the MFC actuators. For this particular measurement a configuration setup with two MFC actuators was used. A photograph of the measured glass window with the MFC actuators clamped in a wooden frame could be seen in Fig. 5.7(a), the picture of the surface displacement of the glass plate captured by the DHI method is in Fig. 5.7(b) and last, for the result of FEM simulation of the glass plate displacement distribution stands Fig. 5.7(c). The white arrows locate the places where the MFC actuators were attached. It is evident that an acceptable agreement between the experimental values and the FEM simulations could be observed.

The dynamic response of the coupled system with attached MFC actuators on the harmonic voltage of the amplitude of 1 V could be seen in Fig. 5.8. The vibrations amplitude was measured in the middle point of the glass plate. The frequency range is limited from 10 Hz to 2 kHz. The experiment data (blue solid) are compared with the FEM model ones (red dashed). In the FEM model, the geometry with the steel frame which is put into the model as a additional mass is used. At the low frequency modes the acceptable agreement between the experiment and the FEM model is observed. On the other hand, at modes ensuing after 1 kHz value, the frequency dependence is shifted. One of the reason for this discrepancy could be the fact that in real situation of the experiment the steel frame is not ideally fixed. At higher frequencies the mass density and the Young's modulus of the glass are not the only dominant parameters which affect the resonant frequencies. It would be desirable to perform some additional FEM simulations to see how the boundary conditions of the frame affect the frequency dependence of the vibration amplitude of the glass plate, especially at the higher frequencies.

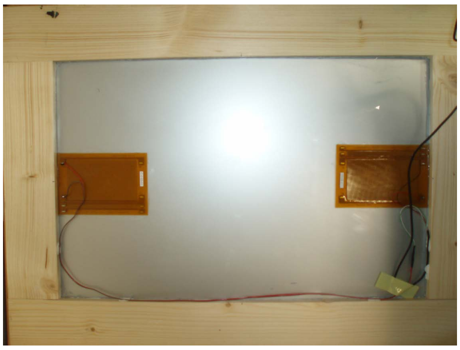

(a)

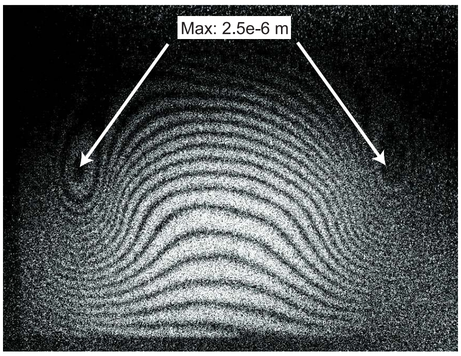

(b)

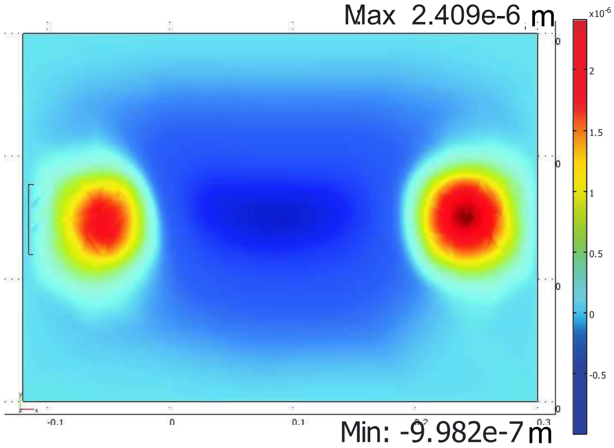

(c)

Figure 5.7: Static bending of the glass plate due to the action of electrical voltage. DHI experiment with FEM model analysis comparison; (a) A photograph of the measured glass window with the MFC actuators clamped in a wooden frame; (b) Surface displacement distribution of the glass plate measured by the DHI method. The white arrows locate the places where the MFC actuators were attached and point out the value of the maximal displacement; (c) The result of FEM simulation of the glass plate displacement distribution. It is evident that an acceptable agreement between the experimental values and the FEM simulations could be observed.

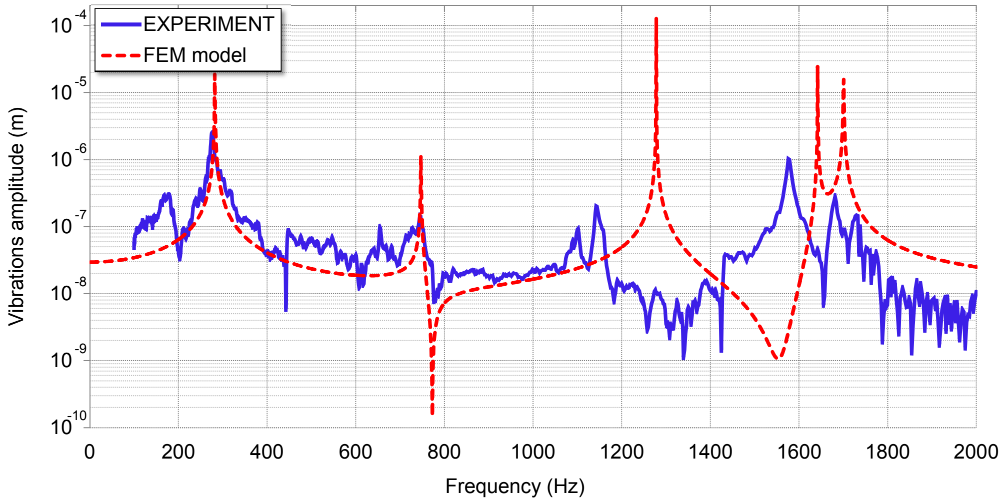

Figure 5.8: Dynamic response of the coupled system with attached MFC actuators on the harmonic voltage of the amplitude of 1 V. The vibrations amplitude was measured in the middle point of the glass plate. The experiment data (blue solid) are compared with the FEM model ones (red dashed). At the low frequency modes the acceptable agreement between the experiment and the FEM model is observed.

5.3.2 Coupled system of the glass plate with attached MFC actuators and acoustic media

Here, the results of the computed and measured acoustic transmission loss will be presented. First, the influence of the flexible boundary conditions of the simple glass plate on the acoustic TL in comparison with experimental data will be shown. Then, the results of the FEM models of the coupled system of the glass plate with MFC actuators and the acoustic field, both cases of the incoming wave from the infinity and the model with the acoustic box, will be presented.

Figure 5.9 shows the frequency dependencies of the acoustic TL obtained from the FEM model simulations in comparison with the experimental data from the approximative acoustic measurements. In FEM simulations, the geometry of the simple glass plate was used, however, with different external boundary conditions as it was described in Sec. 5.1.4, Subsec. 5.1.4.2. The numerical parameters considered in the simulations are listed in Table 5.1. Three situations with different boundary conditions of the glass plate were considered: Ideally fixed glass (solid thick), steel frame with $k_{\mathrm{fr}} = 1 \cdot 10^{10}$ N·m^{-1} (dashed thin), wooden frame with $k_{\mathrm{fr}} = 1 \cdot 10^{7}$ N·m^{-1} (solid thin). It is seen that steel frame represents a very good approximation of the ideally fixed glass plate. On the other hand, the

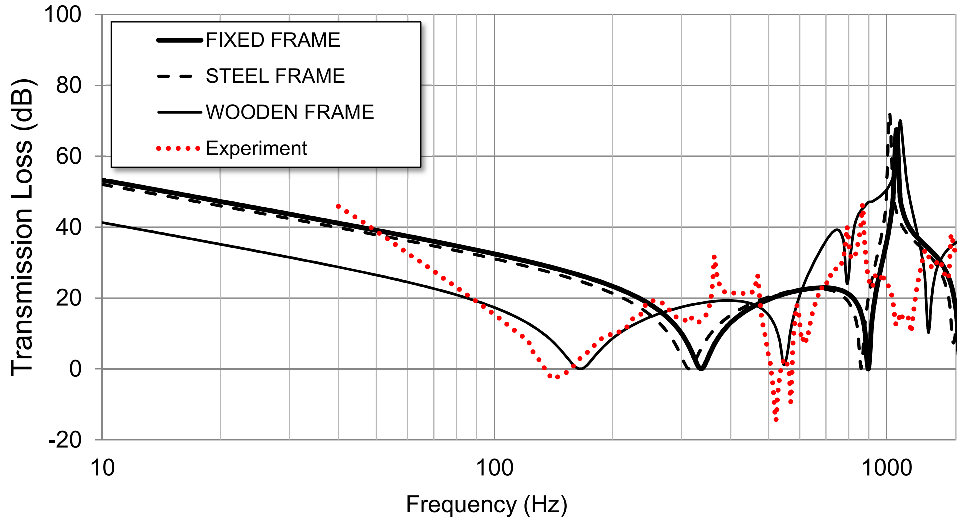

Figure 5.9: Comparison of the approximative measurement of the frequency dependency of the acoustic transmission loss through the planar glass plate (dotted) with the FEM model predictions for three different boundary conditions: Ideally fixed glass (solid thick), steel frame with $k_{\mathrm{fr}} = 1 \cdot 10^{10}$ N·m^{-1} (dashed thin), wooden frame with $k_{\mathrm{fr}} = 1 \cdot 10^{7}$ N·m^{-1} (solid thin). An acceptable agreement of the experimental data with the wooden flexible frame is noticeable.

smaller value (by 3 orders of magnitude) of the effective spring constant of the frame causes a reasonable decrease in the resonant frequencies of the resonant modes of the glass plate. The FEM model results are compared with the approximative measurement of the acoustic TL of the glass plate in a wooden frame. An acceptable agreement of the experimental data with the wooden flexible frame is noticeable. The acquired agreement of the FEM model prediction with the approximative experimental data indicates that the developed FEM model of the coupled analysis of the solid with the acoustic field is credible and that it may serve to valuable predictions of the effect of piezoelectric MFC actuators shunted by negative capacitance circuits on the frequency dependence of the acoustic TL.

Figure 5.10 shows frequency dependence of the acoustic TL obtained from FEM model simulations considering the case of the acoustic wave, which strikes the glass plate incoming from infinity (Fig. 5.10(a)) and the case of the acoustic box with the sound source at the bottom (Fig. 5.10(b)). Four situations with different curvatures of the glass plate and the electrical conditions of the piezoelectric MFC actuators were considered: (i) Planar glass plate with opened MFC actuator (solid thick), (ii) bulged glass plate with opened MFC actuator (solid thin), (iii) planar glass plate with the MFC actuator shunted by NC circuit (dashed thick), and (iv) bulged glass plate with the MFC actuator shunted by NC circuit (dashed thin). The fixed boundary conditions at the edges of the glass plate are considered, i.e. $u_i = 0$. The bulged shape of the glass plate was approximated using the displacement function in the z-axis direction in the form $z_{\max} \sin(\pi x/a) \sin(\pi y/b)$, where $z_{\max} = 5$ mm.

It is presented in Fig. 4.8 that it is possible to significantly increase the effective value of the Young's modulus using the effect of shunt circuit with a negative capacitance. Figure 5.10 shows that such an increase in the effective value of the Young's modulus of the MFC actuators has an appreciable effect on the frequency dependence of the acoustic TL through the glass plate. The numerical predictions of the FEM model indicate that it is possible to achieve the appreciable increase in the acoustic TL by about $10 - 25$ dB in the frequency range below 400 Hz due to the small increase in the curvature of the glass plate. In addition, it is noticeable that due to the effect of the NC circuit the the acoustic TL could be increased by about 25 dB at the second vibrational mode of the glass plate (850 Hz), what the NC circuit was tuned for. And finally, using the both effects, the curved shape of the glass plate and the NC circuit, the maximal increase of the acoustic TL can be achieved, particularly by about $10 - 30$ dB in the frequency range below 500 Hz and by about 25 dB at the second vibrational mode (850 Hz). The same effects of the increased curvature of the glass plate and the shunted NC circuit could be seen in Fig. 5.11. The frequency dependencies are depicted for the displacement amplitude measured in the glass plate middle point. It is clearly visible the decrease of the vibration amplitude both due to the effect of the curved shape of the glass plate and due to the shunted NC circuit.

The graphical representation of the distribution of the total acoustic pressure amplitude is shown in Fig. 5.12 for the geometry of the incoming acoustic wave from infinity and in Fig. 5.13 for the geometry of the acoustic box with the sound source at the bottom. Both results are shown for the frequency value of 850 Hz, the second vibrational mode of the glass plate. Figs. 5.12(a) and 5.13(a) stand for the cases of the planar glass plate with MFC actuator, however, with no NC circuits and Figs. 5.12(b) and 5.13(b) stand for the case of the planar glass plate with MFC actuators shunted by the NC circuits. According to the color legend it is seen that the transmitted value of the acoustic pressure is decreased due to the effect of the NC circuit.

Finally, Fig. 5.14 shows the results of the approximative measurements of the acoustic TL of the glass plate with attached MFC actuators which are (i) opened, i.e. not connected to the NC circuit (blue solid), and (ii) shunted by the NC circuit which is tuned at the frequency of the first vibrational mode of the glass plate, i.e. the value of 276 Hz (red solid). It

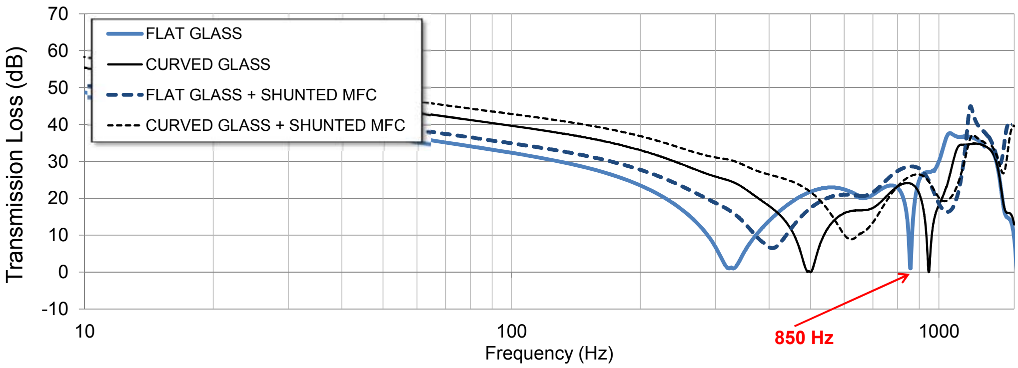

(a)

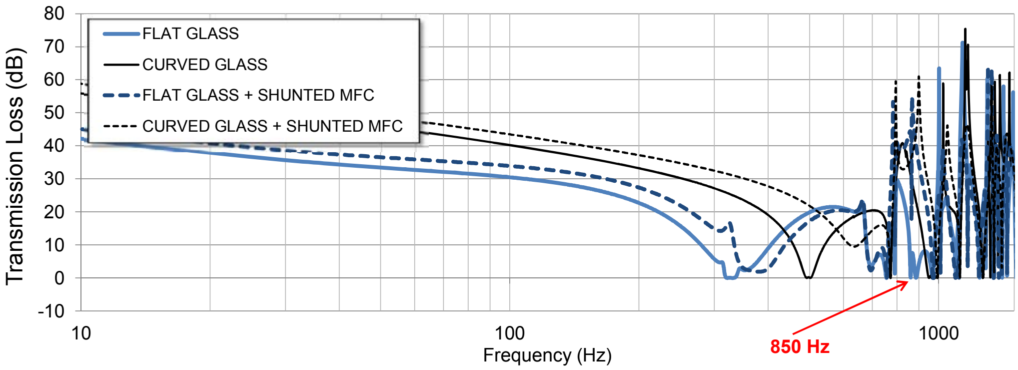

(b)

Figure 5.10: Frequency dependencies of the acoustic TL obtained from the FEM model simulations: Planar glass plate with opened MFC actuator (solid thick), bulged glass plate with opened MFC actuator (solid thin), planar glass plate with the MFC actuator shunted by NC circuit (dashed thick), and bulged glass plate with the MFC actuator shunted by NC circuit (dashed thin). The appreciable increase in the acoustic transmission loss by 10 – 25 dB in the frequency range below 400 Hz due to the small increase in the curvature of the glass plate is noticeable. In addition, it is noticeable that due to the effect of the NC circuit the the acoustic TL could be increased by about 25 dB at the second vibrational mode (850 Hz), what the NC circuit was tuned for; (a) The acoustic wave which strikes the glass plate is incoming from infinity; (b) Acoustic box with the sound source at the bottom.

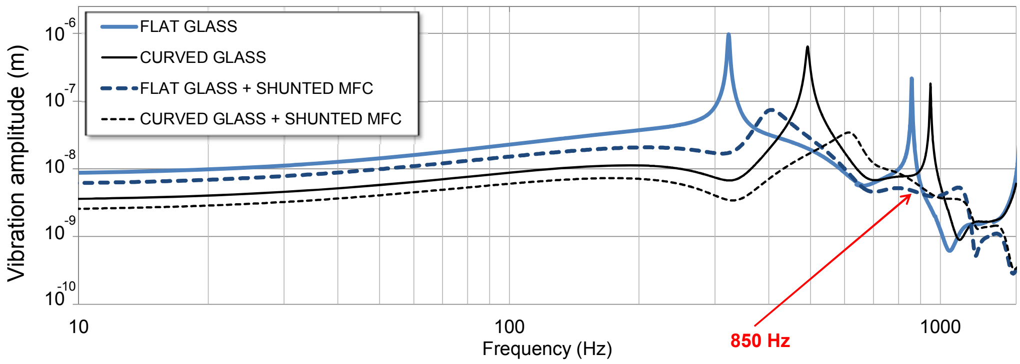

(a)

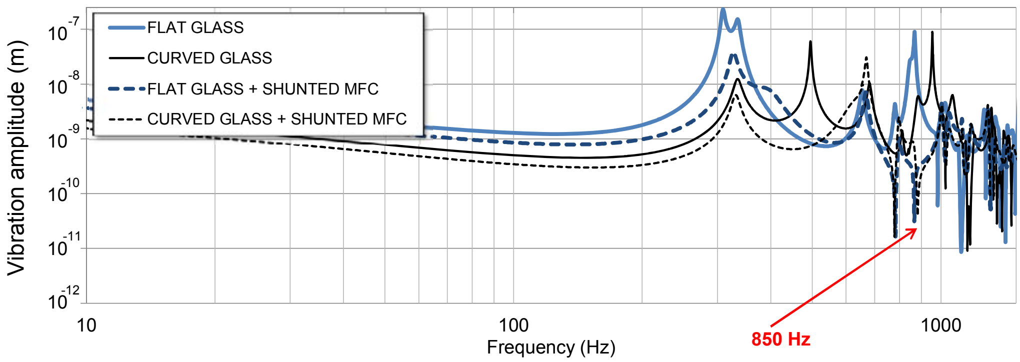

(b)

Figure 5.11: Frequency dependencies of the displacement amplitude measured in the middle point of the glass plate obtained from the FEM model simulations; (a) The acoustic wave which strikes the glass plate is incoming from infinity; (b) Acoustic box with the sound source at the bottom; It is clearly visible the decrease of the vibration amplitude both due to the effect of the curved shape of the glass plate and due to the shunted NC circuit.

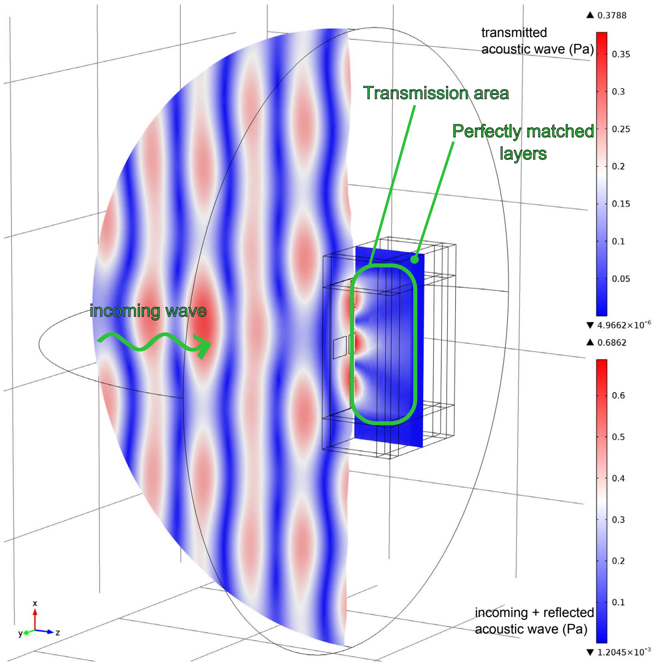

(a)

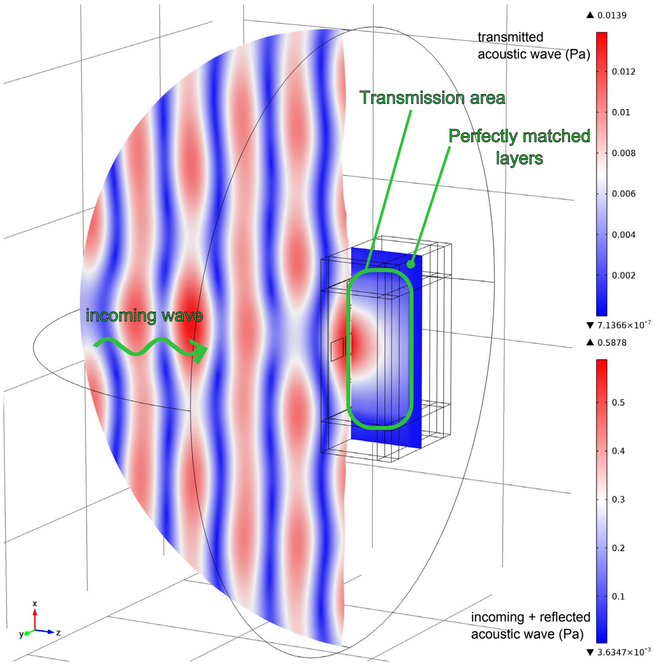

(b)

Figure 5.12: The graphical representation of the distribution of the total acoustic pressure amplitude for the geometry of the incoming acoustic wave from infinity of the frequency value of 850 Hz; (a) Planar glass plate with MFC actuators with no shunted NC circuit; (b) Planar glass plate with MFC actuators shunted by the NC circuit. According to the color legend it could be observed that the transmitted value of the acoustic pressure is decreased due to the effect of the NC circuit.

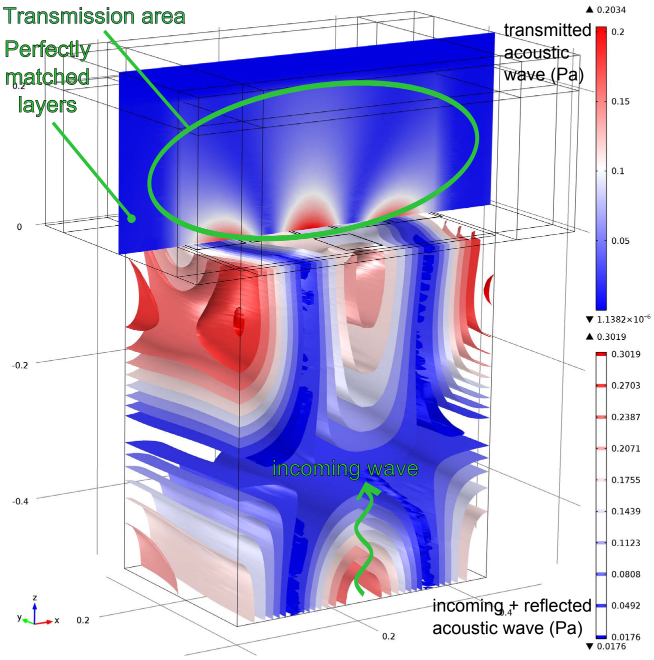

(a)

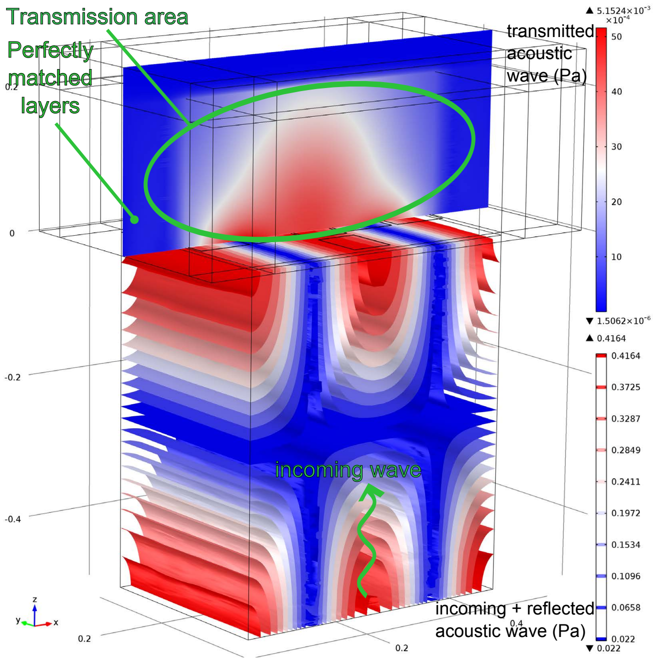

(b)

Figure 5.13: The graphical representation of the distribution of the total acoustic pressure amplitude for the geometry of the acoustic box with the sound source at the bottom of frequency value of 850 Hz; (a) Planar glass plate with MFC actuators with no shunted NC circuit; (b) Planar glass plate with MFC actuators shunted by the NC circuit. According to the color legend it could be observed that the transmitted value of the acoustic pressure is decreased due to the effect of the NC circuit.

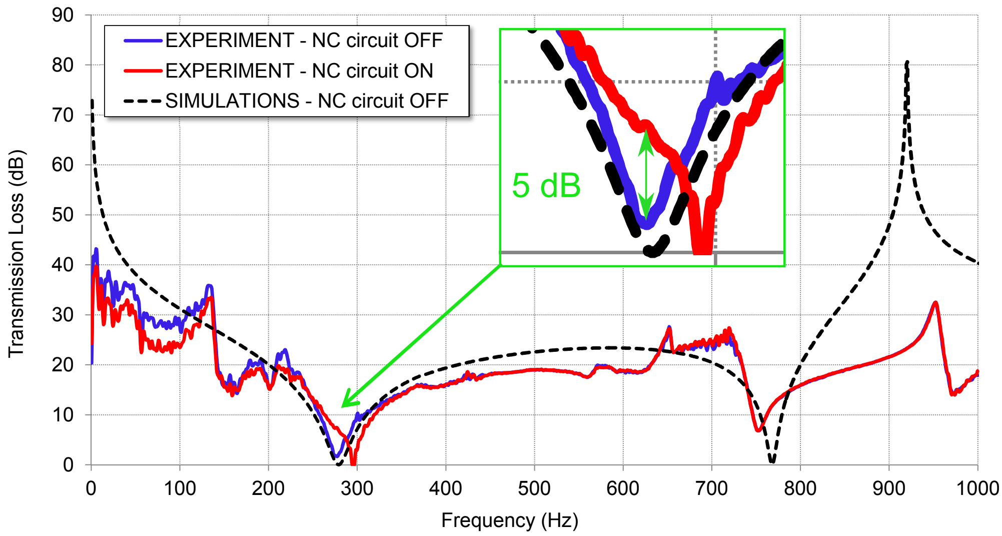

Figure 5.14: Results of the approximative measurements of the acoustic TL of the glass plate with attached MFC actuators which are opened (blue solid) and shunted by the NC circuit which is tuned at the frequency of the first vibrational mode of the glass plate, i.e. the value of 276 Hz (red solid). It is possible to distinguish that at the frequency where the NC circuit was tuned the acoustic TL is increased by about 5 dB. The results without the NC circuit are compared with the FEM model simulations of the acoustic TL of the glass plate with the added steel frame (black dashed). The acceptable agreement of the experiment with the FEM model is observed.

is possible to distinguish that at the frequency where the NC circuit was tuned the acoustic TL is increased by about 5 dB. The results without the NC circuit are compared with the FEM model simulations of the acoustic TL of the glass plate with the added steel frame (black dashed). The acceptable agreement of the experiment with the FEM model is observed.

5.4 Summary

This Section summarizes the obtained results of the FEM simulations and the experimental work. The objective of this Chapter was to analyze the possibility to increase the acoustic transmission loss of sound transmitted through the planar or curved glass plates using the attached piezoelectric MFC actuators shunted by the active circuits with a negative capacitance.

The FEM model of planar and curved glass plate with attached piezoelectric MFC actuators shunted by circuits with a negative capacitance has been developed (see Sec. 5.1). The experimental setups for the approximative measurements of the specific acoustic impedance and the surface displacement distribution are presented (see Sec. 5.2).

Sec. 5.3 presents the results of the FEM model simulations and their comparison with experimental data:

- The static bending of the glass plate when the direct voltage of 300 V was applied on the electrodes of the MFC actuators. The surface displacement of the glass plate captured by the digital holographic interferometry method is compared with the result of FEM simulation of the glass plate displacement distribution. An acceptable agreement between the experimental values and the FEM simulations can be observed.

- The dynamic response of the coupled system with attached MFC actuators on the harmonic voltage of the amplitude of 1 V. The experimental data are compared with the FEM model ones. At low frequency modes the acceptable agreement between the experiment and the FEM model is observed. On the other hand, at modes ensuing after 1 kHz value, the frequency dependence is shifted. One of the reason for this discrepancy can be the fact that in real situation of the experiment the steel frame is not ideally fixed. At higher frequencies the mass density and the Young's modulus of the glass are not the only dominant parameters which affect the resonant frequencies. It would be desirable to perform some additional FEM simulations to see how the boundary conditions of the frame affect the frequency dependence of the vibration amplitude of the glass plate, especially at higher frequencies.

- Frequency dependencies of the acoustic transmission loss obtained from the FEM model simulations with different external boundary conditions in comparison with the experimental data from the approximative measurement of the acoustic transmission loss of the glass plate in a wooden frame. Three situations with different boundary conditions of the glass plate were considered: Ideally fixed glass, steel frame and wooden frame represented by the certain appropriate value of the spring constant. It is seen that steel frame represents a very good approximation of the ideally fixed glass plate. On the other hand, the smaller value (by 3 orders of magnitude) of the effective spring constant of the frame causes a reasonable decrease in the resonant frequencies of the resonant modes of the glass plate. The predictions of the acoustic transmission loss frequency dependencies obtained by the FEM model show a good agreement with the approximative measurements. It was shown that a special attention must be paid to the specification of the correct boundary conditions at the edges of the glass plate.

- Frequency dependencies of the acoustic transmission loss obtained from the FEM model simulations which compare the four situations with different curvatures of the glass plate and the electrical conditions of the piezoelectric MFC actuators: (i) Planar glass plate with opened MFC actuator, (ii) bulged glass plate with opened MFC actuator, (iii) planar glass plate with the MFC actuator shunted by NC circuit, and (iv) bulged glass plate with the MFC actuator shunted by NC circuit. It is shown that an increase in the effective value of the Young's modulus of the MFC actuators has an appreciable effect on the frequency dependence of the acoustic transmission loss through the glass plate. The numerical predictions of the FEM model indicate that it is possible to achieve the appreciable increase in the acoustic transmission loss by about $10 - 25$ dB in the frequency range below 400 Hz due to the small increase in the curvature of the glass plate. In addition, it is noticeable that due to the effect of the NC circuit the the acoustic transmission loss could be increased by about 25 dB at the certain vibrational mode of the glass plate (850 Hz), what the NC circuit was tuned for. And finally, using the both effects, the curved shape of the glass plate and the NC circuit, the maximal increase of the acoustic TL could be achieved, particularly by about $10 - 30$ dB in the frequency range below 500 Hz and by about 25 dB at 850 Hz.

- Frequency dependencies of the approximative measurements of the acoustic transmission loss of the glass plate with attached MFC actuators which are (i) opened, i.e. not connected to the NC circuit, and (ii) shunted by the NC circuit which is tuned at the frequency of the first vibrational mode of the glass plate, i.e. the value of 276 Hz. It is possible to distinguish that at the frequency where the NC circuit was tuned the acoustic transmission loss is increased by about 5 dB.

The Chapter presents a promising approach for the suppression of the noise transmission through glass plates and shells using piezoelectric MFC actuators and negative capacitance circuits. The method starts from the vibrational analysis focusing on the effects of the elastic properties of the composite structure with piezoelectric layers. Using active shunt circuits with a negative capacitance, the effective elastic properties of the piezoelectric layers can be controlled to a large extent. As a result, the appreciable increase in the acoustic transmission loss through the glass plate composite can be achieved. The advantages of this method stem from its generality and simplicity offering an efficient tool for the control of the noise transmission through glass windows especially in the low-frequency range where the passive methods are ineffective.

A developed FEM model of the layered system of the planar structure with the piezoelectric layer can be used not only in structural-acoustic applications but also in structural-optic applications. The piezoelectric element attached to the planar structure can control its shape due to an applied electric voltage. In adaptive optics systems such deformable mirrors are the most commonly used wavefront correctors. A brief description of a deformable mirror that consists of a nickel reflective layer deposited on top of a thin PZT piezoelectric disk follows in the next Chapter.

Chapter 6

Application of the active shape control of the planar structure to adaptive optics

Deformable mirrors are the most commonly used wavefront correctors in adaptive optics systems. Nowadays, many applications of adaptive optics to astronomical telescopes, high power laser systems, and similar fast response optical devices require large diameter deformable mirrors with a fast response time and high actuator stroke. In order to satisfy such requirements, deformable mirrors based on piezoelectric layer composite structures have become a subject of intense scientific research during last two decades. In this Chapter, an optimization of several geometric parameters of a deformable mirror that consists of a nickel reflective layer deposited on top of a thin piezoelectric PZT disk to get the maximum actuator stroke is presented using the FEM model of the layered structure.

6.1 Introduction

In the middle of the last century, the resolution of terrestrial astronomical telescopes reached such limits that further improvement of their resolution required a development of methods for the correction of atmospheric distortions. The first concept of so called adaptive optics was envisioned by Babcock [141] in 1953, who proposed to use a deformable mirror to correct the atmospheric seeing. It took more than forty years to achieve a technological level that would allow the construction of adaptive optics.

During the last few decades, several concepts of deformable mirrors were implemented [142]. Examples to be mentioned here are (i) segmented mirrors, (ii) continuous thin plate mirrors, (iii) monolithic mirrors, and (iv) membrane or pellicle mirrors. It is the continuous thin plate type of

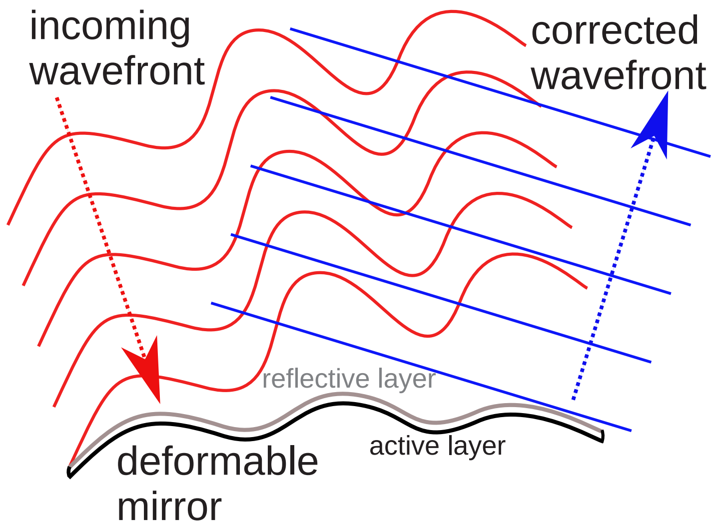

Figure 6.1: Principle of a deformable mirror. Incoming wavefront, which is distorted by atmospheric turbulence, is reflected from a deformable mirror, which corrects the shape of the wavefront to be planar again. In this study the deformable mirror is designed as a composite structure, where the reflective layer is bonded on the active piezoelectric layer.

mirrors, which has become a very popular structure mainly due to their lower technological difficulty.

With the onset of real-time wavefront corrections [143], a very convenient type of electromechanical transducers that is used as a actuator in deformable mirrors is the piezoelectric actuator. The greatest advantage of piezoelectric actuators is their fast response and relatively simple construction. In order to increase the number of degrees of freedom, deformable mirrors based on piezoelectric unimorphs or bimorphs have become a very popular and intensively studied concept [144, 145, 146, 147, 148].

Generally, this type of the deformable mirror consists of a layered sandwich composite structure, where the reflective layer is bonded on a piezoelectric layer. The reflective layer is usually made of a conductive metallic material and forms an equipotential surface. On the opposite side of the piezoelectric layer a system of electrodes is deposited using conventional techniques such as lithographic sputtering. By applying a voltage to a particular electrode, the piezoelectric layer is deformed due to the inverse piezoelectric effect in the in-plane directions. This produces bending moments in the reflective layer of the particular segment of a deformable mirror and yield its out-of-plane deformation (see Fig. 6.1).

The optimization study of the composite structure of the deformable mirror that consists of a nickel reflective layer deposited on top of a thin piezoelectric PZT disk to achieve the maximum out-of-plane deflections at

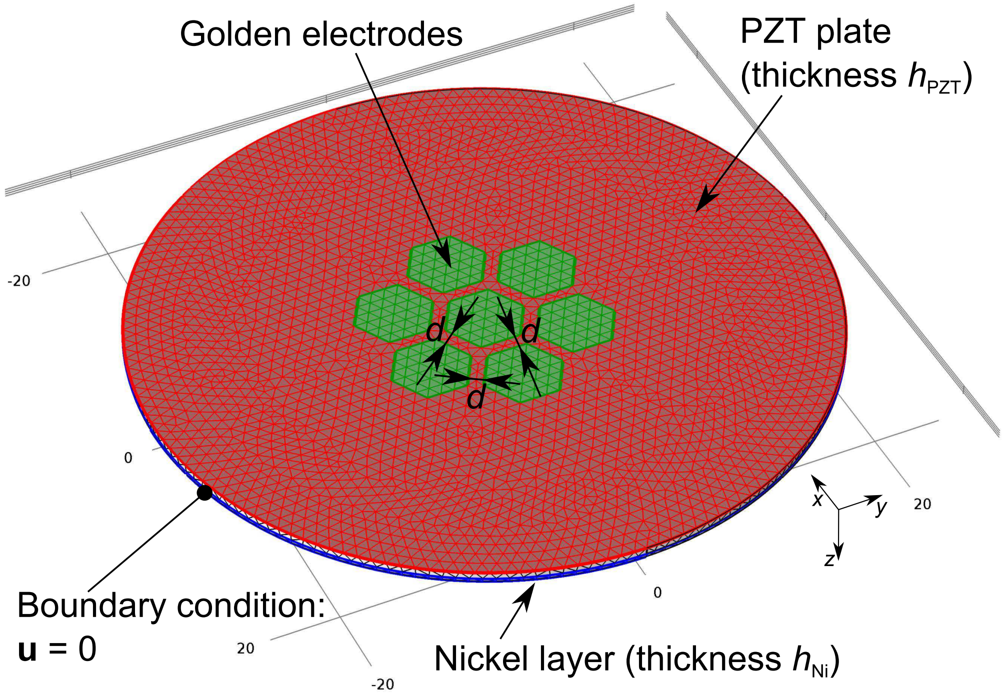

Figure 6.2: Geometry of the FEM model of the deformable mirror. It consists of the nickel reflective layer of the thickness h_{Ni} and of the PZT layer of the thickness h_{PZT}. Honeycomb structure of gold electrodes is deposited on the bottom of the PZT layer. The distance between the sputtered electrodes is denoted by a symbol d. Nickel layer itself can be considered as a grounding electrode. The mirror is fixed in its edges which indicates the boundary condition of zero displacement on this edge, i.e. $\mathbf{u} = 0$.

minimum applied voltages to the piezoelectric structure using FEM numerical simulations. In Sec. 6.2, the geometry of the deformable mirror is introduced and applied to the FEM model. In Sec. 6.3, the results of the numerical simulation and their discussion will be presented.

6.2 FEM model of the deformable mirror

Geometry of the deformable mirror is presented in Figure 6.2. The deformable mirror consists of a double-layer sandwich composite structure in a shape of a disk of the radius R. In this study, the reflective layer of thickness h_{Ni} is made of nickel. The reflective nickel layer is bonded on a piezoelectric layer of thickness h_{PZT}. The reflective layer forms an equipotential at the bottom surface of the piezoelectric layer.

On the top surface of the piezoelectric layer, a system of honeycomb golden electrodes is deposited using lithographic sputtering. The distance between the sputtered electrodes is denoted by a symbol d. It is considered that arbitrary external voltage can be applied at each particular electrode.

The equations which rule the analysis are the same as for the coupled analysis of the isotropic solid with the piezoelectrics, i.e. the Eqs. (4.3)-(4.9). Here, the piezoelectric domain is the thin PZT layer of the thickness h_{PZT} and, the isotropic linear solid domain is the reflective nickel layer of the thickness h_{Ni}.

Material parameters for the nickel layer could be found e.g. in [149]. The material for the PZT layer is considered the commonly used piezoelectric ceramic PZT-2 whose material parameters could be found e.g. in [150].

It is considered that the deformable mirror is fixed in a rigid frame along its circumference, i.e. the external boundary condition for the displacement on this surface is equal to zero, i.e. $\mathbf{u} = 0$.

6.3 Results and discussion

Fig. 6.3 shows the example of the FEM numerical simulation of the deformable mirror. In the presented simulation, the off-centered honeycomb electrode is connected to the electric potential of 200 V, the remaining electrodes are short circuited. The surface boundary between the PZT and nickel layer is taken as a grounding electrode. Using the developed FEM model of the coupled structure of the two layers of isotropic with piezoelectric material, displacements of the deformable mirror are calculated and presented. Fig. 6.3(a) presents the 2D surface plot in the plane (xy) of the displacement of the mirror. Fig. 6.3(b) presents the plot along the line which goes along the diameter of the mirror through the all three honeycomb electrodes. Fig. 6.3(c) shows the 3D graphical interpretation of the displacement of the mirror which is shown using the iso-surfaces and slices.

Figure 6.4 presents results of a similar FEM simulation, however with all honeycomb electrodes connected to the electric potential of 200 V. The maximal value of the mirror deflection which could be achieved is 2.02 μm.

The following geometrical parameters were considered: $R = 3$ mm, $d = 1$ mm, $h_{\mathrm{PZT}} = 0.5$ mm, $h_{\mathrm{Ni}} = 0.18$ mm.

In order to find the optimal ratio of the thicknesses of the nickel and PZT layers, a series of numerical FEM simulations has been performed. At the first step of each simulation, the geometry of the FEM model was modified and the thicknesses of the nickel and PZT layers were set to particular values. In the second step, the displacement of the deformable mirror was calculated. In the third step, the value of the maximum deflection above the activated electrode was determined.

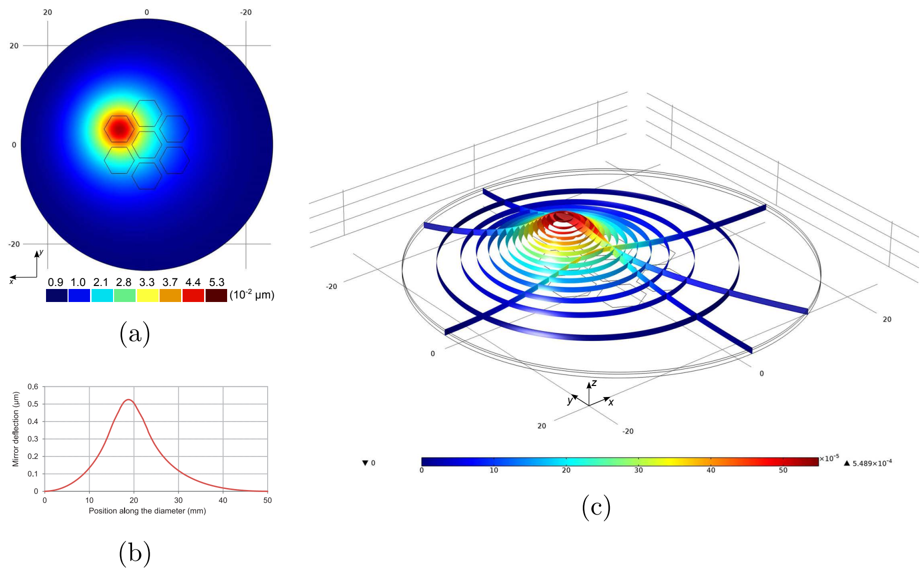

Figure 6.3: Graphical presentation of the deformable mirror displacement. One off-centered honeycomb electrode is connected to the electric potential of 200 V, the remaining electrodes are short circuited. The surface boundary between the PZT and nickel layer is taken as a grounding electrode; (a) The 2D surface plot in the plane (xy) of the displacement of the mirror; (b) Plot along the line which goes along the diameter of the mirror through the all three honeycomb electrodes; (c) The 3D graphical interpretation of the displacement of the mirror, it is shown using the iso-surfaces and slices. In any case, the color legends mean the mechanical displacement value.

Figure 6.5 shows the result of the series of simulations, where the maximal values of the mirror deflection is plotted as a function of the nickel layer thickness h_{Ni} ($0.02 - 0.6$ mm). The parameter of each curve is the PZT layer thickness h_{PZT} ($0.2 - 0.8$ mm). All the combinations of the different thicknesses of the PZT and nickel layer were used for the FEM model. It can be seen that the thiner layers of both nickel and PZT are the larger displacement of the mirror can be achieved.

Figure 6.6 presents the thickness of the nickel layer, which results in the maximum deflection of the deformable mirror, versus the thickness of the PZT layer. The dashed line presents the fit of the optimal nickel and PZT thicknesses to the linear dependence obtained by the method of least squares (i.e. the linear regression).

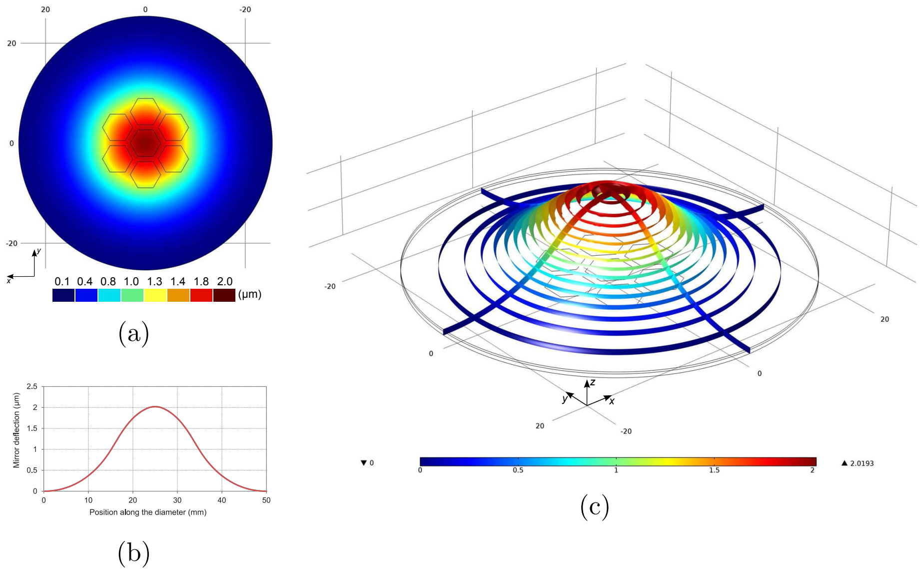

Figure 6.4: Graphical presentation of the deformable mirror displacement. All honeycomb electrodes are connected to the electric potential of 200 V. The surface boundary between the PZT and nickel layer is taken as a grounding electrode; (a) The 2D surface plot in the plane (xy) of the displacement of the mirror; (b) Plot along the line which goes along the diameter of the mirror through the all three honeycomb electrodes; (c) The 3D graphical interpretation of the displacement of the mirror, it is shown using the iso-surfaces and slices. The maximal value of the mirror deflection which could be achieved is 2.02 μm.

6.4 Summary

A developed FEM model of a double-layer composite structure was used for an application from adaptive optics, a deformable mirror, which consists of a reflective nickel layer and an active PZT material. A series of FEM simulations were performed, in order to find optimal thickness ratio of the reflective and active layers to get the maximum out-of-plane deflections at minimum applied voltages to the piezoelectric structure. The linear regression of optimal values of the thicknesses of the nickel and PZT layers was determined.

Brief description of the the obtained results indicates that the developed FEM model of the layered structure could be used across the research fields. In adaptive optics applications, it can provide an efficient and simple tool for the design of deformable mirrors with piezoelectric materials.

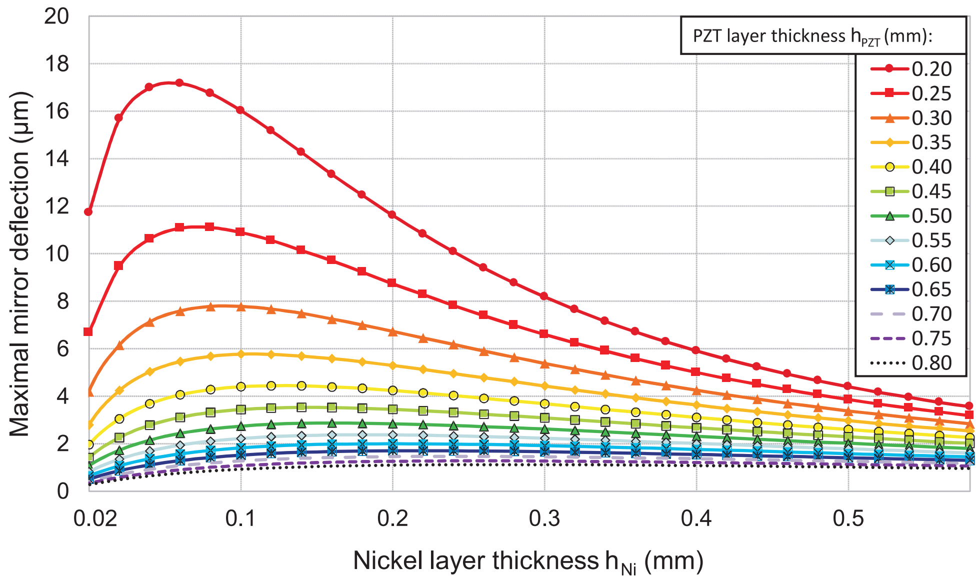

Figure 6.5: Dependences of the maximal values of the mirror deflection as a function of the nickel layer thickness h_{Ni} $(0.02-0.6$ mm). The parameter of each curve is the PZT layer thickness h_{PZT} $(0.2-0.8$ mm). All the combinations of the different thicknesses of the PZT and nickel layer were used for the FEM model. It can be seen that the thiner layers of both nickel and PZT are the larger displacement of the mirror can be achieved.

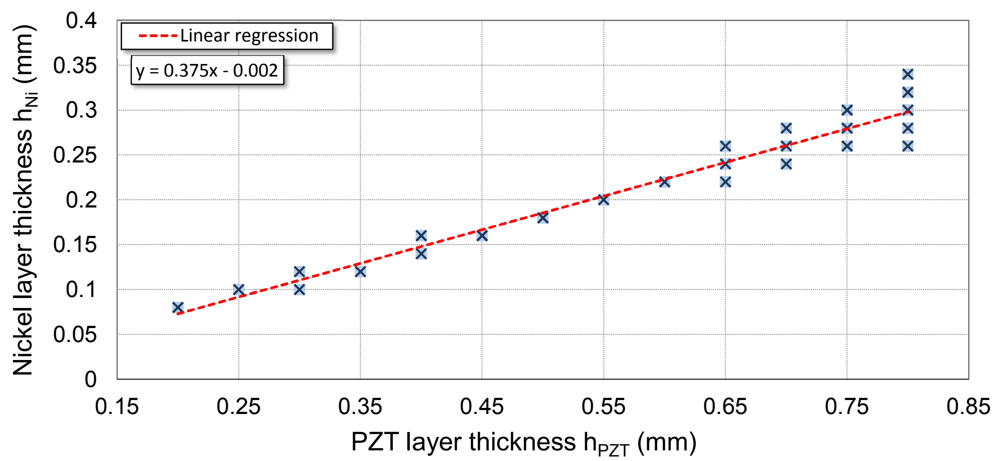

Figure 6.6: Linear regression of optimal values of the thicknesses of the nickel and PZT layers. The decisive values for the optimization were the maximal values of the mirror displacement which could be seen in Figure 6.5. It is shown that for the certain value of the PZT layer thickness could be used certain range of the nickel layer thicknesses, particularly for thicker PZT layers (from 0.65 mm).

Chapter 7

Conclusions

The Thesis was focused on the study of possibilities to actively control the static and dynamic mechanical response of planar structures by means of attached piezoelectric actuators. It was shown that piezoelectric layered planar composite structures can offer an attractive approach for the reduction of amplitude of vibrations or for the electronic shape control. Therefore, these kind of controlled structures can provide an efficient tool with the use in applications of acoustics and adaptive optics.

In acoustics, the planar structure represents the interface between two acoustic media through, which the acoustic wave is propagating. It was shown that it is possible to control the amplitudes of the reflected and transmitted waves by controlling the amplitude of the planar structure vibration. A physical parameter, which expresses the sound shielding efficiency of the structure, is called the acoustic transmission loss. Its definition formula was presented in Chap. 2. The acoustic transmission loss was then expressed by means of the specific acoustic impedance Z of the interface between two acoustic media, i.e. of the planar structure.

In Chap. 3 the key parameters that control the acoustic transmission loss of the planar structure were determined using the analytical approximative model of the glass shell, which was considered of a plane or curved geometry. The basic conclusions from the theoretical model are the followings. With an increase of the glass shell curvature ξ, the term $2Yh\xi^2$ in the denominator of Eqs. (3.23) and (3.25) increases. This yields the decrease of the amplitude of the shell displacement and, therefore, the decrease of the normal velocity of vibrations. As a result, the values of the specific acoustic impedance Z_w and subsequently the acoustic transmission loss of the glass shell increase. That actually means that a greater amplitude of the incident acoustic pressure can be reflected than transmitted to the other side. Moreover, the specific acoustic impedance Z_w of the curved shell, i.e. $\xi > 0$, increases with an increase in the Young's modulus Y and the bending stiffness coefficient G of the glass shell and the value of Z_w of the plane plate, i.e. $\xi = 0$, increases with an increase in the bending stiffness coefficient G of the plate.

Using the theoretical model of motion of the composite layered structure of the glass plate and the piezoelectric layer, it was shown that by the piezoelectric layer attached to the planar structure it is possible to control the elastic properties of the whole system (see the Eqs. (3.30) and (3.31) for the effective Young's modulus and the bending stiffness coefficient, respectively, of the layered composite structure of the glass plate and piezoelectric actuator).

In Chap. 3, it was introduced the active elasticity control method that offers an alternative technique for the suppression of the noise transmission through piezoelectric structures or a technique for active suppression of vibrations of mechanical structures by attaching the piezoelectric elements to them. The idea is that by connecting a piezoelectric layer to the active shunt circuit with a negative capacitance the effective elastic properties of the piezoelectric element can be enhanced. The effective Young's modulus of the piezoelectric element shunted by the negative capacitance circuit follows the theoretical Eq. (3.33), where one can notice that, when the capacitance C is negative, the value of the effective Young's modulus of the piezoelectric actuator can be changed to a large extent. It is shown that, when the piezoelectric actuator is attached to the surface of a glass plate (according to the Fig. 3.4) then the value of the Young's modulus Y and the bending stiffness coefficient G of the glass plate are influenced due to the action of shunted negative capacitance circuit. Then, the vibration amplitude W of the plate is reduced due to an increase in the bending stiffness coefficient G of the plate (in the case of the plane plate) and due to an increase in the bending stiffness coefficient G and the Young's modulus Y of the plate (in the case of the curved plate). In such a way of active "stiffening", the bigger part of the amplitude of acoustic pressure wave can be reflected than transmitted to the other side.

A suitable piezoelectric actuator, which can be simply attached to the various kind of surfaces (such as glass plate) and which is resistant to the cracking is the flexible macro fiber composite actuator. Its geometry, structure and fundamental properties were introduced in Chap. 4. In accord with the aforementioned approach and due to geometrical complexity of the macro fiber composite actuator, the numerical model of the macro fiber composite actuator based on the finite element method was developed. The numerical model includes: (i) definition of the representative volume element (RVE) geometry of the macro fiber composite actuator (Subsec. 4.2.1), (ii) formulation of the equations of motion and specification of numerical values of material parameters (Subsec. 4.2.2), (iii) specification of the electrical and mechanical boundary conditions (Subsec. 4.2.3), (iv) definition of state quantities averaging and the method of calculation of effective elastic and piezoelectric properties (Subsec. 4.2.4), and (v) introduction of the electromechanical interaction of the MFC actuator with the external electric negative capacitance circuit and the implementation of the method of active elasticity control on a simplified model of the macro fiber composite actuator where the movement only in the x direction is allowed (Subsec. 4.2.5).

The numerical model was used for the numerical computation of Young's moduli, shear moduli and Poisson's ratios of short-circuited macro fiber composite actuator (Subsec. 4.3.1). There can be seen an acceptable agreement between the results of the numerical computations, the producer's values and with the values obtained by other computational methods. In a similar manner, macroscopic piezoelectric constants were computed from average strains in mechanically free macro fiber composite actuator with a given testing voltage on its electrodes (Sec. 4.3.2). Again, an agreement between computed values and producer's data sheet values is appreciable. Finally, the capacitance per unit area of the macro fiber composite actuator was computed from the charge generated on the electrodes under the applied testing voltage (Sec. 4.3.3).

The effect of the electromechanical interaction of the macro fiber composite actuator and an external shunt circuit with a given capacitance was analyzed in Subsec. 4.3.4. It was roughly verified that the capacitance value of the shunt circuit controls only the values of the Young's moduli (Y_{11}, Y_{22}, Y_{33}). Values of the shear moduli (G_{12}, G_{13}, G_{23}) are not influenced by the shunt circuit. In the next step of the analysis, the implementation of the negative capacitor was introduced in Subsec. 4.3.5. At first, several simulations were computed in order to determine the optimal adjustment of the negative capacitance circuit parameters that yield the maximum value of effective Young's modulus component Y_{11}. As a result, an increase in the effective Young's modulus Y_{11} by the factor of 1000 at the frequency 850 Hz was demonstrated. After that, the frequency dependence of macroscopic Young's moduli of macro fiber composite actuator shunted by the implemented negative capacitance circuit was measured. It was demonstrated that the value of effective Young's modulus Y_{11} can be increased by the factor of 100 in a narrow frequency range $800-900$ Hz and by the factor of 20 in a frequency range $700-1000$ Hz. The value of the Young's modulus component Y_{22} can be increased by about 400 times at the given frequency and by about 20 times in a frequency range $780-910$ Hz.

In Chap. 5, using the theoretical basics about the acoustic transmission loss stated in Chap. 2 and the findings about the active elasticity control method introduced in Chap. 3 and the results of the simulations of the actively controlled orthotropic Young's modulus of the macro fiber composite actuator obtained in Chap. 4, the possibility of increasing the acoustic transmission loss of sound transmitted through planar or curved glass plates using attached piezoelectric macro fiber composite actuators shunted by the negative capacitance circuits was analyzed using the finite element method numerical simulations and experimental measurements of the acoustic transmission loss.

First, the applicability and functionality of the macro fiber composite actuators attached to the glass plate was verified by the measurement of the static bending of the glass plate when the direct voltage of 300 V was applied on the electrodes of the macro fiber composite actuators. The surface displacement of the glass plate captured by the digital holographic interferometry method is compared with the result of finite element simulation of the glass plate displacement distribution. An acceptable agreement between the experimental values and the simulations could be observed. Then, the dynamic response of the coupled system with attached macro fiber composite actuators on the harmonic voltage of the amplitude of 1 V was performed. The experimental data are again compared with the finite element method model ones. At low frequency modes the acceptable agreement between the experiment and the numerical model is observed.

In the next steps, a couple of simulations and measurements of the acoustic transmission loss were performed. The frequency dependencies of the acoustic transmission loss obtained from the numerical model simulations with different external boundary conditions are compared with the experimental data from the approximative measurement of the acoustic transmission loss of the glass plate in a wooden frame. Three situations with different boundary conditions of the glass plate were considered: Ideally fixed glass, steel frame and wooden frame represented by the certain appropriate value of the spring constant. It is seen that steel frame represents a very good approximation of the ideally fixed glass plate. On the other hand, the smaller value (by 3 orders of magnitude) of the effective spring constant of the frame causes a reasonable decrease in the resonant frequencies of the resonant modes of the glass plate. The predictions of the acoustic transmission loss frequency dependencies obtained by the finite element method model show a good agreement with the approximative measurements. It was shown that a special attention must be paid to the specification of the correct boundary conditions at the edges of the glass plate.

In order to find the most effective way how to increase the acoustic transmission loss of the glass plate, the frequency dependencies of the acoustic transmission loss were computed using the finite element model simulations, which are based on the acoustic-structure interaction. The simulations compare the four situations with different curvatures of the glass plate and the electrical conditions of the piezoelectric macro fiber composite actuators: (i) Planar glass plate with opened macro fiber composite actuator, (ii) bulged glass plate with opened macro fiber composite actuator, (iii) planar glass plate with the macro fiber composite actuator shunted by negative capacitance circuit, and (iv) bulged glass plate with the macro fiber composite actuator shunted by negative capacitance circuit. It is shown that an increase in the effective value of the Young's modulus of the macro fiber composite actuators has an appreciable effect on the frequency dependence of the acoustic transmission loss through the glass plate. The numerical predictions of the numerical model indicate that it is possible to achieve the appreciable increase in the acoustic transmission loss by about $10 - 25$ dB in the frequency range below 400 Hz due to the small increase in the curvature of the glass plate. In addition, it is noticeable that due to the effect of the negative capacitance circuit the acoustic transmission loss can be increased by about 25 dB at the certain vibrational mode of the glass plate (850 Hz), what the negative capacitance circuit was tuned for. And finally, using the both effects, the curved shape of the glass plate and the active circuit, the maximal increase of the acoustic transmission loss could be achieved, particularly by about $10 - 30$ dB in the frequency range below 500 Hz and by about 25 dB at 850 Hz.

According to the approximative acoustic measurement, the frequency dependencies of the acoustic transmission loss of the glass plate with attached macro fiber composite actuators which are (i) opened, i.e. not connected to the negative capacitance circuit, and (ii) shunted by the NC circuit which is tuned at the frequency of the first vibrational mode of the glass plate, i.e. the value of 276 Hz, show, that it is possible to distinguish that at the frequency where the negative capacitance circuit was tuned the acoustic transmission loss is increased by about 5 dB.

A developed finite element method model of the layered system of the planar structure with the piezoelectric layer can be used not only in structural-acoustic applications but also in structural-optic applications. The piezoelectric element attached to the planar structure can control its shape due to an applied electric voltage. In adaptive optics systems such deformable mirrors are the most commonly used wavefront correctors. A brief description of a deformable mirror that consists of a nickel reflective layer deposited on top of a thin PZT piezoelectric disk is presented in Chap. 6. A series of finite element method simulations were performed, in order to find optimal thickness ratio of the reflective and active layers to get the maximum out-of-plane deflections at minimum applied voltages to the piezoelectric structure. The linear regression of optimal values of the thicknesses of the nickel and PZT layers was determined.

The Thesis presents a promising approach for the suppression of the noise transmission through the plates and for the shape control of the plates using piezoelectric flexible composite piezoelectric actuators and active electronic circuits. The method starts from the vibrational analysis focusing on the effects of the elastic properties of the composite structures with piezoelectric layers. Then, optimization of the parameters of the active electronic circuit has to be done to achieve the best performance of the actuator. The advantages of this method stem from its generality and simplicity offering an efficient tool for the control of the noise transmission through glass windows especially in the low-frequency range where the passive methods are ineffective and a simple and efficient tool for the shape control of large planar optical elements.

Bibliography

[1] Z. Maekawa, J. H. Rindel, and P. Lord, *Environmental and Architectural Acoustics.* CRC Press, 2 ed., Feb. 2011.

[2] K. Omae, T. Takebayashi, and H. Sakurai, "Occupational exposure limits based on biological monitoring: the japan society for occupational health," *International Archives of Occupational and Environmental Health*, vol. 72, pp. 271–273, July 1999.

[3] W. G. Cady, *Piezoelectricity: an introduction to the theory and applications of electromechanical phenomena in crystals.* University of California: Dover Publications, 1964.

[4] H. F. Tiersten, *Linear piezoelectric plate vibrations: elements of the linear theory of piezoelectricity and the vibrations of piezoelectric plates.* Plenum Press, 1969.

[5] IEEE, "ANSI/IEEE std 176-1987 standard on piezoelectricity," 1988. Standards.

[6] A. Arnau, *Piezoelectric transducers and applications.* New York: Springer, 2008.

[7] F. Y. Cheng, *Smart Structures: Innovative Systems for Seismic Response Control.* CRC Press, Feb. 2008.

[8] P. Gaudenzi, *Smart Structures Physical Behaviour, Mathematical Modelling and Applications.* Chichester: John Wiley & Sons, 2009.

[9] J. Curie and P. Curie, "Development, par pression, de l'electricite polarise dans les crystaux hemiednes et fares inclines," *Comptes Rendus*, vol. 91, pp. 294–297, 1880.

[10] G. Lippmann, "Principe de la conservation de l'elecricite," in *Ann de Chemie e de Physique*, pp. 24–145, 1881.

[11] J. Curie and P. Curie, "Contractions et dilatations produites par des tensions electriques dans des cristaux hemiedres a faces inclinees," *Comptes Rendus*, vol. 93, pp. 1137–1140, 1881.

[12] K. F. Graff, "chapter 1: A history of ultrasonics," in *A history of ultrasonics* (Mason and Thurston, eds.), vol. 15, Academic Press, 1981.

[13] E. Jaffe, B, W. Cook, and H. Jaffe, "Piezoelectric ceramics," *Journal of Sound and Vibration*, vol. 20, pp. 562–563, Feb. 1972.

[14] A. Safari and E. K. Akdogan, eds., *Piezoelectric and acoustic materials for transducer applications.* New York: Springer, 2008.

[15] "PI ceramic: Piezo ceramics, custom piezo assemblies, piezo technology, piezoelectrics actuator, PZT transducers." `http://www.piceramic.com/index.php`.

[16] "The fascinating world of technical ceramics." `http://www.ceramtec.com/ceramic-materials/`.

[17] "Piezoelectric product | piezo products and materials supplier | APC international." `http://www.americanpiezo.com/`.

[18] "Piezoelectricity." `http://en.wikipedia.org/w/index.php?title=Piezoelectricity&oldid=534193482`, Jan. 2013. Page Version ID: 534193482.

[19] "File:Perovskite.svg." `http://en.wikipedia.org/wiki/File:Perovskite.svg`.

[20] S. O. R. Moheimani and A. J. Fleming, *Piezoelectric Transducers for Vibration Control and Damping.* Advances in Industrial Control, Springer, softcover reprint of hardcover 1st ed. 2006 ed., Dec. 2010.

[21] "Enhancing science learning through electronic library."

[22] A. Einstein, "Die grundlage der allgemeinen relativitätstheorie," *Annalen der Physik*, vol. 354, no. 7, pp. 769–822, 1916.

[23] M. Jirasek and Z. P. Bazant, *Inelastic Analysis of Structures.* John Wiley & Sons, Jan. 2002.

[24] K. Uchino, "Chapter 4 - 4.1 piezoelectric ceramics," in *Handbook of Advanced Ceramics*, pp. 107–159, Oxford: Academic Press, 2003.

[25] F. Fahy, *Foundations of engineering acoustics.* Academic Press, 2001.

[26] T. J. Cox and P. D'Antonio, *Acoustic Absorbers and Diffusers: Theory, Design and Application.* Taylor & Francis, Jan. 2009.

[27] A. L. Araújo, C. A. M. Soares, and J. Herskovits, "Optimal design and parameter estimation of frequency dependent viscoelastic laminated sandwich composite plates," *Composite Structures*, vol. 92, p. 2321–2327, 2010.

[28] J. Li and Y. Narita, "Analysis and optimal design for the damping property of laminated viscoelastic plates under general edge conditions," *Composites Part B: Engineering*, vol. 45, no. 1, pp. 972–980, 2013.

[29] J.-M. Berthelot and Y. Sefrani, "Damping analysis of unidirectional glass fiber composites with interleaved viscoelastic layers: Experimental investigation and discussion," *Journal of Composite Materials*, vol. 40, pp. 1911–1932, Nov. 2006.

[30] R. Spagnolo, *Manuale di acustica applicata.* UTET Universita, 2001.

[31] J. Legault and N. Atalla, "Sound transmission through a double panel structure periodically coupled with vibration insulators," *Journal of Sound and Vibration*, vol. 329, no. 15, pp. 3082–3100, 2010.

[32] P. Leug, "Processing of silencing sound oscillation," June 1936.

[33] H. F. Olson and E. G. May, "Electronic sound absorber," *Journal of the Acoustical Society of America*, vol. 25(6), p. 1130–1136, 1953.

[34] H. F. Olson, "Electronic control of noise, vibration, and reverberation," *Journal of the Acoustical Society of America*, vol. 28(5), p. 966–972, 1956.

[35] B. Widrow, J. J. R. Glover, J. M. McCool, J. Kaunitz, C. S. Williams, R. H. Hearn, J. R. Zeidler, J. E. Dong, and R. C. Goodlin, "Adaptive noise cancelling: Principles and applications," *Proceedings of the IEEE*, vol. 63(12), pp. 1692–1716, 1975.

[36] M. J. M. Jessel and G. Mangiante, "Active sound absorbers in an air duct," *Journal of Sound and Vibration*, vol. 23, p. 383–390, 1972.

[37] M. A. Swinbanks, "Damping for directional sound cancellation," May 1987.

[38] B. Chaplin, "Active attenuation of recurring sound," 1977.

[39] B. Chaplin, "The cancellation of repetitive noise and vibration," in *Proc. InterNoise 80*, p. 699–702, 1980.

[40] L. J. Eriksson and M. C. Allie, "Use of random noise for on-line transducer modeling in an adaptive active attenuation system," *Journal of the Acoustic Society of America*, vol. 85, p. 797–802, 1989.

[41] W. Petiet, "Acoustic vibration generator," Nov. 1996.

[42] J. P. Tagg, "Through-window speaker/microphone," Aug. 1998.

[43] J. S. Mark, "Passenger compartment noise attenuation apparatus for use in a motor vehicle," Sept. 1998.

[44] A. Jakob and M. Moser, "Active control of double-glazed windows - Part I: Feedforward control," *Applied Acoustics*, vol. 64, pp. 163–182, FEB 2003.

[45] A. Jakob and M. Moser, "Active control of double-glazed windows. Part II: Feedback control," *Applied Acoustics*, vol. 64, pp. 183–196, FEB 2003.

[46] H. Zhu, X. Yu, R. Rajamani, and K. A. Stelson, "Active control of glass panels for reduction of sound transmission through windows," *Mechatronics*, vol. 14, pp. 805–819, SEP 2004.

[47] C. C. Fuller, S. Elliott, and P. A. Nelson, *Active Control of Vibration*. Academic Press, Feb. 1996.

[48] C. R. Fuller, "Active control of sound-transmission radiation from elastic plates by vibration inputs .1. analysis," *Journal Of Sound And Vibration*, vol. 136, pp. 1–15, JAN 8 1990.

[49] V. L. Metcalf, C. R. Fuller, R. J. Silcox, and D. E. Brown, "Active control of sound-transmission radiation from elastic plates by vibration inputs .2. experiments," *Journal Of Sound And Vibration*, vol. 153, pp. 387–402, MAR 22 1992.

[50] B. T. Wang, C. R. Fuller, and E. K. Dimitriadis, "Active control of noise transmission through rectangular-plates using multiple piezoelectric or point force actuators," *Journal Of The Acoustical Society Of America*, vol. 90, pp. 2820–2830, NOV 1991.

[51] D. R. Thomas, P. A. Nelson, R. J. Pinnington, and S. J. Elliott, "An analytical investigation of the active control of the transmission of sound through plates," *Journal of Sound and Vibration*, vol. 181(3), pp. 515–539, 1995.

[52] A. Berry, J. L. Guyader, and J. Nicolas, "A general formulation for the sound radiation from rectangular, baffled plates with arbitrary boundary conditions," *Journal of the Acoustical Society of America*, vol. 88, no. 6, pp. 2792–2802, 1990.

[53] J. Pan, C. H. Hansen, and D. A. Bies, "Active control of noise transmission through a panel into a cavity .1. analytical study," *Journal Of The Acoustical Society Of America*, vol. 87, pp. 2098–2108, MAY 1990.

[54] J. Pan and C. H. Hansen, "Active control of noise transmission through a panel into a cavity .2. experimental-study," *Journal Of The Acoustical Society Of America*, vol. 90, pp. 1488–1492, SEP 1991.

[55] B. Balachandran, A. Sampath, and J. Park, "Active control of interior noise in a three-dimensional enclosure," *Smart Materials and Structures*, vol. 5, pp. 89–97, Feb. 1996.

[56] M. Al-Bassyiouni and B. Balachandran, "Sound transmission through a flexible panel into an enclosure: structural–acoustics model," *Journal of Sound and Vibration*, vol. 284, pp. 467–486, 2005.

[57] J. P. Carneal and C. R. Fuller, "An analytical and experimental investigation of active structural acoustic control of noise transmission through double panel systems," *Journal Of Sound And Vibration*, vol. 272, pp. 749–771, MAY 6 2004.

[58] Y. Li and L. Cheng, "Active noise control of a mechanically linked double panel system coupled with an acoustic enclosure," *Journal of Sound and Vibration, Short Communication*, vol. 297, p. 1068–1074, 2006.

[59] B. Naticchia and A. Carbonari, "Feasibility analysis of an active technology to improve acoustic comfort in buildings," *Building And Environment*, vol. 42, pp. 2785–2796, JUL 2007.

[60] G. Pinte, R. Boonen, and W. Desmet, "Active structural acoustic control of repetitive impact noise," *Journal of Sound and Vibration*, vol. 319, no. 3-5, pp. 768–794, 2009.

[61] M. Kozupa and J. Wiciak, "Active Vibration Control of Rectangular Plate with Distributed Piezoelements Excited Acoustically and Mechanically," *Acta Physica Polonica A*, vol. 118, pp. 95–98, JUL 2010.

[62] S. Kapuria and M. Y. Yasin, “Active vibration suppression of multilayered plates integrated with piezoelectric fiber reinforced composites using an efficient finite element model,” *Journal of Sound and Vibration*, vol. 329, pp. 3247–3265, 2010.

[63] I. Bruant, L. Gallimard, and S. Nikoukar, “Optimal piezoelectric actuator and sensor location for active vibration control, using genetic algorithm,” *Journal of Sound and Vibration*, vol. 329, pp. 1615–1635, 2010.

[64] F. Y. M. Yiqi, “Nonlinear dynamic response and active vibration control for piezoelectric functionally graded plate,” *Journal of Sound and Vibration*, vol. 329, pp. 2015–2028, 2010.

[65] A. R. Tavakolpour, M. Mailah, I. Z. M. Darus, and O. Tokhi, “Self-learning active vibration control of a flexible plate structure with piezoelectric actuator,” *Simulation Modelling Practice and Theory*, vol. 18, pp. 516–532, 2010.

[66] Y. Hu and M. A. Galland, “Acoustic transmission performance of double-wall active sound packages in a tube: Numerical/experimental validations,” *Applied Acoustics*, vol. 73, pp. 323–337, 2012.

[67] M. Yuan, H. Ji, J. Qiu, and T. Ma, “Active control of sound transmission through a stiffened panel using a hybrid control strategy,” *Journal of Intelligent Material Systems and Structures*, vol. 23, no. 7, pp. 791–803, 2012.

[68] Q. Mao and S. Pietrzko, “Control of sound transmission through double wall partitions using optimally tuned Helmholtz resonators,” *Aacta Acustica United With Acustica*, vol. 91, pp. 723–731, JUL-AUG 2005.

[69] Q. Mao and S. Pietrzko, “Experimental study for control of sound transmission through double glazed window using optimally tuned Helmholtz resonators,” *Applied Acoustics*, vol. 71, pp. 32–38, JAN 2010.

[70] S. J. Pietrzko and Q. Mao, “New results in active and passive control of sound transmission through double wall structures,” *Aerospace Science And Technology*, vol. 12, pp. 42–53, JAN 2008.

[71] D. Niederberger, *Smart Damping Materials Using Shunt Control*. Cuvillier Verlag, 2005.

[72] A. Alabama and D. Shen, *Piezoelectric Energy Harvesting Devices for Low Frequency Vibration Applications.* ProQuest, 2009.

[73] A. Erturk and D. J. Inman, *Piezoelectric Energy Harvesting.* John Wiley & Sons, Apr. 2011.

[74] A. Fleming, S. Behrens, and S. Moheimani, "Optimization and implementation of multimode piezoelectric shunt damping systems," *IEEE-ASME Transactions On Mechatronics*, vol. 7, pp. 87–94, MAR 2002.

[75] S. Behrens, A. Fleming, and S. Moheimani, "A broadband controller for shunt piezoelectric damping of structural vibration," *Smart Materials & Structures*, vol. 12, pp. 18–28, Feb 2003.

[76] A. Belloli, D. Niederberger, S. Pietrzko, M. Morari, and P. Ermanni, "Structural vibration control via r-l shunted active fiber composites," *Journal Of Intelligent Material Systems And Structures*, vol. 18, no. 3, pp. 275–287, 2007.

[77] A. Fleming, "Nanopositioning system with force feedback for high-performance tracking and vibration control," *IEEE/ASME Transactions on Mechatronics*, vol. 15, pp. 433 –447, June 2010.

[78] M. Fairbairn, S. Moheimani, and A. Fleming, "Control of an atomic force microscope microcantilever: A sensorless approach," *Journal of Microelectromechanical Systems*, vol. 20, pp. 1372 –1381, Dec. 2011.

[79] W. Larbi, J.-F. Deü, and R. Ohayon, "Finite element formulation of smart piezoelectric composite plates coupled with acoustic fluid," *Composite Structures*, vol. 94, pp. 501–509, Jan. 2012.

[80] R. L. Harne and C. R. Fuller, "Modeling of a distributed device for simultaneous reactive vibration suppression and energy harvesting," *Journal of Intelligent Material Systems and Structures*, vol. 23, pp. 655–664, Apr. 2012.

[81] J. Ducarne, O. Thomas, and J.-F. DeĂĽ, "Placement and dimension optimization of shunted piezoelectric patches for vibration reduction," *Journal of Sound and Vibration*, vol. 331, no. 14, pp. 3286–3303, 2012.

[82] M. Ciminello, L. Lecce, S. Ameduri, A. Calabro, and A. Concilio, "Multi-tone switching shunt control by a PZT network embedded into a fiberglass panel: Design, manufacture, and test," *Journal of Intelligent Material Systems and Structures*, vol. 21, pp. 437–451, MARCH 2010.

[83] T. Sluka, *Noise and vibration control using piezoelectric elements shunted by a negative capacitor*. PhD dissertation, Technical University of Liberec, Liberec, CZ, 2007.

[84] H. Lissek, R. Boulandet, M. Černík, J. Václavík, and P. Mokrý, "Design of switching amplifier used in negative impedance disposal for the active control of transducer's acoustic impedance," in *Proceedings of the 16th International Congress on Sound and Vibration, Cracow, Poland*, (Crakow, Poland), International Institute of Acoustics and Vibration (IIAV), Poland, July 2009.

[85] R. B. Hervé Lissek, "Practical active and semi-active strategies for the control of room acoustics in the low frequency range," June 2010. Invited Paper.

[86] H. Lissek, R. Boulandet, and R. Fleury, "Electroacoustic absorbers: Bridging the gap between shunt loudspeakers and active sound absorption," *The Journal of the Acoustical Society of America*, vol. 129, no. 5, pp. 2968–2978, 2011.

[87] R. Boulandet and H. Lissek, "Optimization of electroacoustic absorbers by means of designed experiments," *Applied Acoustics*, vol. 71, no. 9, pp. 830–842, 2010.

[88] R. Boulandet, E. Rivet, and H. Lissek, "Electroacoustic absorbers II: implementation of a digital synthetic admittance for controlling the dynamics of electroacoustic absorbers," (Rio de Janeiro, Brazil), July 2011.

[89] T. Sluka, P. Mokry, and H. Lissek, "A theory of sound transmission through a clamped curved piezoelectric membrane connected to a negative capacitor," *International Journal of Solids and Structures*, vol. 47, no. 17, pp. 2260–2267, 2010.

[90] M. Date, M. Kutani, and S. Sakai, "Electrically controlled elasticity utilizing piezoelectric coupling," *Journal of Applied Physics*, vol. 87, no. 2, pp. 863–868, 2000.

[91] T. Okubo, H. Kodama, K. Kimura, K. Yamamoto, E. Fukada, and M. Date, "Sound-isolation and vibration-isolating efficiency piezoelectric materials connected to negative capacitance circuits," in *Proc. 17th International Congress on Acoustics*, pp. 301–306, 2001.

[92] H. Kodama, T. Okubo, M. Date, and E. Fukada, "Sound reflection and absorption by piezoelectric polymer films," in *Proc. Materials*

Research Society Symposium, vol. 698, (506 Keystone Drive, Warrendale, PA 15088-7563 USA), pp. 43–52, Materials Research Society, 2002.

[93] P. Mokry, E. Fukada, and K. Yamamoto, "Noise shielding system utilizing a thin piezoelectric membrane and elasticity control," *Journal of Applied Physics*, vol. 94, no. 1, pp. 789–796, 2003.

[94] P. Mokry, E. Fukada, and K. Yamamoto, "Sound absorbing system as an application of the active elasticity control technique," *Journal of Applied Physics*, vol. 94, no. 11, pp. 7356–7362, 2003.

[95] E. Fukada, M. Date, K. Kimura, T. Okubo, H. Kodama, P. Mokry, and K. Yamamoto, "Sound isolation by piezoelectric polymer films connected to negative capacitance circuits," *IEEE Transactions on Dielectrics and Electrical Insulation*, vol. 11, pp. 328–333, APR 2004.

[96] E. Fukada, M. Date, and H. Kodama, "Recent trends on application of piezoactive polymers to acoustics," *Materials Technology*, vol. 19, pp. 83–90, JUN 2004.

[97] K. Imoto, M. Nishiura, K. Yamamoto, M. Date, E. Fukada, and Y. Tajitsu, "Elasticity control of piezoelectric lead zirconate titanate (pzt) materials using negative-capacitance circuits," *Japanese Journal of Applied Physics*, vol. 44, no. 9B, pp. 7019–7023, 2005.

[98] K. Tahara, H. Ueda, J. Takarada, K. Imoto, K. Yamamoto, M. Date, E. Fukada, and Y. Tajitsu, "Basic study of application for elasticity control of piezoelectric lead zirconate titanate materials using negative-capacitance circuits to sound shielding technology," *Japanese Journal of Applied Physics*, vol. 45, no. 9B, pp. 7422–7425, 2006.

[99] J. Václavík and P. Mokrý, "Measurement of mechanical and electrical energy flows in the semiactive piezoelectric shunt damping system," *Journal of Intelligent Material Systems and Structures*, vol. 23, pp. 527–533, 2012.

[100] X. Cao, H. Hua, and Z. Zhang, "Sound radiation from shear deformable stiffened laminated plates," *Journal of Sound and Vibration*, vol. 330, no. 16, pp. 4047–4063, 2011.

[101] X. Cao, H. Hua, and C. Ma, "Acoustic radiation from shear deformable stiffened laminated cylindrical shells," *Journal of Sound and Vibration*, vol. 331, no. 3, pp. 651–670, 2012.

[102] F. X. Xin and T. J. Lu, "Analytical modeling of wave propagation in orthogonally rib-stiffened sandwich structures: Sound radiation," *Comput. Struct.*, vol. 89, no. 5-6, pp. 507–516, 2011.

[103] D. Chronopoulos, B. Troclet, M. Ichchou, and J. Laine, "A unified approach for the broadband vibroacoustic response of composite shells," *Composites Part B: Engineering*, vol. 43, no. 4, pp. 1837–1846, 2012.

[104] S. K. Sarangi and M. C. Ray, "Active damping of geometrically nonlinear vibrations of laminated composite shallow shells using vertically/obliquely reinforced 1-3 piezoelectric composites," *International Journal of Mechanics and Materials in Design*, vol. 7, pp. 29–44, Mar. 2011.

[105] S. Timoshenko, *Theory of Plates and Shells*. McGraw-Hill Book Company, 1940.

[106] K. Graff, *Wave motion in elastic solids*. Dover Publication, 1991.

[107] W. Soedel, *Vibrations of Shells and Plates*. Marcel Dekker, 2004.

[108] S. W. Tsai, *Theory of Composites Design*. Think Composites, 1992.

[109] T. S. Sluka, H. Kodama, E. Fukada, and P. Mokrý, "Sound shielding by a piezoelectric membrane and a negative capacitor with feedback control," *IEEE Transactions on Ultrasonics, Ferroelectrics, and Frequency Control*, vol. 55, pp. 1859–1866, AUG 2008.

[110] T. Sluka and P. Mokry, "Feedback control of piezoelectric actuator elastic properties in a vibration isolation system," *Ferroelectrics*, vol. 351, pp. 51–61, 2007.

[111] H. Kodama, K. Yamamoto, M. Date, and E. Fukada, "Vibration control of curved piezoelectric sheets using negative capacitance circuits," *Ferroelectrics*, vol. 351, no. 1, pp. 33–42, 2007.

[112] P. Mokry, M. Kodejska, and T. Sluka, "On the vibration control using a piezoelectric actuator and a negative capacitor adjusted by a microprocessor," in *IEEE Proceedings of the 16th Intenational Symposium on Application of Ferroelectrics, Nara, Japan*, pp. 786–789, 2007.

[113] J. Takarada, K. Imoto, K. Yamamoto, M. Date, E. Fukada, and Y. Tajitsu, "Vibration control of piezoelectric lead zirconate titanate ceramics using negative capacitance," *Japanese Journal of Applied Physics*, vol. 47, pp. 7698–7701, Sept. 2008.

[114] H. A. Sodano, G. Park, and D. J. Inman, "An investigation into the performance of macro-fiber composites for sensing and structural vibration applications," *Mechanical Systems and Signal Processing*, vol. 18, pp. 683–697, 2004.

[115] N. W. Hagood and A. A. Bent, "Development of piezoelectric fiber composites for structural actuation," in *AIAA/ASME/ASCE/AHS/ASC 34th Structures, Structural Dynamics, and Materials Conference*, vol. -1, pp. 3625–3638, Apr. 1993.

[116] N. W. Hagood, R. Kindel, K. Ghandi, and P. Gaudenzi, "Improving transverse actuation of piezoceramics using interdigitated surface electrodes," in *Proc. SPIE 1917, Smart Structures and Materials 1993: Smart Structures and Intelligent Systems*, pp. 341–352, 1993.

[117] W. K. Wilkie, R. G. Bryant, J. W. High, R. L. Fox, R. F. Hellbaum, A. Jalink, B. D. Little, and P. H. Mirick, "Low-cost piezocomposite actuator for structural control applications," in *Society of Photo-Optical Instrumentation Engineers (SPIE) Conference Series* (J. H. Jacobs, ed.), vol. 3991, pp. 323–334, June 2000.

[118] "Smart material corp.." `http://www.smart-material.com`, 2000-2012.

[119] B. R. Williams, G. Park, D. J. Inman, and W. K. Wilkie, "An overview of composite actuators with piezoceramic fibers," in *Proceedings of 20th International Modal Analysis Conference*, (Los Angles, CA), Feb. 2003.

[120] W. K. Wilkie, J. W. Bryant, R. L. Fox, R. G. Hellbaum, R. F. High, A. Jalink, B. D. Little, and P. H. Mirick, "Method of fabricating a piezoelectric composite apparatus," 2003.

[121] H. A. Sodano, J. Lloyd, and D. J. Inman, "An experimental comparison between several active composite actuators for power generation," *Smart Materials and Structures*, vol. 15, no. 5, pp. –1211, 2006.

[122] A. J. Schönecker, T. Daue, B. Brückner, C. Freytag, L. Hähne, and T. Rödig, "Overview on macrofiber composite applications," in *Society of Photo-Optical Instrumentation Engineers (SPIE) Conference Series* (W. D. Armstrong, ed.), vol. 6170, pp. 408–415, Apr. 2006.

[123] A. A. N. Bent and W. Hagood, "Piezoelectric fiber composites with interdigitated electrodes," *Journal of Intelligent Material Systems and Structures*, vol. 8, pp. 903–919, 1997.

[124] P. Tan and L. Tong, "A micro-electromechanics model for the 3-d pfrc materials," *Journal of Composite Materials*, vol. 36, pp. 127–141, Jan. 2002.

[125] A. Deraemaeker, H. Nasser, A. Benjeddou, and A. Preumont, "Mixing rules for the piezoelectric properties of macro fiber composites," *Journal of Intelligent Material Systems and Structures*, vol. 20, pp. 1475–1482, Aug. 2009.

[126] H. Berger, S. Kari, U. Gabbert, R. Rodriguez-Ramos, J. Bravo-Castillero, and R. Guinovart-Diaz, "A comprehensive numerical homogenisation technique for calculating effective coefficients of uniaxial piezoelectric fibre composites," *Materials Science and Engineering A*, vol. 412, pp. 53–60, 2005.

[127] T. Tang and W. Yu, "Variational asymptotic micromechanics modeling of heterogeneous piezoelectric materials," *Mechanics of Materials*, vol. 40, pp. 812–824, 2008.

[128] J. A. Oliveira, J. P. da Cruz, and F. Teixeira-Dias, "Asymptotic homogenisation in linear elasticity. part ii: Finite element procedures and multiscale applications," *Computational Materials Science*, vol. 45, pp. 1081–1096, 2009.

[129] H. Nasser, A. Deraemaeker, and S. Belouettar, "Electric field distribution in macro fiber composite using interdigitated electrodes," *Advanced Materials Research*, vol. 47-50, pp. 1173–1176, June 2008.

[130] M. E. Moreno, V. Tita, and F. D. Marques, "Finite element analysis applied to evaluation of effective material coefficients for piezoelectric fiber composites," in *Proceedings Brazilian Symposium on Aerospace Eng. & Applications*, (S. J. Campos, SP, Brazil), 2009.

[131] A. Deraemaeker and H. Nasser, "Numerical evaluation of the equivalent properties of macro fiber composite (mfc) transducers using periodic homogenization," *International Journal of Solids and Structures*, vol. 47, pp. 3272–3285, 2010.

[132] F. Biscani, H. Nasser, S. Belouettar, and E. Carrera, "Equivalent electro-elastic properties of macro fiber composite (mfc) transducers using asymptotic expansion approach," *Composites: Part B*, vol. 42, pp. 444–455, 2011.

[133] "Aremco products, inc.." `http://www.aremco.com/`, 2012.

[134] "efunda, inc.: Piezo data: Pzt-5a." `http://www.efunda.com/materials/piezo/material_data/matdata_output.cfm?Material_ID=PZT-5A`, 2012.

[135] P. Suquet, *Homogenisation Techniques for Composite Media.* Springer-Verlag, 1987.

[136] R. B. Williams, D. J. Inman, M. R. Schultz, M. W. Hyer, and W. K. Wilkie, "Nonlinear tensile and shear behavior of macro fiber composite actuators," *Journal of Composite Materials*, vol. 38, no. 10, pp. 855–869, 2004.

[137] J.-P. Berenger, "A perfectly matched layer for the absorption of electromagnetic waves," *J. Comput. Phys.*, vol. 114, no. 2, pp. 185–200, 1994.

[138] COMSOL, "Comsol multiphysics user's guide, version 4.3a," Nov. 2012.

[139] R. H. Doremus, "Glasses," in *Materials Sciences in Space* (P. B. Feuerbacher, D.-I. H. Hamacher, and D. R. J. Naumann, eds.), pp. 447–464, Springer Berlin Heidelberg, Jan. 1986.

[140] R. H. Doremus, *Glass Science, 2nd Edition.* Wiley-Interscience, 2 ed., Mar. 1994.

[141] H. W. Babcock, "Possibility of compensating astronomical seeing," *Publ. Astron. Soc. Pac.*, vol. 65, p. 229, 1953.

[142] J. Hardy, "Active optics: A new technology for the control of light," *Proceedings of the IEEE*, vol. 66, pp. 651 – 697, June 1978.

[143] F. Merkle, "Real-time wave-front sensing and adaptive optics," in *Diffraction-limited Imaging With Very Large Telescopes* (D. Aalloin and J. Mariotti, eds.), vol. 274 of *Nato Advanced Science Institutes Series, Series C, Mathematical And Physical Sciences*, pp. 237–248, 1989. Nato Advanced Study Inst On Diffraction-limited Imaging With Very Large Telescopes, Cargese, France, Sep 13-23, 1988.

[144] H. Zhao, P. Fekete, and J. OByrne, "Prototype bimorph mirror for the AAT adaptive optics system," in *Adaptive Optics And Applications* (R. Tyson and R. Fugate, eds.), vol. 3126 of *Proceedings Of The Society Of Photo-optical Instrumentation Engineers (SPIE)*, pp. 384–390, 1997. Conference on Adaptive Optics and Applications, SAN DIEGO, CA, JUL 30-AUG 01, 1997.

[145] M. Huonker, G. Waibel, A. Giesen, and H. Hugel, "Fast and compact adaptive mirror," in *Lasers in material processing* (L. Beckmann, ed.), vol. 3097 of *Proceedings of the society of photo-optical instrumentation engineers (SPIE)*, pp. 310–319, 1997. Conference on Lasers in Material Processing, MUNICH, GERMANY, JUN 16-20, 1997.

[146] R. Signorato, O. Hignette, and J. Goulon, "Multi-segmented piezoelectric mirrors as active/adaptive optics components," *Journal of Synchrotron Radiation*, vol. 5, pp. 797–800, May 1998.

[147] E. Yang and K. Shcheglov, "A piezoelectric unimorph deformable mirror concept by wafer transfer for ultra large space telescopes," in *Adaptive Optical System Technologies Ii, Pts 1 And 2* (P. Wizinowich and D. Bonaccini, eds.), vol. 4839 of *Proceedings Of The Society Of Photo-optical Instrumentation Engineers (SPIE)*, pp. 703–710, 2003. Conference on Adaptive Optical System Technologies II, WAIKOLOA, HI, AUG 22-26, 2002.

[148] I. Kanno, T. Kunisawa, T. Suzuki, and H. Kotera, "Development of deformable mirror composed of piezoelectric thin films for adaptive optics," *Selected Topics in Quantum Electronics, IEEE Journal of*, vol. 13, pp. 155 –161, Apr. 2007.

[149] "eFunda: general information on element nickel." `http://www.efunda.com/materials/elements/element_info.cfm?Element_ID=Ni`.

[150] "eFunda: properties of piezo material lead zirconate titanate (PZT-2)." `http://www.efunda.com/materials/piezo/material_data/matdata_output.cfm?Material_ID=PZT-2`.

Publications of the Author

[A.1] K. Nováková, P. Mokrý, J. Václavík, and V. Lédl, "Moderní trendy v semi-aktivním potlačování přenosu hluku skrz okenní tabuli pomocí piezoelektrických aktuátorů," *Silnice a železnice*, vol. 5, pp. IX–XIII, 2010.

- Journal Article

[A.2] K. Nováková, P. Mokrý, J. Václavík, and V. Lédl, "Analysis of noise transmission through the window glass plate and its control using the Macro Fiber Composite actuator," in *Proc. IEEE 19th International Symposium on Applications of Ferroelectrics*, Edinburgh, SCOTLAND, 2010, pp. 1–4.

- Presented at the 19th IEEE International Symposium on the Applications of Ferroelectrics (ISAF 2010), Edinburgh, SCOTLAND. (oral presentation)

[A.3] K. Nováková and P. Mokrý, "Numerical simulation of mechanical behavior of a Macro Fiber Composite piezoelectric actuator shunted by a negative capacitor," in *Proc. 10th International Workshop on Electronics, Control, Measurement and Signals (ECMS)*, Liberec, Česká republika, 2011, pp. 1–5.

- Presented at the 10th International Workshop on Electronics, Control, Measurement and Signals (ECMS 2011), Liberec, Česká republika. (oral presentation)

[A.4] K. Nováková and P. Mokrý, "Application of piezoelectric macro-fiber-composite actuators for the suppression of noise transmission through curved glass plates," in *Proc. 20th IEEE International Symposium on Applications of Ferroelectrics*, Vancouver, CANADA, 2011, pp. 1–5.

- Presented at the 20th IEEE International Symposium on the Applications of Ferroelectrics (ISAF 2011), Vancouver, CANADA. (oral presentation)

[A.5] K. Nováková and P. Mokrý, "Glass Plates Noise Transmission Suppression By Means of Distributed Piezoelectric Composite Actuators Shunted By an Active Circuitle," in *Proc. COMSOL Conference 2012 Milan*, Milan, ITALY, 2012.

- Presented at the COMSOL Conference 2012 Milan, ITALY. (poster)

[A.6] A. Kruchenko, K. Nováková and P. Mokrý, "Optimization of electrode geometry and piezoelectric layer thickness of a deformable mirror incoming corrected mirror," in *Proc. Optics and Measurement International Conference*, Liberec, Česká republika, 2012, pp. 69–73.

- Presented at the Optics and Measurement International Conference 2012, Liberec, Česká republika. (poster)

[A.7] K. Nováková, P. Mokrý, and J. Vaclavík, "Využití piezoelektrických kompozitních aktuátorů k potlačování přenášeného hluku skrz tenkostěnné plošné struktury," *Jemná mechanika a optika*, vol. 57, no. 11–12, pp. 300–307, Dec. 2012.

- Journal Article

[A.8] K. Nováková, P. Mokrý, and J. Vaclavík, "Application of piezoelectric macro-fiber-composite actuators to the suppression of noise transmission through curved glass plates," *IEEE Transactions on Ultrasonics, Ferroelectrics and Frequency Control*, vol. 59, no. 9, pp. 2004–2014, Sep. 2012.

- Journal Article

[A.9] A. Kruchenko, K. Nováková and P. Mokrý, "Optimization of electrode geometry and piezoelectric layer thickness of a deformable mirror incoming corrected mirror," in *EPJ Web of Conferences*, 2013, In Press.

- Journal Article In Press

[A.10] K. Nováková and P. Mokrý, "Numerical computation of effective material properties of Macro Fiber Composite actuator shunted by a negative capacitance circuit," *Composite Structures*, 2013, Submitted.

- Submitted Journal Article
- Under review

Publications of the Author which are not directly related to the Thesis

[B.1] P. Mokrý, K. Nováková, M. Marvan, and J. Fousek, "Dielectrophoretic forces generated by ferroelectric polydomain films," *Phase Transitions*, vol. 84, no. 9–10, pp. 810–820, Sep. 2011.

- Journal Article

[B.2] M. Alexeev, R. Birsa, F. Bradamante, A. Bressan, M. Chiosso, P. Ciliberti, S. Dalla Torre, O. Denisov, V. Duic, A. Ferrero, M. Finger, M. Finger Jr., H. Fischer, M. Giorgi, M. Gregori, B. Gobbo, F. H. Heinsius, F. Herrmann, K. Königsmann, L. Lauser, S. Levorato, A. Maggiora, A. Martin, G. Menon, A. Mutter, F. Nerling, K. Novakova, D. Panzieri, G. Pesaro, J. Polak, E. Rocco, C. Santos, G. Sbrizzai, P. Schiavon, C. Schill, S. Schopferer, M. Slunecka, F. Sozzi, L. Steiger, M. Sulc, S. Takekawa, F. Tessarotto, and H. Wollny, "Single-photon detection with THGEM-based counters," *Nuovo Cimento della Societa Italiana di Fisica C*, vol. 34, no. 6, pp. 52–56, 2011.

- Journal Article

[B.3] M. Alexeev, F. Barbosa, R. Birsa, F. Bradamante, A. Bressan, M. Chiosso, P. Ciliberti, S. D. Torre, O. Denisov, V. Duic, M. Finger, M. Finger, H. Fischer, M. Giorgi, B. Gobbo, M. Gregori, F. Herrmann, K. Königsmann, D. Kramer, S. Levorato, A. Maggiora, A. Martin, G. Menon, A. Mutter, F. Nerling, K. Novakova, J. Novy, D. Panzieri, J. Polak, E. Rocco, C. Santos, G. Sbrizzai, P. Schiavon, C. Schill, S. Schopferer, M. Slunecka, F. Sozzi, L. Steiger, M. Sulc, S. Takekawa, F. Tessarotto, J. F. C. A. Veloso, and H. Wollny, "Detection of single photons with ThickGEM-based counters," *Journal of Instrumentation*, vol. 7, no. 02, pp. C02014–C02014, 2012.

- Journal Article

[B.4] M. Alexeev, F. Barbosa, R. Birsa, F. Bradamante, A. Bressan, M. Chiosso, P. Ciliberti, S. Dalla Torre, O. Denisov, V. Duic, A. Ferrero, M. Finger, M. Finger, H. Fischer, M. Giorgi, B. Gobbo, M. Gregori, F. H. Heinsius, F. Herrmann, K. Königsmann, D. Kramer, L. Lauser, S. Levorato, A. Maggiora, A. Martin, G. Menon, K. Novakova, J. Novy, D. Panzieri, G. Pesaro, J. Polak, E. Rocco, C. Santos, G. Sbrizzai, P. Schiavon, C. Schill, S. Schopferer, M. Slunecka, F. Sozzi, L. Steiger, M. Sulc, S. Takekawa, F. Tessarotto, C. Veloso, and H. Wollny, “Detection of single photons with THickGEM-based counters,” *Nuclear Instruments and Methods in Physics Research Section A: Accelerators, Spectrometers, Detectors and Associated Equipment*, vol. 695, pp. 159–162, Dec. 2012.

- Journal Article

[B.5] M. Alexeev, R. Birsa, F. Bradamante, A. Bressan, M. Chiosso, P. Ciliberti, S. D. Torre, O. Denisov, V. Duic, M. Finger, M. Finger, H. Fischer, M.Giorgi, B. Gobbo, M. Gregori, F. Herrmann, K. K. önigsmann, D. Kramer, S. Levorato, A. Maggiora, A. Martin, G. Menon, A. Mutter, F. Nerling, K. Novakova, J. Novy, D. Panzieri, F. Pereira, J. Polak, E. Rocco, C. A. Santos, G. Sbrizzai, P. Schiavon, C. Schill, S. Schopferer, M. Slunecka, F. Sozzi, L. Steiger, M. Sulc, S. Takekawa, F. Tessarotto, J. F. C. A. Veloso, and H. Wollny, “Development of THGEM-based Photon Detectors for COMPASS RICH-1,” *Physics Procedia*, vol. 37, pp. 781–788, Jan. 2012.

- Journal Article